

## Microwave Ferrites, Part 2: Passive components and electrical tuning

Ümit Özgür<sup>i</sup>, Yahya Alivov, and Hadis Morkoç

Department of Electrical and Computer Engineering  
Virginia Commonwealth University  
Richmond, VA 23284

Received: 5 January 2009

### Abstract

Low-loss ferrimagnets are the basis for passive microwave components operating in a wide range of frequencies. The magnetic resonances of passive components can be tuned using static magnetic fields over a wide frequency range, where higher operation frequencies require higher magnetic bias unless hexaferrites with large crystalline anisotropy are used. However, electrical tuning of the operation frequency, which can be achieved if the magnetic property of the material is sensitive to the field through magnetoelectric (ME) coupling, is more attractive than magnetic tuning. In the so-called multiferroic materials such as TbMnO<sub>3</sub>, TbMn<sub>2</sub>O<sub>5</sub>, BiFeO<sub>3</sub>, Cr<sub>2</sub>O<sub>3</sub>, and BiMnO<sub>3</sub>, which possess simultaneously both the ferroelectric and ferromagnetic properties, ME coupling is very small to be practical. The ME effect, however, can be significantly enhanced in the case of bilayer/multilayer structures with one constituent highly piezoelectric, such as Pb(Zr<sub>1-x</sub>Ti<sub>x</sub>)O<sub>3</sub> (PZT) and 0.7Pb(Mg<sub>1/3</sub>Nb<sub>2/3</sub>)O<sub>3</sub>-0.3PbTiO<sub>3</sub> (PMN-PT), and the

---

<sup>i</sup> E-mail: [uozgur@vcu.edu](mailto:uozgur@vcu.edu)

other highly ferromagnetic, opening up the possibility for a whole host of tunable microwave passive components. In such structures, the strain induced by the electric field applied across the piezoelectric material is transferred mechanically to the magnetic material, which then experiences a change in its magnetic permeability through magnetostriction. Additionally, electrical tuning coupled with high dielectric permittivity and magnetic susceptibility could lead to miniature microwave components and/or make operation at very high frequencies possible without the need for increased size and weight common in conventional approaches. In Part 1 of this review, fundamentals of ferrite materials, interconnecting chemical, structural, and magnetic properties with the treatment of various types of ferrites used in microwave systems are discussed. Part 2 discusses the basis for coupling between electrical and magnetic properties for highly attractive electrical tuning of passive components by combining piezoelectric materials with ferrites and various device applications of ferrites.

# TABLE OF CONTENTS

<b>1. INTRODUCTION.....</b>	<b>4</b>
<b>2. PRINCIPLES OF OPERATION OF MICROWAVE PASSIVE MAGNETIC COMPONENTS</b>	<b>5</b>
2.1. FARADAY ROTATION .....	5
2.2. MAGNETOELECTRIC (ME) EFFECT .....	9
2.2.1. <i>Experimental results on Single-Phase multiferroic materials</i> .....	23
2.2.2. <i>Experimental results on Two-Phase systems</i> .....	25
2.2.3. <i>Resonance effects</i> .....	41
2.2.4. <i>Nanostructures</i> .....	52
<b>3. APPLICATIONS .....</b>	<b>54</b>
3.1. PHASE SHIFTERS .....	56
3.2. CIRCULATORS .....	59
3.3. FILTERS .....	62
3.4. ISOLATORS .....	65
3.5. MINIATURE ANTENNAS .....	70
3.5.1. <i>Microstrip Antennas</i> .....	71
3.5.2. <i>Miniature antennas using ferrites</i> .....	74
3.6. ELECTRICALLY TUNABLE MAGNETIC BASED PASSIVE COMPONENTS USING MAGNETOELECTRIC (ME) COUPLING .....	82
<b>4. SUMMARY AND OUTLOOK .....</b>	<b>95</b>
<b>5. ACKNOWLEDGMENTS .....</b>	<b>97</b>

## 1. Introduction

Low loss varieties of ferrites, a special class of magnetic materials using Fe as a constituent, find a plethora of applications in passive microwave components such as isolators, circulators, phase shifters, and miniature antennas operating at a wide range of frequencies (1–100 GHz) and also as magnetic recording media. Miniaturization of the passive components could also become possible owing to high magnetic susceptibility of ferromagnets coupled with high dielectric permittivity of some ferroelectrics. Fundamentals of ferrite materials, connecting chemical, structural, and magnetic properties have been discussed in Part 1 of this review.<sup>1</sup> If the strain which changes the magnetic properties of a ferrimagnetic material is transmitted from a piezoelectric material that is in contact with the ferrimagnet, the electric field applied across the piezoelectric material can be used to tune the magnetic properties opening up the possibility for a whole host of electrically tunable microwave passive components. The same behavior, albeit to a much lesser degree, can be obtained in materials with magneto-electric coupling dubbed the multiferroics. However, the strength of this coupling is not expected to compete with that achievable in two-phase systems involving separate piezoelectric and ferromagnetic constituents. We should mention that piezoelectric materials are those that respond to applied electric field by change in dimensions or vice versa. Piezoelectric materials and ferrimagnets are a subclass of oxides lacking centrosymmetry. Materials lacking centrosymmetry also exhibit nonlinear optical properties which have been useful in areas such as optical communication and signal processing. Miniaturization of the passive components could also become possible owing

to high magnetic susceptibility of ferromagnets coupled with high dielectric permittivity of ferroelectrics.

In this review, operational principles of microwave passive magnetic components, including fundamentals of magnetoelectric coupling and its use for tuning magnetic properties with electric field, followed by various applications such as phase shifters, circulators, isolators, filters, and ferrite antennas are discussed.

## **2. Principles of operation of microwave passive magnetic components**

In order to fully understand the design considerations and motivations behind certain ferrites, it is essential to have at least a working knowledge of the principles of operation of passive components intended for microwave applications. In the following section, the basis for the common denominator in passive components, the Faraday rotation, is discussed. Next, an important effect that allows electrical tuning of the magnetic properties of materials, magnetoelectric effect, is reviewed.

### **2.1. Faraday rotation**

The Faraday effect is a fundamental property of ferrite materials that are magnetized parallel to the direction of propagation. This effect can be used to achieve circulator action in a quasi-optical geometry, which is especially useful for millimeter-wave applications. Discovered by Michael Faraday in 1845, the Faraday rotation is a magneto-

optic effect caused by an interaction between linearly polarized electro-magnetic (EM) wave and a magnetic field applied or inherent to the material. The rotation of the plane of polarization is proportional to the intensity of the component of the magnetic field in the direction of the EM wave and the length of the sample. A linearly polarized beam of EM wave having a unique electric field  $E$ -vector direction can be decomposed into two circularly polarized beams of equal intensity. These right- and left-circularly polarized beams propagate simultaneously, but are independent of each other (orthogonal). In a magnetic field the medium of propagation becomes electromagnetically active producing different refractive indices/dielectric constants for the two beams so that they travel at different phase velocities. When the two beams exit the material they have a different phase relationship, which manifest in a rotation of the  $E$ -vector of the combined beams.

In order to provide a macroscopic description of the ferrite material in microwave radiation one should solve Maxwell's equations for wave propagation in such a ferrimagnetic medium. Maxwell's equations for ferrites can be written in phasor form as follows:

$$\nabla \times \mathbf{E} = -j\omega[\mu]\mathbf{H}$$

Equation 1

$$\nabla \times \mathbf{H} = j\omega\epsilon\mathbf{E}$$

Equation 2

$$\nabla \cdot \mathbf{D} = 0$$

Equation 3

$$\nabla \cdot \mathbf{B} = 0$$

**Equation 4**

where  $[\mu]$  is the permeability tensor defined in Equation 38 in Part 1 [1] and  $\varepsilon$  is the permittivity of the ferrite. Solving these equations for plane waves in the form of electric and magnetic fields  $\mathbf{E} = \mathbf{E}_0 e^{-j\beta z}$  and  $\mathbf{H} = \mathbf{H}_0 e^{-j\beta z}$  propagating along the  $z$  direction and having a propagation constant  $\beta$  leads to the following expressions for right-hand circularly polarized (RHCP) and left-hand circularly polarized (LHCP) electric and magnetic fields:

$$\begin{aligned} \mathbf{E}_+ &= E_0 (\hat{x} - j\hat{y}) e^{-j\beta_+ z} \\ \mathbf{H}_+ &= H_0 Y_+ (j\hat{x} + \hat{y}) e^{-j\beta_+ z} \end{aligned} \quad (\text{for RHCP})$$

**Equation 5**

$$\begin{aligned} \mathbf{E}_- &= E_0 (\hat{x} + j\hat{y}) e^{-j\beta_- z} \\ \mathbf{H}_- &= H_0 Y_- (-j\hat{x} + \hat{y}) e^{-j\beta_- z} \end{aligned} \quad (\text{for LHCP})$$

**Equation 6**

where  $Y_+ = \frac{\omega\varepsilon}{\beta_+} = \sqrt{\frac{\varepsilon}{\mu + \kappa}}$  and  $Y_- = \frac{\omega\varepsilon}{\beta_-} = \sqrt{\frac{\varepsilon}{\mu - \kappa}}$  are the corresponding wave admittances, and  $\mu$  and  $\kappa$  are the Polder permeability tensor elements defined in Equation 39 and Equation 40 in Part 1,[1] respectively. As seen from these expressions RHCP and LHCP plane waves propagate through the ferrite material with different propagation constants. Also it is seen that for RHCP waves ferrite can be represented with an effective permeability  $\mu + \kappa$ , while for an LHCP wave it can be represented with  $\mu - \kappa$ .

Let us now consider a linearly polarized electric field at  $z=0$ , represented as the sum of an RHCP and an LHCP wave:

$$\mathbf{E}|_{z=0} = \hat{x}E_0 = \frac{E_0}{2}(\hat{x} - j\hat{y}) + \frac{E_0}{2}(\hat{x} + j\hat{y})$$

Equation 7

This total field, taking into account that RHCP component will propagate in the  $z$  direction as  $e^{-j\beta_+z}$  and LHCP component as  $e^{-j\beta_-z}$ , will equal to

$$\mathbf{E} = E_0 \left\{ \hat{x} \cos \left[ \frac{(\beta_+ - \beta_-)}{2} z \right] - \hat{y} \sin \left[ \frac{(\beta_+ - \beta_-)}{2} z \right] \right\} e^{-j \left( \frac{\beta_+ + \beta_-}{2} \right) z}$$

Equation 8

As can be seen Equation 8 the polarization rotates as the wave propagates along the  $z$ -axis. At a given point along the  $z$ -axis the angle of polarization measured from the  $x$ -axis is given by

$$\phi = \tan^{-1} \frac{E_y}{E_x} = \tan^{-1} \left\{ -\tan \left[ \frac{(\beta_+ - \beta_-)}{2} z \right] \right\} = - \left( \frac{\beta_+ - \beta_-}{2} \right) z$$

Equation 9

which is the mathematical expression for Faraday rotation. As can be discerned from Equation 9 for a fixed position along the  $z$ -axis the polarization angle is fixed, while for a circularly polarized wave the polarization rotates with time. According to Equation 39 and Equation 40 in Part 1,[1] for  $\omega < \omega_0$ ,  $\mu$  and  $\kappa$  are both positive and  $\mu > \kappa$ . Then  $\beta_+ > \beta_-$  and from Equation 9 it is seen that  $\phi$  becomes more negative as  $z$  increases implying that the polarization rotates as we look in the  $+z$  direction. Reversing of the magnetic bias



( $H_0$ ) direction changes the sign of  $\kappa$  which in turn changes the direction of rotation to a clockwise one. Similarly, for +z bias a wave traveling in the  $-z$  direction will rotate its propagation clockwise if we look in the direction of propagation,  $-z$ . So, the polarization of a wave traveling from  $z = 0$  to  $z = L$  and back again to  $z = 0$  rotates by  $2\phi$ , where  $\phi$  is expressed by Equation 9 for  $z = L$ .

## 2.2. Magnetoelectric (ME) effect

Multiferroics are materials or structures where different ferroic orders such as ferroelectric, ferromagnetic/antiferromagnetic, and ferroelastic coexist in one material. In multiferroic magnetoelectrics, a dielectric polarization can be induced by an external magnetic field or vice versa, a magnetic moment can be induced by an external electric field. This phenomenon is described as the magnetoelectric effect (ME).<sup>2</sup> Using the ME coefficient  $\alpha$ , the electric polarization  $\mathbf{P}$  and the magnetization  $\mathbf{M}$  can be written as

$$\mathbf{P} = \varepsilon_0 \chi_e \mathbf{E} + \alpha \mathbf{H}$$

Equation 10  
and

$$\mathbf{M} = \chi_m \mathbf{H} + \frac{1}{\mu_0} \alpha^T \mathbf{E}$$

Equation 11

where  $\chi_e$  is the dielectric susceptibility,  $\chi_m$  is the magnetic susceptibility, and  $\alpha^T$  is the transpose of  $\alpha$ . It should be mentioned that Equation 10 and Equation 11 can be derived directly from Maxwell's equations and the correction terms in general have magnitudes on the order of  $1/c$ , where  $c$  is the speed of light, making it very hard to observe the ME effect. In three dimensions, these equations are usually matrix equations where the

susceptibilities and  $\alpha$  are (3 x 3) matrices. Clearly, when  $\mathbf{E}=0$  the polarization is given by  $\mathbf{P} = \alpha\mathbf{H}$ , where  $\alpha$  is the second rank ME-susceptibility tensor. After substituting Equation 10 into the equation for displacement

$$\mathbf{D} = \varepsilon_0 \mathbf{E} + \mathbf{P}$$

Equation 12

and setting  $\mathbf{D}=0$  for open circuit condition, one obtains

$$\mathbf{E} = -\frac{\alpha}{\varepsilon_0(1 + \chi_e)} \mathbf{H} = -\frac{\alpha}{\varepsilon_0 \varepsilon_r} \mathbf{H}$$

Equation 13

where  $\varepsilon_r$  is the relative permittivity. The modified factor in Equation 13

$$(\alpha_E)_{ij} = \frac{\delta E_i}{\delta H_j} = -\frac{\alpha_{ij}}{\varepsilon_0 \varepsilon_r}$$

Equation 14

is called the ME voltage coefficient, which is the quantity generally measured during experiments.

The ME effect in single crystals is generally described using the Landau theory by writing the expansion of free energy of the system in S.I. units as<sup>3,4</sup>

$$F(\mathbf{E}, \mathbf{H}) = F_0 - P_i^S E_i - \mu_0 M_i^S H_i - \frac{1}{2} \varepsilon_0 \varepsilon_{ij} E_i E_j - \frac{1}{2} \mu_0 \mu_{ij} H_i H_j - \alpha_{ij} E_i H_j - \frac{1}{2} \beta_{ijk} E_i H_j H_k - \frac{1}{2} \gamma_{ijk} H_i E_j E_k - \dots$$

Equation 15

where  $P_i^s$  and  $M_i^s$  are the spontaneous polarization and magnetization,  $F_0$  is the field independent energy, and  $\varepsilon_{ij}$  and  $\mu_{ij}$  are the second ranked permittivity and permeability tensors, respectively. The fourth and the fifth terms represent the pure electrical and magnetic responses of the system, respectively. The sixth term describes the linear ME coupling via the second ranked tensor  $\alpha$ . The terms such as those with the third ranked tensors  $\beta_{ijk}$  and  $\gamma_{ijk}$  represent the higher order ME effects. The polarization and the magnetization of the system may then be obtained by differentiation of Equation 15 with respect to  $E_i$  and  $H_i$ , respectively:

$$P_i(\mathbf{E}, \mathbf{H}) = - \left. \frac{\partial F(\mathbf{E}, \mathbf{H})}{\partial E_i} \right|_{E_i=0} = P_i^s + \alpha_{ij} H_j + \frac{1}{2} \beta_{ijk} H_j H_k + \dots$$

Equation 16

$$\mu_0 M_i(\mathbf{E}, \mathbf{H}) = - \left. \frac{\partial F(\mathbf{E}, \mathbf{H})}{\partial H_i} \right|_{H_i=0} = \mu_0 M_i^s + \alpha_{ij} E_j + \frac{1}{2} \gamma_{ijk} E_j E_k + \dots$$

Equation 17

The ME response is limited by the geometric mean of the diagonalized permittivity and permeability tensors

$$\alpha_{ij}^2 \leq \mu_0 \varepsilon_0 \mu_{ij} \varepsilon_{ij}$$

Equation 18

This condition is obtained by ignoring the higher order terms and forcing the sum of the fourth and the fifth terms and the linear ME term to be less than zero. The ME effect, therefore, is expected to be large in only ferroelectric and/or ferromagnetic materials.

However, we must note that not all the ferroelectrics have large  $\varepsilon_{ij}$  and ferromagnets do not necessarily possess large  $\mu_{ij}$ , and ME effect is not restricted to multiferroic materials.

The linear ME effect is usually very small as seen from Equation 18 since most materials have either small  $\varepsilon_{ij}$  or  $\mu_{ij}$ . However, there is no limitation on the higher order ME terms, which in some materials may be larger than the linear term.<sup>5</sup> The nonlinear terms were suggested to strengthen in magnetic materials with reduced dimensionality.<sup>3</sup>

The ME effect is observed in two classes of materials: single phase multiferroic materials possessing simultaneously both ferroelectric and ferromagnetic properties and composites consisting of ferroelectric and ferromagnetic phases. The ME effect in the single phase materials arises from the long range interaction between the atomic moments and electric dipoles in ordered magnetic and ferroelectric sublattices. The realizable ME coefficient in single phase materials is, however, very small (1-20 mV/cm-Oe) and not sufficient for practical applications. This is because the ligand-field hybridization of a transition metal cation by its surrounding anions, which is often responsible for conventional ferroelectricity, requires that the  $d$  orbitals of the cations be unoccupied, thus precluding ferromagnetism.<sup>6, 7</sup> As a result single-phase multiferroics often exhibit only weak magnetization and/or ferroelectricity. Moreover, ME effect in most of these single phase materials is observed only at low temperatures as either ferromagnetic (or antiferromagnetic) or ferroelectric transition temperature is very low. Composite materials, on the other hand, provide an alternative strategy which makes use of indirect coupling via mechanical strain between the materials of two different phases:

ferroelectric and ferromagnetic (or antiferromagnetic or ferrimagnetic such as ferrites). Mechanical deformation of the magnetostrictive phase results in polarization in the piezoelectric phase. With the possibility of independent optimization of the two different phases for room temperature operation, the limiting condition described in Equation 18 is lifted. As a result, the ME effect in composites may be more than several orders of magnitude higher than that in single phase materials, the latter forming actually the basis for multiferroics. Such composites can be implemented in the form of "multilayers" consisting of alternating layers of the ferroelectric phase and the ferro- or ferri-magnetic phase as illustrated in Figure 1 (a). Bilayers and multilayers of composites are especially promising due to their low leakage current and superior poling properties. In multilayers, however, the magnetoelectric coupling effect is weakened due to the clamping effect of the substrate,<sup>8</sup> unless the multilayers are fabricated as free standing membranes. Alternatively, heterostructures consisting of nanopillars of the ferro/ferrimagnetic phase embedded in a ferroelectric matrix can be implemented as shown in Figure 1 (b).

In the discussion of linear and higher order magnetoelectrical coupling, we have so far ignored the effects of strain. However, inclusion of strain arising from piezomagnetism and magnetostriction would introduce cross terms in Equation 15 that are proportional to strain and have linear and/or quadratic dependence on  $H$ . Similarly, additional terms would arise from piezoelectricity and electrostriction, having dependences on  $E$ . Even mixed terms involving strain,  $H$ , and  $E$  would appear. The effects of strain are significant and in some cases may even dominate, which is actually desired in laminated two-layer

composites. To reiterate, in the two-phase materials, the indirect coupling of ferroelectric and ferromagnetic materials by strain is not restricted by Equation 18.

Most ferromagnetic materials exhibit magnetostriction, which describes a change in strain as a quadratic function of the applied magnetic field. This change in the strain may induce polarization in the ferroelectric phase, which is in contact with the ferromagnetic/antiferromagnetic/ferromagnetic phase (ideally in atomic registry), through the piezoelectric effect.

The polarization induced in the ferroelectric phase is given in terms of stress by

$$P_i = d_{ijk} T_{jk} ,$$

Equation 19

where  $d_{ijk}$  are the piezoelectric stress coefficients (can be represented by a 3 x 6 matrix) and  $T_{jk}$  are the stress tensor elements (represented by a 6 x 1 matrix) that are related to strain through the compliance tensor  $S_{ijkl}$  (represented by a 6 x 6 matrix) as

$$S_{ij} = s_{ijkl} T_{kl} ,$$

Equation 20

where  $S_{ij}$  are the strain tensor elements (represented by a 6 x 1 matrix). The inverse effect, where the strain is developed, *e.g.* as a result of an applied electric field, may also be written in terms of the electric field  $\mathbf{E}$  as

$$S_{ij} = d_{ijk} E_k .$$

Equation 21

It should be mentioned that the matrix representations of all these tensors become possible since tensor indices can be decreased by replacing two indices by a single index according to  $xx = 1, yy = 2, zz = 3, zy = yz = 4, xz = zx = 5, yx = xy = 6$ . For example  $d_{ijk}$  (where  $i, j, k$  all can take values of x, y, and z, or 1, 2, and 3) can be transformed to  $d_{il}$  (where  $i = 1, 2, 3$  and  $l = 1, 2, \dots, 6$ ) which can be represented by a 3 x 6 matrix. Similarly  $T_{kl}$  can be transformed to  $T_m$  ( $m = 1, 2, \dots, 6$ ).

Assuming no hysteresis, the strain induced due to magnetostriction is expressed as

$$\mathbf{S} = \lambda^{(\text{MS})} \mathbf{H}^2$$

#### Equation 22

where  $\mathbf{S}$  is the strain,  $\mathbf{H}$  is the applied magnetic field, and  $\lambda^{(\text{MS})}$  is the spontaneous magnetostriction tensor. Although there are several magnetostriction effects, such as volume magnetostriction, dipolar magnetostriction, and the Wiedemann effect,<sup>9</sup> usually only the longitudinal (or also referred to as Joule) magnetostriction is considered. The highly anisotropic strain resulting from magnetostriction depends strongly on the magnitude of the applied magnetic field and reaches a limiting value when magnetization saturates. The sign of the magnetostriction may be positive or negative depending on the crystallographic direction in the material. Assuming that the demagnetized state before the application of the magnetic field is isotropic, the limiting magnetostriction measured along the field direction is called the saturation magnetostriction. In isotropic cubic crystals under applied magnetic field, change in the crystal length in one direction saturates at a value  $\Delta l$  given by  $\Delta l/l = (3/2)\lambda_s^{(\text{MS})}(\cos^2 \theta - 1/3)$ , where  $l$  is the original length of the specimen,  $\theta$  is the angle between the magnetization and the direction in

which  $\Delta l$  is measured, and  $\lambda_s^{(MS)}$  is the longitudinal saturation magnetostriction.<sup>10</sup> To eliminate the effects of anisotropy in the demagnetized state, the magnetostriction perpendicular to the field direction ( $\lambda_{\perp}^{(MS)}$ ) in addition to that along the field direction ( $\lambda_{\parallel}^{(MS)}$ ) should also be measured and the saturation magnetostriction independent of the demagnetized state is given by

$$\lambda_s^{(MS)} = \frac{2}{3}(\lambda_{\parallel}^{(MS)} - \lambda_{\perp}^{(MS)})$$

#### Equation 23

For a large ME effect, the magnitude of the magnetostriction is required to be as large as possible. Table 1 lists saturation magnetostriction values for some materials at room temperature.<sup>11</sup>

As expressed in Equation 22, magnetostriction is a nonlinear magnetomechanical effect, whereas piezoelectricity is a linear electromechanical effect as Equation 21 indicates. This makes the ME effect in composites a nonlinear effect and causes a hysteretic behavior unlike in the single phase materials. However, to make use of composite materials in linear device applications, linearity may be achieved by applying a magnetic field bias so that the magnetostriction around the bias field may be considered as a linear effect. At a given bias magnetic field  $\mathbf{H}_0$  magnetostriction can lead to pseudo-piezomagnetism over a small range of magnetic fields, where the slope of the strain vs. the applied magnetic field curve can be approximated as a constant. At this particular  $\mathbf{H}_0$ , the strain may be expressed as

$$\mathbf{S} = \mathbf{qH}$$



Equation 24

where  $\mathbf{q}$  is the pseudo-piezomagnetism tensor of dimensions 6x3. Piezomagnetism is usually defined as the appearance of a magnetic moment on the application of stress.

Equation 24 basically defines the inverse effect, which may be considered as the physical property that relates the applied magnetic field to the resultant strain using the same piezomagnetism tensor.

For a given material one can then write a general expression for the strain taking into account the contributions from the stress field (elasticity), the electric field (piezoelectricity), and the magnetic field (piezomagnetism) as

$$\mathbf{S} = \mathbf{sT} + \mathbf{dE} + \mathbf{qH}$$

Equation 25

which can be used to derive the ME voltage coefficients in composites having different configurations as described in Harshé *et al.*<sup>12</sup>

For the two-phase systems, the physical properties are determined by the interaction between the constituents as well as by their individual properties. Some effects, which are already present in the constituents may be averaged or enhanced for the overall system. However, the ME effect is among the novel effects that arises from the product properties originating through the interaction between the two phases. The ME effect can be achieved by coupling a piezoelectric (or electrostrictive) material and a piezomagnetic (or magnetostrictive) material via a good mechanical contact. Such a two-phase system may be achieved in the form of composites, laminates, or epitaxial layers. An applied

magnetic field induces strain in the magnetostrictive constituent, which can be transferred to the piezoelectric constituent to the extent allowed by the mechanical coupling between the two, and the transferred strain induces an electric polarization in the piezoelectric constituent. The inverse effect is also possible, where an electric field may be applied to the piezoelectric material to induce strain, which is then transferred to the magnetostrictive material, where it affects the magnetization. The ME effect can crudely be described as the product of the piezoelectric and magnetostrictive responses of the constituents:

$$\text{ME effect} = \left( \frac{\text{Electrical}}{\text{Mechanical}} \right)_{\text{piezoelectric}} \left( \frac{\text{Mechanical}}{\text{Magnetic}} \right)_{\text{magnetostrictive}}$$

**Equation 26**

Assuming that there exists a perfect coupling between the two phases and the Young's moduli for the two-phases are equal the ME voltage coefficient can be written as<sup>13</sup>

$$\left( \frac{dE}{dH} \right)_{2-Phase} = \left( \frac{dx}{dH} \right)_{2-Phase} \left( \frac{dE}{dx} \right)_{2-Phase} = f_v \left( \frac{dx}{dH} \right)_m \left( \frac{dE}{dx} \right)_p$$

**Equation 27**

where  $\frac{dx}{dH}$  is the change in length per unit applied magnetic field,  $\frac{dE}{dx}$  is the change in the electric field per unit dimension, and  $f_v = {}^mV / {}^pV$  is the volume fraction of the magnetostrictive constituent with  ${}^mV$  and  ${}^pV$  being the volumes of the magnetostrictive ( $m$ ) and piezoelectric ( $p$ ) constituents, respectively. This expression can also be written in terms of the strain  $S$  as<sup>14</sup>

$$\alpha_E = \left( \frac{dE}{dH} \right)_{2-Phase} = f_V \left( \frac{dS}{dH} \right)_m (1 - f_V) \left( \frac{dE}{dS} \right)_p = f_V \left( \frac{dS}{dH} \right)_m (1 - f_V) (g_{33} C_{33})_p$$

Equation 28

The last part in Equation 28 is obtained using  $dE = g_{33}dT$  and  $dT = C_{33}dS$ , where the electric field has been assumed to be in the  $z$ -direction with  $g_{33}$  and  $C_{33}$  being the appropriate piezoelectric voltage and the stiffness coefficients, respectively, of the piezoelectric phase. Evidently, piezoelectric materials with large  $g_{33}$  and  $C_{33}$  coefficients are chosen for the two-phase systems to increase the ME effect. In other words, the dynamic coefficient  $dE/dS$  in Equation 28 should be as large as possible. The relationship between the strain  $S$  and the applied electric field  $E$  is described as the electrostriction, which is a second order electromechanical effect. More conveniently, the coupling between the electric-field induced strain and the polarization is expressed using the electrostriction tensor,  $\mathbf{Q}$ , as<sup>15</sup>

$$\mathbf{S} = \mathbf{Q}\mathbf{P}^2$$

Equation 29

where  $\mathbf{P}$  is the polarization tensor. The piezoelectric coefficients can be described as the electrostriction biased by polarization. For example for  $\langle 111 \rangle$  orientation the longitudinal ( $d_{33}$ ) and transverse ( $d_{31}$ ) piezoelectric coefficients are given by<sup>16</sup>

$$d_{33} = \frac{2}{3} \varepsilon_0 \varepsilon_{33}^T P_s (Q_{11} + 2Q_{12} + 2Q_{44})$$

$$d_{31} = \frac{2}{3} \varepsilon_0 \varepsilon_{33}^T P_s (Q_{11} + 2Q_{12} - Q_{14})$$

Equation 30

where  $Q_{11}$ ,  $Q_{12}$ , and  $Q_{44}$  are the electrostriction coefficients,  $P_s$  is the spontaneous polarization,  $\epsilon_0$  is the permittivity of vacuum, and  $\epsilon_{33}^T$  is the relative dielectric permittivity at constant stress. As the dynamic coefficient  $dE/dS$  in Equation 28 is desired to be large for a strong ME effect, materials with large piezoelectric, and therefore, large electrostriction constants should be chosen for the piezoelectric phase. Studies on ME coupling-based devices, therefore, usually employ piezoelectric materials such as BaTiO<sub>3</sub>, Ba<sub>0.7</sub>Sr<sub>0.3</sub>TiO<sub>3</sub>, PbZr<sub>0.45</sub>Ti<sub>0.55</sub>O<sub>3</sub>, and Pb(Mg<sub>1/3</sub>Nb<sub>2/3</sub>)O<sub>3</sub>-PbTiO<sub>3</sub>, either in single crystal or ceramic form, noting that in single crystal form, which may be more difficult to obtain, they exhibit higher piezoelectricity.

For theoretical estimates of  $\alpha_E$  in 2-phase systems the magnetostriction  $\lambda^{(MS)}$  is an important parameter. In order to maximize the ME coefficient, the applied bias field  $\mathbf{H}$  must correspond to the maximum in the slope of  $\lambda^{(MS)}$  vs.  $\mathbf{H}$  characteristics, i.e.  $dS/dH$  in Equation 28 should be at a maximum. Magnetostriction coefficients as a function of the bias field may be measured for different directions using various techniques utilizing the strain-gauge method, dilatometers, optical interferometry, etc.<sup>9</sup> The measured values then can then be fed into Equation 28 to evaluate the ME effect for perfect mechanical contact between the two constituents.

Let us now look at the expressions for the ME coefficients in a 2-phase system with a piezoelectric and a magnetostrictive layer connected only in two directions, i.e. a single contact plane. The procedure for estimating the ME coefficient is described by Harshé *et al.*<sup>12</sup> Using Equation 15 the total strain at the interface is first calculated for an applied

magnetic field, and the stress-strain relationship is used for a set of certain boundary conditions at the interface. The electric field is then related to stress using the appropriate boundary conditions. For example, for a free body with both phases perfectly bonded together the boundary conditions are such that no stresses are present along the direction perpendicular to the bonding plane, and the strains in both constituents along the transverse directions are equal. Also, the total force acting on the system along the transverse directions and the electric displacement vector in the piezoelectric layer under open circuit conditions are both zero. Using a 3-dimensional coordinate system and defining the directions as indicated in **Figure 2** the transverse ( $zx$ ) and the longitudinal ( $zz$ ) ME coefficients can be obtained as:

$$(\alpha_E)_{zx} = \frac{\delta E_z}{\delta H_x} = - \frac{2 {}^m q_{xx} {}^p d_{zx} {}^m V}{\left( {}^m s_{xx} + {}^m s_{xy} \right) \left( {}^p \epsilon_{zz}^T \right) {}^p V + \left( {}^p s_{xx} + {}^p s_{xy} \right) \left( {}^p \epsilon_{zz}^T \right) {}^m V - 2 \left( {}^p d_{zx} \right)^2 {}^m V}$$

$$(\alpha_E)_{zz} = \frac{\delta E_z}{\delta H_z} = - \frac{2 {}^m q_{zx} {}^p d_{zx} {}^m V}{\left( {}^m s_{xx} + {}^m s_{xy} \right) \left( {}^p \epsilon_{zz}^T \right) {}^p V + \left( {}^p s_{xx} + {}^p s_{xy} \right) \left( {}^p \epsilon_{zz}^T \right) {}^m V - 2 \left( {}^p d_{zx} \right)^2 {}^m V}$$

**Equation 31**

where  $s_{ij}$  are the compliances,  $q_{ij}$  are the piezomagnetic coefficients,  $d_{zx}$  is the piezoelectric coefficient,  $\epsilon_{zz}^T$  is the dielectric permittivity at constant stress,  $V$  is the volume, and superscripts  $m$  and  $p$  denote the magnetostrictive and piezoelectric phases, respectively. The piezomagnetic coefficients  $q_{ij} = d\lambda_{ij}^{(MS)}/dH$  are usually determined from the measured magnetic field dependence of the longitudinal ( $\lambda_{zz}^{(MS)}$ ) and transverse ( $\lambda_{zx}^{(MS)}$ ) magnetostriction.<sup>17</sup> Since only the electric field across the piezoelectric layer is measured, the ME coefficients  $\alpha_E$  are usually defined per unit thickness of the

piezoelectric phase. Table 2 shows the material parameters used to calculate the ME voltage coefficients in CoFe<sub>2</sub>O<sub>4</sub> - BaTiO<sub>3</sub> and CoFe<sub>2</sub>O<sub>4</sub> - PZT bilayer structures. The ME voltage coefficients calculated for different volume fractions of the magnetostrictive and piezoelectric phases are listed in Table 3.<sup>12</sup>

The ME coefficients given above in Equation 31 are for the configurations indicated in Figure 2, where the electric field is always along the *z*-direction. Therefore, we have two cases, where the magnetic field is either along the *z* or the *x*-direction. Other two cases when the electric field is in the sample plane (*x-y* plane) yield the same expressions for  $\alpha_E$  as in Equation 31, but with the coefficients  ${}^m q_{ij}$  and  ${}^p d_{zx}$  replaced with the appropriate ones.<sup>12</sup>

The strength of ME coupling is measured directly by mainly two different methods: by monitoring either the electric field induced change in magnetization or magnetic field induced change in electric polarization (see Equation 17). For magnetic field induced change in electric field, usually the ME voltage coefficient (or the electrical ME coefficient)  $(\alpha_E)_{ij} = \delta E_i / \delta H_j$  (in units of V/A in SI units and mV/cm-Oe in cgs units) is measured. The magnetization change under applied field is also used to obtain the magnetic ME coefficient  $(\alpha_M)_{ij} = \mu_0 \delta M_i / \delta E_j$  (in units of s/m in SI units and Gauss-cm/V in cgs units where  $\mu_0 = 1$ ). Similarly, the shift in the ferromagnetic resonance static field *H* for a given frequency, or the shift in the ferromagnetic resonance frequency (*f<sub>r</sub>*) under a fixed applied field is also measured to evaluate the ME coupling:  $\alpha_f = \delta H / \delta E = (2\pi/\gamma) \delta f_r / \delta E$  (in units of Oe-cm/kV, where  $\gamma = 2\pi \times 2.8$  MHz/Oe is the

electron gyromagnetic ratio) and generally the constant  $\delta f_r/\delta E$  is reported in units of MHz-cm/kV. To measure the ME voltage coefficients, a DC bias magnetic field is applied along with a small AC magnetic field and the AC voltage induced across the piezoelectric material is measured. The AC magnetic field is applied in the same direction as the DC field using a pair of Helmholtz coils. One of the major challenges during measurements is to make the samples sufficiently insulating to prevent leakage currents. ME coupling can be measured also indirectly by simply recording the changes in either the magnetization near a ferroelectric transition temperature or the dielectric constant near a magnetic transition temperature. The same measurement scheme can be applied to the 2-phase systems where the measurements could be done near the transition temperature of any one of the constituents.

### 2.2.1. Experimental results on Single-Phase multiferroic materials

The advantage of multiferroics is the ME coupling in the same material. The violation of time-reversal symmetry was first explicitly shown for antiferromagnetic  $\text{Cr}_2\text{O}_3$ , which therefore was predicted to exhibit linear ME coupling.<sup>18</sup> A nonzero linear ME coefficient, *i.e.* magnetic field induced polarization,<sup>19,20</sup> was then confirmed for  $\text{Cr}_2\text{O}_3$ , as well as the electrical field induced magnetization,<sup>21,22</sup> below the antiferromagnetic Néel temperature ( $T_N$ ) of 307 K. The ME coupling coefficient peaked near 275 K at  $\alpha_M = \mu_0 \delta M/\delta E = 4.13 \text{ ps m}^{-1}$ ,<sup>[23]</sup> which is really very small for any practical application. The discouraging results in  $\text{Cr}_2\text{O}_3$  led to a search for alternative single phase compounds. Subsequently, ME effect in compounds such as  $\text{Ti}_2\text{O}_3$ ,<sup>24</sup>  $\text{GaFeO}_3$ ,<sup>25</sup>  $\text{Gd}_2\text{CuO}_4$ ,  $\text{Sm}_2\text{CuO}_4$ ,  $\text{KNiPO}_4$ ,  $\text{LiCoPO}_4$ ,<sup>26</sup>  $\text{LiNiPO}_4$ ,<sup>27, 28</sup>  $\text{BaMnF}_4$ ,<sup>29</sup> molybdate  $\text{Tb}(\text{MO}_4)_3$ ,<sup>30</sup> boracites  $\text{Ni}_3\text{B}_7\text{O}_{13}\text{I}$ ,

$\text{FeB}_7\text{O}_{13}\text{Cl}$ , and  $\text{Mn}_3\text{B}_7\text{O}_{13}\text{Cl}$ ,<sup>31, 32</sup> solid solutions such as  $\text{PbFe}_{0.5}\text{Ta}_{0.5}\text{O}_3$  and  $\text{PbFe}_{0.5}\text{Nb}_{0.5}\text{O}_3$ ,<sup>33, 34</sup> orthorhombic manganites  $\text{GdMn}_2\text{O}_5$ ,<sup>35</sup>  $\text{TbMn}_2\text{O}_5$  and  $\text{TbMnO}_3$ ,<sup>36</sup> hexaferrite  $\text{Ba}_{0.5}\text{Sr}_{1.5}\text{Zn}_2\text{Fe}_{12}\text{O}_{22}$ ,<sup>37</sup> hexagonal perovskite  $\text{YMnO}_3$ ,<sup>38, 39</sup> monoclinic perovskite  $\text{BiMnO}_3$ ,<sup>40, 41</sup> spinel  $\text{CdCrS}_4$ ,<sup>42</sup> garnets such as YIG<sup>43</sup> and  $(\text{YBiPrLu})_3(\text{FeGa})_5\text{O}_{12}$ ,<sup>44</sup> has been observed. Relatively large ME coefficients were measured for  $\text{LiCoPO}_4$  ( $30.6 \text{ ps m}^{-1}$  at 4.2 K),<sup>45</sup>  $(\text{YBiLaPr})_3(\text{FeGa})_5\text{O}_{12}$  (substituted YIG) films ( $\sim 30 \text{ ps m}^{-1}$  at 294 K),<sup>46</sup> and  $\text{TbPO}_4$  ( $36.7 \text{ ps m}^{-1}$  at 1.92 K).<sup>47</sup> However, the magnitude of the ME effect is still very small for any practical device applications and or the compounds listed above exhibit multiferroicity only at very low temperatures, again rendering more or less useless in practical applications. In addition to  $\text{Cr}_2\text{O}_3$ , room temperature multiferroic behavior has been observed only for perovskite  $\text{BiFeO}_3$  (antiferromagnetic  $T_N \sim 643 \text{ K}$ , ferroelectric  $T_C \sim 1103 \text{ K}$ ) and its derivatives.<sup>48, 49, 50</sup> Strong multiferroic behavior ( $1 \mu_B$  magnetization per formula unit,  $\sim 60 \mu\text{C}/\text{cm}^2$  electric polarization) and ME coupling ( $3 \text{ V}/\text{cm-Oe}$ ) reported<sup>48</sup> for  $\text{BiFeO}_3$  triggered significant research activity albeit with some degree of controversy. These striking results, however, could not be reproduced by others and have been attributed<sup>51</sup> to measurement artifacts resulting from misvaluation of the film resistivity ( $10^9 \Omega \text{ cm}$  was stated in Ref. 48). In short, unfortunately, none of the multiferroic single phase materials provide a strong enough effect for practical applications. Among multiferroics of various crystal structures four major crystallographic types are distinguishable:<sup>4</sup> Perovskite (e.g.  $\text{BiFeO}_3$ ,  $\text{PbFe}_{0.5}\text{Nb}_{0.5}\text{O}_3$ ), hexagonal (e.g. manganites  $\text{REMnO}_3$  with  $\text{RE} = \text{Sc, Y, Gd, Tb, Ho, Er, Tm, Yb, Lu}$ ), boracite (e.g.  $\text{Me}_3\text{B}_7\text{O}_{13}\text{X}$  with  $\text{Me} = \text{Cr, Mn, Fe, Co, Cu, Ni}$  and  $\text{X} = \text{Cl, Br, I}$ ), and orthorhombic  $\text{BaMeF}_4$  (with  $\text{Me} = \text{Mg, Mn, Fe, Co, Ni, Zn}$ ) compounds. The



principle weaknesses of these single phase materials have their genesis in the limitation set by Equation 18. Table 4 lists ME coupling coefficients measured for various multiferroic single phase materials, which can be compared with those for some two-phase systems listed in Table 5.<sup>52,53,54,55,56,57,58,59,60,61,62,63,64,65,66,67,68,69,70,71</sup> The  $\alpha_M$  values for two phase systems [e.g.  $\sim 6 \times 10^{-8}$  s/m for a  $\text{La}_{0.7}\text{Sr}_{0.3}\text{MnO}_3/\text{PMN-PT}$  (001) bilayer<sup>72</sup>] are much larger than those observed for single-phase materials. For most of the two-phase materials where the ME coefficient  $\alpha_E$  is large the change of magnetization under applied electric field has not yet been investigated.

### 2.2.2. Experimental results on Two-Phase systems

As alluded to earlier, the alternative strategy to enhance the ME effect is to utilize indirect coupling via strain between two materials such as a ferromagnet (or ferrimagnet or antiferromagnet) and a ferroelectric. In this avenue, many systems involving composites, laminates, and epitaxial bilayers have been investigated. Several synthesis methods have been used for growing multiferroic composite materials in the bulk form, such as eutectic unidirectional solidification,<sup>73</sup> ceramic sintering,<sup>74</sup> hot molding,<sup>75</sup> tape casting,<sup>17</sup> and epoxy-bonded laminates.<sup>76,77,78,79,80</sup> For growth in the film form, pulsed laser deposition,<sup>8,81</sup> physical vapor deposition,<sup>82</sup> and sol-gel process<sup>83,84,85</sup> have been utilized. Since for multilayers, the condition described by Equation 18 is lifted, the constituents with the best piezoelectric and magnetostrictive properties for a particular application may be chosen to obtain enhanced ME effect. To observe the best coupling efficiency in multilayers, the mechanical coupling between the constituents should be as

close as possible to being perfect. The best interface bonding can naturally be achieved by epitaxial growth of at least one of the constituents on the other (for bilayers) required that they have a good lattice match and compatible crystal structures. In addition to the interface quality, the crystal orientation and layer thickness may also be controlled very accurately during epitaxial growth. However, to apply an electric field or measure the induced electric field directly across the piezoelectric layer (normal to the sample plane) a contact layer (metal or a conductive bridge layer) should be used at the interface unless the magnetostrictive constituent is conductive (such as the manganite  $\text{La}_{0.7}\text{Sr}_{0.3}\text{MnO}_3$ ), which is not the case for most ferrites. This contact layer may significantly degrade the efficiency of strain transfer between the ferromagnetic and ferroelectric phases. A succinct review of the experimental studies on particulate and laminated composites can be found in reviews such as 4 and 86. The ME voltage coefficients measured for some piezoelectric/magnetostrictive two-phase systems are tabulated in Table 5.

#### ***Composite systems:***

The first group of artificial ME composite materials has been produced at Philips Laboratories by combining the piezoelectric  $\text{BaTiO}_3$  with piezomagnetic  $\text{CoFe}_2\text{O}_4$  using unidirectional solidification of a eutectic composition of the two constituents.<sup>87</sup> These initial experiments revealed magnetic ME coefficients up to  $722 \text{ ps m}^{-1}$ , which is more than two orders of magnitude higher than that obtained for the single phase  $\text{Cr}_2\text{O}_3$  ( $4.13 \text{ ps m}^{-1}$ ). Using Equation 28 with the maximum optimistic parameter values, the maximum ME voltage coefficient can be estimated to be  $920 \text{ mV/cm-Oe}$  for the  $\text{BaTiO}_3$  -

CoFe<sub>2</sub>O<sub>4</sub> composite with  $f_V = 0.5$ , which is much larger than that observed experimentally due to imperfect interface coupling (see Table 5).

For enhancement of ME coupling, most of the investigations have focused on piezoelectric magnetostrictive composites, where the ME effect is described by Equation 26. Piezoelectric constituents used involved BaTiO<sub>3</sub> (BTO),<sup>88</sup> PbZr<sub>1-x</sub>Ti<sub>x</sub>O<sub>3</sub> (PZT),<sup>89</sup> Bi<sub>4</sub>Ti<sub>3</sub>O<sub>12</sub> (Aurivillius phase),<sup>90, 91</sup> polyvinylidene-fluoride (PVDF, also known as KYNAR® or HYLAR®),<sup>92, 93</sup> and P(Mg<sub>1/3</sub>Nb<sub>2/3</sub>)O<sub>3</sub>-PbTiO<sub>3</sub> or PMN-PT.<sup>94</sup> Due to commercial availability and large piezoelectric constants mostly PZT and PMN-PT materials in ceramic form were employed. The strain that could be achieved by single crystal PMN-PT has been shown to be as large as 1.7 %.<sup>94</sup> Therefore, PZT and PMN-PT in single crystal form are very promising for devices utilizing the ME effect. As in most novel applications, a large electrical field induced change in magnetization in the ferrites for tuning the ferromagnetic resonance is desired. Aside from ferrites such as CoFe<sub>2</sub>O<sub>4</sub> and hexaferrites, manganites [La<sub>x</sub>(Ca,Sr)<sub>1-x</sub>MnO<sub>3</sub>],<sup>17, 95</sup> CoPd,<sup>96</sup> LiF<sub>5</sub>O<sub>8</sub>,<sup>86</sup> YIG,<sup>76</sup> permendur,<sup>79</sup> and terfenol-D alloys (terbium-dysprosium iron, Tb<sub>1-x</sub>Dy<sub>x</sub>Fe<sub>2</sub>)<sup>97,98,99</sup> have been considered as the magnetostrictive constituents. As Terfenol-D is among the materials that display the highest magnetostriction ( $\sim 2 \times 10^{-3}$ ), PZT/Terfenol-D composites have been frequently studied in search for the largest ME coupling coefficient. However, PZT/ferrite composites are needed for microwave device applications, which will be discussed in Section 3.

#### ***Laminated composites:***

As alluded to earlier, to maximize the magnitude of the ME effect, the strain transfer between the piezoelectric and magnetostrictive constituents should ideally be lossless. However, in composites, the ME effect is limited by the quality of the interface in addition to the material quality of each layer. This is the reason why the theory overestimates the coupling coefficient using Equation 28 as compared to experiments in the composites, where use of different sintering procedures, dopants, grain sizes, and mole fractions did not provide any relief. The problem is multifaceted such as the chemical reactions between the constituents during the high temperature sintering process of the particulate composites, mechanical defects in the form of pores or cracks due to imperfect lattice matching between the two constituents, presence of multiple orientations in one or both constituents that have different response along different crystal orientations, and AC magnetic field induced Eddy currents or the low resistivity of the magnetostrictive material that makes the electrical poling difficult, resulting in current leakage.<sup>4</sup> In addition, when the concentration of the piezoelectric phase is increased in the composites to enhance the ME coupling, the ferromagnetic resonance is broadened, obscuring the electric field effects on the resonance field. These obstacles could be overcome by using laminated instead of particulate composites. In laminated composites, the two constituents can be prepared independently and then bonded together; therefore the chemical reaction between them is avoided. Ideally, the constituents of the laminates should be in atomic registry for maximum transfer of strain but this is not easy and may not even be possible for a given laminate pair. Additionally, when contact layers are used in between the ferroelectric and ferromagnetic constituents to have a uniform electric field normal to the bilayer (or multilayer) plane the mechanical coupling is weaker. Also

of concern is the substrate clamping which reduces the ME coupling unless floating structures, such as those used in the micro-electro-mechanical-systems (MEMs) technology, are employed. The caveat is that doing so would make the device very sensitive to g-forces and limit its applications.

In laminated composites, the ME response is determined by the respective thicknesses of constituents, the number of layers, the nature of bonding between the constituents, the orientation of the constituents, and the applied fields in addition to the material parameters. The bonding is naturally very critical to achieve good mechanical coupling. In order to take into account the actual interface conditions between the magnetostrictive and the piezoelectric units, an interface coupling parameter has been introduced to estimate longitudinal and transverse ME coupling coefficients.<sup>100</sup> The coupling coefficient was found to depend on the choice of constituents. For instance the coupling of PZT with  $\text{NiFe}_2\text{O}_4$  was found to be nearly perfect, while it was very poor with  $\text{La}_{0.7}(\text{Sr}, \text{Ca})_{0.3}\text{MnO}_3$  and  $\text{CoFe}_2\text{O}_4$ .<sup>17,57,100</sup> The substitution of Co and Ni with Zn was found to increase the ME coupling.<sup>100</sup>

It should be mentioned that even though manganites such as  $\text{La}_{0.7}\text{Sr}_{0.3}\text{MnO}_3$  (LSMO) and  $\text{La}_{0.7}\text{Ca}_{0.3}\text{MnO}_3$  (LCMO) are potential candidates for ME composites because of high magnetostriction and metallic conductivity that eliminates the need for a foreign electrode, conducting layers provide microwave loss due to Eddy currents, and are therefore, precluded from use as microwave passive components. However, the effect goes to the heart of electrical tunability which is why the subject matter is discussed

briefly. The ME effect in manganite/PZT heterostructures was observed by Srinivasan *et al.*<sup>17</sup> who laminated and sintered the films prepared by tapecasting to obtain the heterostructure samples. Two types of heterostructures were investigated: LSMO-PZT and LCMO-PZT. Figure 3 shows the  $H$  dependence of the transverse ME voltage coefficient  $\alpha_{E,zx}$  for a LSMO-PZT bilayer at temperatures 120 and 300 K measured using an AC magnetic field frequency of 100 Hz. Hysteretic behavior is evident at both temperatures. At 120 K, while increasing  $H$  from -500 Oe to 500 Oe  $\alpha_{E,zx}$  reaches a peak value of -40 mV/cm-Oe at  $H = -35$  Oe. With further increase in  $H$ , the magnitude of  $\alpha_{E,zx}$  is reduced and a phase shift occurs in the ME voltage at the coercive field of  $H_c = 35$  Oe.  $\alpha_{E,zx}$  again reaches a peak value of 40 mV/cm-Oe at 140 Oe and gradually decreases to zero with further increase in  $H$ . The decrease in  $\alpha_{E,zx}$  with increasing  $H$  at high bias fields for both polarities is due to saturation of the magnetostriction of the LSMO layer. A similar behavior is observed for decreasing  $H$ , from 500 to -500 Oe, but the positive peak position is downshifted in  $H$ , and  $\alpha_{E,zx}$  reaches a higher value of 60 mV/cm-Oe. When the sample temperature is increased to 300 K the hysteresis has similar shape, but with a smaller  $H_c$  and overall reduction in the ME magnitude  $\alpha_{E,zx}$ . The ME effect in LSMO-PZT samples was observed to be larger by a factor 5 than that in LCMO-PZT. The longitudinal ME coefficients were observed to be independent of the temperature, while the transverse coefficient showed a 50% drop over the temperature range 200–300 K. This was attributed to the temperature dependence of material parameters, in particular, the magnetostriction. Additionally, both transverse and longitudinal components of  $\alpha_E$  decreased linearly with increasing total number of layers in the multilayer heterostructure. A reduction by a factor of 3 was observed when the total number of layers was increased

form 2 to 8. Such a large decrease in the ME parameters could only be due to degradation of the material parameters due to diffusion of metal ions across the piezoelectric-magnetostrictive interface.

Srinivasan *et al.*<sup>57</sup> reported a giant ME effect that results from stress-mediated electromagnetic coupling in bilayers and multilayers of nickel ferrite and lead zirconate titanate. Samples with layer thickness 10–200  $\mu\text{m}$  were synthesized by doctor-blade techniques, and then laminated and sintered to form multilayer structures. The magnetoelectric voltage coefficient  $\alpha_E$  ranged from 460 mV/cm-Oe in bilayers to 1500 mV/cm-Oe for multilayers. The transverse effect was an order of magnitude stronger than longitudinal one. The ME coefficient was maximum at room temperature and a general increase in  $\alpha_E$  was observed with increasing frequency. Data on the dependence of  $\alpha_E$  on volume fraction of the two phases and bias magnetic field are in excellent agreement with a theoretical model for a perfectly bonded bilayer.

***Single crystal ferrites bonded with single crystal or ceramic ferroelectrics:***

Even though the ferromagnetic resonance line broadening problem can be overcome by using layered structures such as laminated composites, the narrowest resonance linewidth is naturally possible in single crystal material. Therefore, using single crystal ferrites enhances the resolution in electric field tunability. Using ferroelectrics of single crystal form is also beneficial as they would produce higher strain, and therefore, a larger ME effect will result in ferroelectric/ferromagnetic bilayer structures. As single crystal YIG has been shown to exhibit the narrowest ferromagnetic resonance linewidth, most of the

efforts on ME coupling-based devices have focused on incorporating single crystal YIG with different types of ferroelectric layers, either in single crystal or ceramic form. The two constituents are generally bonded using epoxy to form the bilayer structures. In the case the change in the ferromagnetic resonance (FMR) frequency of the ferrite layer is monitored, the electric field is applied across the piezoelectric layer, where one of the electrodes is placed between the two constituents forming the bilayer. To avoid microwave losses in the piezoelectric stressor, generally a metal layer that is several skin depths thick (e.g. skin depth for Ag is  $0.64\ \mu\text{m}$  at 10 GHz) is used in between to confine the microwave radiation in the ferrite layer during FMR measurements. However, the presence of such a thick metal layer at the bonding interface reduces the mechanical coupling, i.e. the efficiency of strain transfer. Therefore, the thickness of the electrode as well as the bonding material and the measurement configuration should be optimized to achieve higher mechanical coupling.

An electric field-tunable yttrium iron garnet (YIG)-lead zirconate titanate (PZT) microwave resonator based on ferromagnetic resonance for YIG has been demonstrated.<sup>77</sup>

The schematics of the YIG-PZT bilayer resonator are shown in Figure 4. A  $15\ \mu\text{m}$ -thick liquid phase epitaxy grown YIG film on a (111) GGG substrate having lateral dimensions  $1\ \text{mm} \times 2.2\ \text{mm}$  was bonded to a ceramic PZT plate ( $4\ \text{mm} \times 4\ \text{mm} \times 0.5\ \text{mm}$ ) coated with  $5\ \mu\text{m}$ -thick silver electrodes on both sides, using fast-dry epoxy. The YIG film had a saturation magnetization of 1750 G and a FMR linewidth of  $\sim 0.6\ \text{Oe}$  at 5 GHz. The bilayer was placed on a microstrip transducer ( $50\ \mu\text{m} \times 3\ \text{mm}$ ) fabricated on an alumina substrate from the GGG substrate side as shown in Figure 4. For an electric field of  $\pm 10$



kV/cm applied across the PZT plate, the FMR peak shifted by up to 18 MHz and 25 MHz for a magnetic field bias parallel and perpendicular, respectively, to the bilayer plane [see **Figure 5**], an order of magnitude higher than the absorption width of the resonator (3.4 MHz at 3dB). The FMR frequencies for in plane ( $\omega_1$ ) and out-of-plane ( $\omega_2$ ) applied magnetic fields are given in cgs units by

$$\omega_1 = \gamma \left[ H_0 (H_0 + 4\pi M_s) \right]^{1/2} \quad \text{and} \quad \omega_2 = \gamma (H_0 - 4\pi M_s)$$

**Equation 32**

The finite lateral dimensions of the ferrite film, metallization on the ferroelectric surfaces, and the anisotropy fields in the ferrite may result in slight deviations from the theoretical estimates; however, FMR frequencies obtained from **Equation 32** were shown to be in good agreement with measurements. **Figure 5(b)** shows the dependence of the frequency shifts  $\delta f_1$  and  $\delta f_2$  as functions of  $E$  measured at a central frequency  $f = 5$  GHz, corresponding to an in-plane  $H = 1.07$  kOe or out-of-plane  $H = 3.53$  kOe magnetic field. The average shift is in the range of 1.8–2.5 MHz for  $E = 1$  kV/cm, depending on the orientation of  $H$ . The corresponding ME coefficients extracted from magnetostriction induced magnetic field shifts are  $\alpha_{f,1} = \delta H_1 / \delta E \approx 0.58$  Oe-cm/kV and  $\alpha_{f,2} = \delta H_2 / \delta E \approx 0.88$  Oe-cm/kV, for magnetic bias field applied parallel and perpendicular to the sample plane, respectively, which are larger than 0.1-0.33 Oe-cm/kV estimated<sup>101</sup> and measured<sup>102</sup> for similar YIG-PZT bilayers. The frequency shift, which arises due to magnetoelectric interactions, is relatively large for out-of-plane  $H$  in accordance with the theory.<sup>103,104</sup> From the analysis of data it was concluded that the primary cause of the frequency shift was variation of the effective internal magnetic field in YIG with applied electric field. In the case of PZT integrated with  $\text{Li}_{0.5}\text{Fe}_{2.5}\text{O}_4$  (lithium ferrite or LFO), a

much smaller ME coupling coefficient of  $\alpha_f = 0.25$  Oe-cm/kV has been reported for multilayer structures containing 16 layers of LFO and 15 layers of PZT, with each layer thickness being 15  $\mu\text{m}$ .<sup>105</sup>

The extent of frequency tuning could potentially be increased by decreasing the thickness of the GGG substrate and/or using a stronger piezoelectric than PZT, such as single crystal PMN-PT.<sup>76,104</sup> Bilayers incorporating 0.5 mm-thick single crystal (001) PMN-PT bonded using epoxy to 1 to 110  $\mu\text{m}$ -thick (111) YIG films on GGG substrates have been investigated.<sup>76</sup> Upon increasing the YIG thickness from 4.9  $\mu\text{m}$  to 110  $\mu\text{m}$  the ME constant for the out-of-plane H-field reduced from 5.4 Oe-cm/kV to 2.3 Oe-cm/kV. For  $H$  parallel to the YIG plane the magnitude of the shift in the resonance field,  $\delta H_E$ , and the coupling constant  $\alpha$ , were smaller compared to those for the out-of-plane  $H$ -field. For example, for 110  $\mu\text{m}$ -thick YIG  $\alpha_f$  decreased from 2.3 Oe-cm/kV for the out-of-plane  $H$  to 1 Oe-cm/kV for the in-plane  $H$  (Figure 6).

As discussed in Section 3.4 in Part 1,<sup>[1]</sup> hexaferrites have high uniaxial anisotropy fields,  $H_a$ , and high saturation magnetization,  $4\pi M_s$ . M-type barium hexaferrite  $\text{BaFe}_{12}\text{O}_{19}$  (BaM) with  $H_a = 17$  kOe and saturation magnetization  $4\pi M_s = 4.8$  kG is appropriate for studies of millimeter-wave ME interactions. Using Equation 72 in Part 1 [1] the corresponding FMR frequency can be calculated to be in a frequency range of 47-60 GHz for external fields of  $H_0 = 5$ -9 kOe applied along the  $c$ -axis (perpendicular to the surface) of a BaM slab. When a piezoelectric layer is used to deform the ferrite and the ME effects are taken into account, the FMR frequency is given by

$$f_r = \frac{\gamma}{2\pi} (H_0 + H_a - 4\pi M_s + \alpha_f \cdot E) = \frac{g\mu_B}{2\pi\hbar} (H_0 + H_a - 4\pi M_s + \alpha_f \cdot E) \\ \cong (2.8 \text{ MHz/Oe}) (H_0 + H_a - 4\pi M_s + \alpha_f \cdot E)$$

**Equation 33**

where  $\alpha_f = \delta H / \delta E$  is the ME coupling constant. The electric field induced shift in the resonance frequency is, therefore,  $\delta f_r = (\gamma / 2\pi) \alpha_f \delta E$ , which has been measured in BaM-PZT bilayers.<sup>106</sup>

In one particular investigation,<sup>106</sup> the bilayer was prepared by bonding BaM single crystal plates prepared by floating zone method to polycrystalline PZT plates having thin layers of silver electrodes on both surfaces using fast dry epoxy. Using a measurement cell that consisted of a coaxial-to-waveguide adaptor the reflected power as a function of the frequency was measured at different electric fields applied across the PZT stressor. As shown in **Figure 7(a)** as the electric field  $E$  is increased from 0 to 8 kV/cm the frequency upshifts by 4 MHz, which is significantly higher than the 3dB linewidth of 1 MHz, and absorption increases by 10–20 dB. **Figure 7(b)** shows the electric field dependence of the frequency shift ( $\delta f_r$ ) measured for a bilayer with 95  $\mu\text{m}$ -thick BaM, which exhibits hysteretic behavior resulting from the piezoelectric deformation in PZT. A maximum shift of 8 MHz is observed at +10 kV/cm, corresponding to an ME coupling constant of  $\delta f_r / \delta E = \alpha_f (\gamma / 2\pi) = 0.8 \text{ MHz-cm/kV}$ . This is lower than the calculated coefficient of 22 MHz-cm/kV [Ref. 106] most probably due to imperfect mechanical coupling. The measured coefficient ( $\delta f_r / \delta E$ ) is also slightly lower than those obtained for

YIG/PMN-PT bilayers (3-15 MHz-cm/kV) and YIG<sub>0.95</sub>-PZT<sub>0.05</sub> bulk composites (1 MHz-cm/kV).<sup>76</sup>

More results on bonded single crystal ferrite-ferroelectric bilayer structures will be discussed in [Section 3.6](#). These structures have been used for electrically tunable microwave resonators, phase shifters, delay lines, and filters.

#### ***Epitaxially grown bilayers:***

The bonding requirement for the ferroelectric and ferromagnetic (or ferrimagnetic) constituents to enhance ME coupling is lifted in epitaxial layers, meaning epitaxial growth of the stressor and the ferrite material on each other. In fact, epitaxial growth results in the best mechanical coupling, and therefore, the largest ME effect between the two constituents if they can be epitaxially grown on one another. However, the lattice mismatch and incompatible crystal structure related problems, which in many cases may prove to be intractable, remain. This naturally limits the choice of materials for ME coupling-based device applications, and is the reason why experimental reports on epitaxially-grown multilayer structures have been very limited. Additionally, in the case of ferrites, which are usually nonconductive, the need for a metal layer in between the two types of materials as an electrical contact to the ferroelectric layer complicates the epitaxial growth further. Therefore, almost all the ME coupling investigations in epitaxially grown bilayers involve conductive and ferromagnetic manganites such as La<sub>0.7</sub>Sr<sub>0.3</sub>MnO<sub>3</sub> (LSMO).

A remarkable ME effect was observed by Wu *et al.*<sup>56</sup> in an epitaxial multiferroic heterostructure which was constructed by depositing a piezoelectric  $\text{PbZr}_{0.3}\text{Ti}_{0.7}\text{O}_3$  film (110 nm) by the sol-gel method on a magnetostrictive layered manganite, melt-grown single crystal  $\text{La}_{1.2}\text{Sr}_{1.8}\text{Mn}_2\text{O}_7$ . The ME voltage, which had strong temperature dependence, was very close to the theoretical value (~87% of value predicted by theory).

**Figure 8** shows the static magnetic field dependence of the induced ME voltage at three temperatures, 50, 120, and 300 K, measured using an AC magnetic field with a magnitude of  $H = 2$  Oe and a frequency of  $f = 1$  kHz. The strongest ME effect is at 120 K, near the ferromagnetic transition temperature ( $T_C$ ) of the manganite crystal, wherein as  $H_0$  is increased  $V_{ME}$  first increases, then peaks at ~1 T with a magnitude of  $\Delta V_{ME} \sim 15$   $\mu\text{V}$ , and finally decreases at higher fields. As  $H_0$  decreases,  $V_{ME}$  goes through zero and switches its direction (changing its sign). At 120 K, the peak-to-peak difference of the ME voltage swing is  $\sim 2\Delta V_{ME}$  or 28  $\mu\text{V}$ . This ME effect is much weaker at 50 K and room temperature, away from  $T_C$ . This strong temperature dependence is supposed to result from magnetostrictive properties of the manganite crystal. As the temperature approaches  $T_C$ , magnetostriction along both the  $ab$  plane and the  $c$  axis increase in accordance with the enhancement of the magnetoresistance effect. At 120 K, the in-plane lattice contraction  $\Delta L_{ab} / L_{ab}(0)$ , reaches a value of  $4.4 \times 10^{-4}$  under a magnetic field of 7 T, which is comparable to that of Terfenol-D ( $\text{TbDyFe}_2$  alloy), the best magnetostrictive materials. However, at lower fields the magnetostriction of the manganite crystal is much smaller being only  $100 \times 10^{-6}$  under 5 kOe that is about two orders of magnitude smaller than that for Terfenol-D for the same field. The temperature dependence of the

magnetostriction without magnetic field also shows a contraction of the in-plane lattice plane of  $\sim 0.1\%$  at  $T_C$ , showing the structural instability at this temperature.

Magnetostrictive layers have also been grown epitaxially on single crystal piezoelectric layers. In a particular study it was shown that<sup>107</sup> the resistance of thin ( $\sim 35$  nm)  $c$ -axis oriented  $\text{La}_{0.85}\text{Sr}_{0.15}\text{MnO}_3$  (LSMO) films grown by DC magnetron sputtering on single crystal (001)  $0.7\text{Pb}(\text{Mg}_{1/3}\text{Nb}_{2/3})\text{O}_3$ - $0.3\text{PbTiO}_3$  (PMN-PT) substrates could be modulated by applying an electric field across the PMN-PT substrate. LSMO exhibited a phase transition from paramagnetic state to ferromagnetic state when the temperature was decreased below the Curie temperature, which was taken to be the insulator-metal transition temperature ( $\sim 120$  °C). With further reduction of the temperature, another phase transition to the charge-ordered state was observed (transition temperature  $\sim 50$  °C). The maximum resistance modulation ( $\Delta R/R$ ) observed was 0.5 % at 296 K (paramagnetic state) and 3 % at 77 K (ferromagnetic state) for an applied field of 2 kV/cm. The increasing (decreasing) resistance of the thin LSMO layer was indicative of increasing (decreasing) in-plane tensile strain. This indicates that the magnetization of the LSMO films can be modified by applying an electric field to the PMN-PTO stressor; however, no measurements on the magnetic properties were reported in this particular study.

The piezoelectric and ferromagnetic layers can both also be grown epitaxially on a non-native substrate. For example, the ME effect was studied on epitaxial (001)  $\text{Pb}(\text{Zr}_{0.52}\text{Ti}_{0.48})\text{O}_3$  (430 nm) /  $\text{La}_{0.7}\text{Sr}_{0.3}\text{MnO}_3$  (330 nm) bilayers grown by pulsed laser deposition on (001)  $\text{LaAlO}_3$  substrates.<sup>108</sup> The ME voltage coefficient  $\alpha_E = \delta V / t \delta H$ ,

where  $t$  is the PZT layer thickness, was measured with the bias DC magnetic field perpendicular (transverse) and parallel to the AC magnetic field  $\delta H$  applied along the normal [001] direction. For transverse and parallel configurations, the maximum ME coefficients obtained were 3.0 and 4.2 mV/cm-Oe, respectively. In thin epitaxial bilayers, since the substrate is much thicker than the epitaxial layers, any free deformation of the bilayer is prevented due to “substrate clamping”, as also will be discussed in [Section 2.2.4](#). The observation of the ME effect in PZT/LSMO epitaxial bilayers was thought to be made possible by weakening of this clamping effect due to the columnar structure of the magnetostrictive LSMO layer, which resulted from the large amount of void grain boundaries. This columnar structure was suggested to result in free deformation of the upper parts of the LSMO layer with electric field applied to the PZT layer grown on top. However, the ME coefficients are still almost an order of magnitude smaller than those obtained in tape-cast thick PZT/LSMO laminates ( $\alpha_E = 30$  and 14 mV/cm-Oe for transverse and parallel modes, respectively, at room temperature).<sup>17</sup> This difference was attributed to the strong substrate clamping, which was still present for the thin film structures, even though its effect was somewhat weakened due to the columnar structure.

To modify the magnetic properties of the ferromagnetic phase in ferromagnetic/piezoelectric bilayers, the biaxial strains induced by the phase transitions in piezoelectric layers have also been utilized.<sup>109</sup> For instance, BaTiO<sub>3</sub> goes through three distinct phase transitions with decreasing temperature: from cubic to tetragonal structure at 393 K, to monoclinic structure at 278 K, and to rhombohedral structure at 183 K. During the tetrahedral-monoclinic transition (001) oriented BaTiO<sub>3</sub> substrate undergoes a

21 % expansion and 0.21 % distortion in in-plane lattice strains  $\varepsilon_a = (\varepsilon_{xx} + \varepsilon_{yy})/2$  and  $\varepsilon^* = (\varepsilon_{xx} - \varepsilon_{yy})/2$ , respectively. The transition to rhombohedral structure results in 0.10 % expansion in  $\varepsilon_a$  and -0.43 distortion in  $\varepsilon^*$ . The  $\text{La}_{0.67}\text{Sr}_{0.33}\text{MnO}_3$  epitaxial films (50 nm) sputtered on (001)  $\text{BaTiO}_3$  substrates, therefore, exhibit large changes in the magnetization at the ferroelectric phase transition temperatures as shown in **Figure 9**. When a magnetic field of 20 Oe was applied along the [100] direction, the magnetization was observed to change by 10 % and 70 % at 183 and 278 K, respectively, with increasing temperature, as shown in **Figure 10**. The magnetization loop measured above the tetragonal to monoclinic transition temperature exhibited nearly zero remanence and high saturation magnetization indicating hard axis, while it was nearly square with well defined coercivity ( $\sim 70$  Oe) and smaller saturation magnetization below the transition temperature consistent with behavior along the easy axis. This indicates that magnetic anisotropy reversal in LSMO takes place due to in-plane lattice distortions.

Thin film structures composed of BaM and  $\text{BaSrTiO}_3$  (BST) bilayers have also been produced using epitaxial methods for dual tunable (electric and magnetic tunability) devices.<sup>110</sup> A BaM layer of 0.5  $\mu\text{m}$  nominal thickness was grown epitaxially on *c*-sapphire by PLD. A BST layer of 0.9  $\mu\text{m}$ -thickness was then grown on the BaM layer also by PLD after sputter deposition of a 30 nm-thick Au electrode. Finally, a 50 nm-thick Au electrode was sputtered on top of BST. XRD analysis of the overall structure showed that the BaM layer was epitaxial while the BST layer was polycrystalline. Magnetization and FMR measurements performed on the bilayer structure with electrodes showed a uniaxial anisotropy field of 16 kOe and an FMR linewidth of 25 Oe



at 60 GHz (at  $H = 9.4$  kOe) for the BaM constituent. This indicates that a low FMR loss BaM layer can be achieved even in a layered structure including thin gold electrode and BST layers present. The FMR linewidth is comparable to the intrinsic linewidths in bulk BaM single crystals (see discussion in [Section 4.7](#) in [Part 1](#))[1] Furthermore, the dielectric constant of BST could be tuned between 13 and 27 showing a cusp response with electric field applied between the Au electrodes. These low dielectric constants were attributed to gold diffusion into the BST layer as the dielectric constant for conventional 100 nm-thick BST layers is expected to be  $\sim 1200$ . It was suggested that using Pt electrodes might prevent this diffusion-related degradation of BST.

### 2.2.3. Resonance effects

The ME coupling in magnetostrictive-piezoelectric two-phase systems has been demonstrated using mostly low frequency (10 Hz to 10 kHz) modulation of the magnetic or the electric field. The studies on the frequency dependence of the ME effect, however, have shown that the ME coupling is affected by the mechanical and magnetic resonances of the respective subsystems. In the vicinity of the electromechanical resonance of the piezoelectric component or the ferromagnetic resonance of the magnetostrictive component, the ME effects are significantly enhanced. The electromechanical resonance can even be adjusted to coincide with the ferromagnetic resonance, by decreasing the size, particularly the thickness, of the piezoelectric constituent, resulting in magnetoacoustic resonances.

To study the resonance effects, typically the ME response is first measured at a given AC magnetic field frequency as a function of the static magnetic field to determine the static field corresponding to the peak response. The static field is then set to this value and the frequency of the AC magnetic field frequency is swept to observe the resonance behavior.

**Figure 10** shows the frequency response of the longitudinal ME voltage coefficient measured for a 10 mm diameter multilayer sample consisting of 11 layers of 13  $\mu\text{m}$ -thick  $\text{NiFe}_2\text{O}_4$  and 10 layers of 26  $\mu\text{m}$ -thick PZT disks.<sup>70</sup> The resonance value of  $\alpha_E$  at  $f_r = 350$  kHz is more than 40 times higher than the low frequency values. The frequency dependence of the dielectric constant of a single 10 mm-diameter PZT disk shows a resonance (discontinuity) close to the peak position of  $\alpha_E$ , indicating that the enhancement in  $\alpha_E$  is due to electromechanical coupling.

The theoretical analysis of the resonance ME effects may be performed for multilayers in the form of thin disks or thin plates, where the thickness is small compared to the wavelengths of the acoustic modes. The thickness is also assumed to be much smaller than the lateral dimensions of the multilayer (radius,  $R$ , in the case of disks) so that only the radial modes are considered. The outer surfaces of the multilayer system are coated with metallic contacts, and are equipotential; therefore, only the normal component of the electric field is nonzero. Moreover, for thin layers the normal component of the stress tensor may be taken as zero in the entire volume. In the case of longitudinal fields (AC and DC magnetic fields and the electric field are all along the surface normal), if the coordinate system is defined to be similar to that in **Figure 2** (with 1, 2, and 3 corresponding to  $x$ ,  $y$ , and  $z$ , respectively), where the surface normal is along the  $z$ -

direction, using Equation 25 the nonzero components of the strain tensor components in cylindrical coordinates can be obtained as

$$S_{rr} = \frac{\partial u_r}{\partial r} = s_{11}T_{rr} + s_{12}T_{\theta\theta} + d_{31}E_z + q_{31}H_z$$

$$S_{\theta\theta} = \frac{1}{r} \left( \frac{\partial u_\theta}{\partial \theta} + u_r \right) = s_{12}T_{rr} + s_{11}T_{\theta\theta} + d_{31}E_z + q_{31}H_z$$

**Equation 34**

where  $\mathbf{u}$  is the medium displacement vector and  $T_{rr}$  and  $T_{\theta\theta}$  are the nonzero components of the stress tensor. Due to the axial symmetry, the displacement component  $u_\theta$  is zero. For composite and multilayer systems, effective values of all the coefficients are used for the overall system.<sup>111</sup> The equation of motion for the radial propagating modes can be written as

$$\frac{\partial}{\partial r} T_{rr} + \frac{1}{r} (T_{rr} - T_{\theta\theta}) + \rho \omega^2 u_r = 0$$

**Equation 35**

where  $\rho$  is the mass density and  $\omega$  is the angular frequency. Expressing the stress components in terms of the strain using Equation 34 and substituting them in Equation 35, the  $u_r$  term is found to be a linear combination of the first and second order Bessel functions where the coefficients are determined from the boundary conditions:  $u_r = 0$  at  $r = 0$  and  $T_{rr} = 0$  at  $r = R$ . Using these boundary conditions leads to<sup>111</sup>

$$T_{rr} = \frac{1}{s_{11}(1-\nu)} \left[ \frac{kR J_0(kr) - (1-\nu) \frac{R}{r} J_1(kr)}{kR J_0(kR) - (1-\nu) J_1(kR)} - 1 \right] (q_{31}H_z + d_{31}E_z)$$

$$T_{\theta\theta} = \frac{1}{s_{11}(1-\nu)} \left[ \frac{\nu k R J_0(kr) + (1-\nu) \frac{R}{r} J_1(kr)}{k R J_0(kR) - (1-\nu) J_1(kR)} - 1 \right] (q_{31} H_z + d_{31} E_z)$$

**Equation 36**

where  $\nu = -s_{12} / s_{11}$  is the Poisson's ratio and  $k = \omega \sqrt{\rho s_{11} (1-\nu^2)}$ .

Since the top and the bottom surfaces are coated with thin metal layers, and therefore are equipotential, the only nonzero component of the electric displacement is

$$D_z = d_{31} (T_{rr} + T_{\theta\theta}) + \varepsilon_{33} E_z + \alpha_{33} H_z$$

**Equation 37**

where  $\varepsilon_{33}$  is the dielectric constant and  $\alpha_{33}$  is the ME coefficient. Using open circuit conditions and **Equation 36**, the electric field can be found as

$$E_z = -\frac{1}{\Delta_a} \left[ \frac{2d_{31}q_{31}}{\varepsilon_{33}s_{11}(1-\nu)} \left( \frac{(1+\nu)J_1(kR)}{\Delta_r} - 1 \right) + \frac{\alpha_{33}}{\varepsilon_{33}} \right] H_z$$

**Equation 38**

where  $\Delta_r = k R J_0(kR) - (1-\nu) J_1(kR)$  and  $\Delta_a = 1 - K_p^2 + K_p^2 (1+\nu) J_1(kR) / \Delta_r$ . Here,  $K_p$

represents the electromechanical coupling coefficient for the radial modes

$$K_p^2 = \frac{2d_{31}^2}{\varepsilon_{33}s_{11}(1-\nu)}$$

**Equation 39**

The longitudinal ME voltage coefficient can then be obtained as:<sup>111</sup>

$$(\alpha_E)_L = \frac{\delta E_z}{\delta H_z} = \frac{1}{\Delta_a} \left[ \frac{2d_{31}q_{31}}{\varepsilon_{33}s_{11}(1-\nu)} \left( 1 - \frac{(1+\nu)J_1(kR)}{\Delta_r} \right) - \frac{\alpha_{33}}{\varepsilon_{33}} \right]$$

**Equation 40**

At low frequencies, the first term in the square brackets is negligible and the ME coefficient reduces to its low frequency value of  $\alpha_{33}/\epsilon_{33}$ . The roots of  $\Delta_r$  define the resonance frequencies, and the roots of  $\Delta_a$  give the antiresonances corresponding to the piezoelectric effect. Under open circuit conditions, the ME coefficient rises rapidly near the antiresonance frequencies, where the first term in Equation 40 dominates. In reality, the losses control the resonance linewidth and limit the ME coefficient. The losses can be included in Equation 40 by using a complex quantity either for  $\omega$  or  $k$ , where a damping coefficient  $\xi$  defines the complex part (such as  $\omega = \omega' + i\xi$ ).<sup>111</sup> Damping may also be taken into account by introducing a loss factor as an imaginary component into  $\Delta_a$ .<sup>70</sup>

Similarly, in the case of transverse fields (AC and DC magnetic fields are in the sample plane, chosen to be along the  $x$ -direction here, and the electric field is along the surface normal), the strain components can be written in cylindrical coordinates as

$$S_{rr} = \frac{\partial u_r}{\partial r} = s_{11}T_{rr} + s_{12}T_{\theta\theta} + d_{31}E_z + (q_{11}\cos^2\theta + q_{12}\sin^2\theta)H_x$$

$$S_{\theta\theta} = \frac{1}{r}\left(\frac{\partial u_\theta}{\partial \theta} + u_r\right) = s_{12}T_{rr} + s_{11}T_{\theta\theta} + d_{31}E_z + (q_{11}\sin^2\theta + q_{12}\cos^2\theta)H_x$$

**Equation 41**

In the transverse case, the strain components have angular dependence in addition to the radial dependence since the magnetic field breaks the axial symmetry. Using a similar approach as taken before for the longitudinal case, the transverse ME voltage coefficient can be obtained as:<sup>111</sup>

$$(\alpha_E)_T = \frac{\delta E_z}{\delta H_x} = \frac{1}{\Delta_a} \left[ \frac{d_{31}(q_{11} + q_{12})}{\varepsilon_{33}s_{11}(1-\nu)} \left( 1 - \frac{(1+\nu)J_1(kR)}{\Delta_r} \right) - \frac{\alpha_{31}}{\varepsilon_{33}} \right]$$

Equation 42

It is evident from Equation 40 and Equation 42 that the ME coefficient is proportional to the product of the effective piezoelectric and the piezomagnetic moduli. Due to the absence of demagnetization for the transverse orientation, the piezomagnetic coefficients  $q_{11}$  and  $q_{12}$  are significantly larger than  $q_{31}$ . Therefore, the transverse ME coefficient at the resonance is expected to be larger than the longitudinal ME coefficient. The frequency dependences of the longitudinal and transverse ME coefficients are identical, as the same radial modes are excited in both orientations. Experimental results on multilayer structures consisting of 10 layers of 26  $\mu\text{m}$ -thick ceramic PZT and 11 layers of 13  $\mu\text{m}$ -thick spinel  $\text{NiFe}_2\text{O}_4$  disks have shown 10 fold stronger ME coefficients at the resonance for the transverse mode ( $\sim 15 \text{ V/cm-Oe}$ ).<sup>111</sup> The resonance was observed near 350 kHz, and the ME coefficients measured at 100 Hz, was much smaller, 0.16 V/cm-Oe.

The theory of the resonance ME effect may also be considered for plate-like bilayer samples instead of disks.<sup>112</sup> The vibrations induced in the ferromagnet (or ferrimagnet) by the AC magnetic field due to magnetostriction may propagate both along the sample normal and in the contact plane. The vibrational modes along the surface normal have higher frequencies as will be discussed later, and the analysis below is restricted to the modes in the contact plane, which have the lowest frequencies. The approach taken is similar to that described for the disk-shaped samples using cylindrical coordinates. In the case of plate-like samples, the bilayer structure is assumed to have the coordinate system

shown in Figure 11. It is assumed that the total thickness ( ${}^m h + {}^p h$ ) and the width ( $W$ ) are much smaller than the length ( $L$ ). For such a thin and narrow plate, the stress components along  $y$  and  $z$  may be considered zero over the entire volume of the plates, and only the  $x$  component of the stress,  $T_x$ , remains. Also, the top and bottom surfaces are at equipotential; and therefore, only the  $z$ -component of the electric field ( $E_z$ ) is nonzero. For a free body, the stresses at the surfaces are also zero. The nonzero strain tensor components of the magnetostrictive and the piezoelectric layers for the transverse fields may be written as

$$\begin{aligned} {}^m S_x &= {}^m s_{11} {}^m T_x + {}^m q_{11} {}^m H_x \\ {}^p S_x &= {}^p s_{11} {}^p T_x + {}^p d_{31} E_z \end{aligned}$$

#### Equation 43

where superscripts  $m$  and  $p$  stand for the magnetostrictive and the piezoelectric phases, respectively. For the longitudinal fields,  ${}^m q_{31} {}^m H_z$  should be used instead of  ${}^m q_{11} {}^m H_x$ . After writing the stress components in terms of the strain components and substituting them into the equation of motion, the solution for the  $x$ -projection displacement vector of the magnetic medium have the form

$${}^m u_x(x) = A \cos({}^m kx) + B \sin({}^m kx)$$

#### Equation 44

where  $A$  and  $B$  are constants,  ${}^m k = \omega \left( {}^m \rho {}^m s_{11} \right)^{1/2}$ , and  ${}^m \rho$  is the mass density of the magnetostrictive component. The displacement of the piezoelectric medium can be written as a superposition of the displacement caused by the coupling to the

magnetostrictive component and the natural displacement due to the induced electric field as

$${}^p u_x(x) = \beta {}^m u_x(x) + (1 - \beta) {}^p u_x^{(0)}(x)$$

**Equation 45**

where  $\beta$  is a coefficient, between 0 and 1, representing the coupling between the two constituents, as the mechanical contact between the two phases is not ideal, and  ${}^p u_x^{(0)}(x)$  is the displacement in the absence of coupling

$${}^p u_x^{(0)}(x) = \frac{{}^p d_{31} E_z}{{}^p k \cos({}^p kL/2)} \sin({}^p kx)$$

**Equation 46**

where  ${}^p k = \omega({}^p \rho {}^p s_{11})^{1/2}$  and  ${}^p \rho$  is the mass density of the piezoelectric component. The faces of the sample along the x-axis are free; therefore, the resultant force acting on them is zero. Using these boundary conditions one obtains:<sup>112</sup>

$${}^p u_x(x) = \frac{\beta}{(\gamma + \beta)} \frac{\sin({}^m kx)}{{}^m k \cos({}^m kL/2)} (\gamma {}^m q_{11} H_x - \beta {}^p d_{31} E_z) + (1 - \beta) \frac{{}^p d_{31} E_z}{{}^p k \cos({}^p kL/2)} \sin({}^p kx)$$

**Equation 47**

where  $\gamma = ({}^p s_{11} / {}^m s_{11})({}^m h / {}^p h)$  is a dimensionless parameter.

The electric displacement in the piezoelectric component for the transverse fields is given by

$$D_z = {}^p \varepsilon_{33} E_z + {}^p d_{31} {}^p T_x$$

**Equation 48**



Using open circuit conditions, the electric field in the piezoelectric medium can be obtained as:

$$E_z = -\frac{\gamma\beta}{(\gamma + \beta)} \frac{{}^p d_{31} {}^m q_{11}}{{}^p \epsilon_{33} {}^p s_{11} \Delta_a} \frac{\tan({}^m kL/2)}{{}^m kL/2} H_x$$

**Equation 49**

where

$$\Delta_a = 1 - \left( 1 - (1 - \beta) \frac{\tan({}^p kL/2)}{{}^p kL/2} - \frac{\beta^2}{(\gamma + \beta)} \frac{\tan({}^m kL/2)}{{}^m kL/2} \right) \frac{{}^p d_{31}^2}{{}^p \epsilon_{33} {}^p s_{11}}$$

**Equation 50**

Assuming that the total voltage drop occurs across the piezoelectric and the electric field should be averaged over the total thickness of the bilayer the transverse ME voltage coefficient may be obtained as

$$(\alpha_E)_T = \frac{\delta E_{z,average}}{\delta H_x} = -\frac{\gamma\beta}{(\gamma + \beta)} \frac{{}^p d_{31} {}^m q_{11}}{{}^p \epsilon_{33} {}^p s_{11} \Delta_a} \frac{\tan({}^m kL/2)}{{}^m kL/2} \frac{{}^p h}{{}^p h + {}^m h}$$

**Equation 51**

In order to obtain the longitudinal ME voltage coefficient, simply  ${}^m q_{11}$  in Equation 51 should be replaced by  ${}^m q_{31}$ . Note that usually  ${}^m q_{31} < {}^m q_{11}$  due to demagnetization fields; therefore the transverse ME coefficient is significantly larger than the longitudinal one. The resonances again occur at the roots of  $\Delta_a$ . and the losses may be included by introducing a complex frequency  $\omega = \omega' + i\chi$ , with the damping parameter  $\chi$ .

When the coupling coefficient  $\beta$  is unity, the ME coefficient is increased significantly at the frequency corresponding to the resonance in the magnetostrictive phase. For  $\beta < 1$ ,

two sets of vibrations characterized by the wavevectors  $^mk$  and  $^pk$  occur, leading to a second peak in the frequency response of the ME coefficient. Figure 12 shows the calculated frequency response of the transverse ME voltage coefficient for a PZT-Permendur<sup>ii</sup> bilayer structure ( $^mh = ^ph = 0.36$  mm,  $L = 7.5$  mm,  $\chi = 20000$  rad/s), for two different values of  $\beta$  (0.4 and 1).<sup>112</sup> The largest resonance ME responses measured so far was for Permendur-PZT-Permendur (90 V/cm-Oe)<sup>79</sup> and Ni/PZT/Ni (90 V/cm-Oe)<sup>113</sup> trilayer samples.

In addition to the radial modes in the piezoelectric constituent, the vibrational modes along the surface normal, which are also referred to as the thickness modes, may also be utilized to enhance the ME effect. As mentioned earlier, the thickness modes have frequencies higher than the radial modes since the thickness of the system is much smaller than the lateral dimensions. Utilizing these thickness modes, the electromechanical resonance (EMR) of the piezoelectric component may be adjusted to coincide with the FMR of the magnetic component. In such a case, the resonance is referred to as the magnetoacoustic resonance.<sup>114</sup> After fixing the geometrical shape of the piezoelectric layer, which sets the EMR, the magnetic field can be adjusted to tune the FMR to the EMR, resulting in a resonant enhancement of the ME coupling as discussed above. The applied static magnetic field also results in a shift in the EMR frequency due to changes in the Young's modulus.<sup>114,115</sup> At the coincidence of FMR and EMR, the coupling between the spins and the lattice, *i.e.* the energy transfer between the phonons, spin waves, and electrical and magnetic fields is expected to enhance the ME interactions.

---

<sup>ii</sup> An alloy formed by mixing 48-50% cobalt with iron (and up to 2% vanadium may be added). The alloy was discovered in the United States around 1920. It has a high permeability at high flux densities with a very high saturation point with a magnetic transition temperature is 980 °C.

By considering a ferrite-PZT bilayer, Bichurin *et al.*<sup>114</sup> have derived expressions for the ME voltage coefficient at microwave frequencies. The bilayer, which has ferrite and piezoelectric thicknesses of  $^mh$  and  $^ph$ , respectively, is subjected to a bias field  $\mathbf{H}_0$  perpendicular to the sample plane and the polling electric field  $\mathbf{E}_0$  is assumed to be parallel to  $\mathbf{H}_0$ . As discussed before, the AC magnetic field should be applied perpendicular to the DC magnetic field  $\mathbf{H}_0$  to observe the FMR, which induces an electric field in the plane of the PZT layer. Using a free energy composed of the Zeeman, anisotropy, magnetoelastic, and elastic energy components and writing out the equations of motion of displacements and magnetization, the ME voltage coefficient under open circuit conditions has been obtained.<sup>114</sup> The theory was tested for NiFe<sub>2</sub>O<sub>4</sub>-PZT and YIG-PZT bilayer systems. The FMR occurs at frequencies around 3-5 GHz for NiFe<sub>2</sub>O<sub>4</sub> and YIG, where a magnetically saturated state can be realized in the ferrite. For the EMR to coincide with the FMR, the thickness modes should be considered and the thicknesses of the layers should be chosen accordingly. Even if the lateral dimensions would allow such large EMR frequencies, the radial modes do not couple to FMR due to field polarization considerations.<sup>114</sup> For static magnetic field magnitudes smaller than that required for FMR,  $H^{FMR} = \omega/\gamma - 4\pi M_s$ , the ME voltage was found to show resonances at the fundamental and the second harmonic of the EMR for both of the systems investigated. When FMR was chosen to coincide with either the fundamental or the second harmonic of the EMR by adjusting the magnetic field magnitude, more than 40-fold and 80-fold increases in the ME coefficients were anticipated for NiFe<sub>2</sub>O<sub>4</sub>-PZT (480 V/cm-Oe) and YIG-PZT (170 V/cm-Oe) systems, respectively. The ME coefficients at the

magnetoacoustic resonance are higher in  $\text{NiFe}_2\text{O}_4$ -PZT due to strong magnetoelastic interaction in  $\text{NiFe}_2\text{O}_4$ . The layer thicknesses and the bias magnetic field magnitudes determine the EMR and FMR conditions, respectively, for a given set of materials. By choosing a higher order EMR, the FMR at a higher frequency can be fulfilled. Also by reducing the layer thicknesses the EMR can be tuned to higher frequencies. The fundamental EMR frequencies are around 5 GHz for both of the systems when 200 nm-thick PZT and 100 nm-thick  $\text{NiFe}_2\text{O}_4$  or YIG layers were considered. The EMR frequencies would double for the same systems having half these thickness values.

#### 2.2.4. Nanostructures

As discussed before, the ME effect is very sensitive to the mechanical coupling between the piezoelectric and the magnetostrictive components. Heteroepitaxial growth is the most effective way of integrating these two phases for the best mechanical coupling through the interface assuming that the lattice mismatch between the two phases can be managed and the crystal structures are compatible. In a film-on-substrate geometry, where the two phases are grown on a common substrate, the ME effect is limited due to the substrate clamping assuming that the ME coupling is purely through elastic interactions. The substrate clamping can be eliminated if the thin film bilayers can be formed into suspended membranes. In fact, finite element analysis has shown that an order of magnitude larger and more uniformly distributed strain can be induced in the suspended (unclamped) bilayer membranes compared to the clamped structures for a constant electric field applied across the piezoelectric phase.<sup>116</sup> To enhance the ME coupling, the interface area between the piezoelectric and the magnetostrictive phases

may also be increased by patterning the surface of one of the phases before the growth of the other. Alternatively, self assembled ME nanostructures may be formed, such as spinel  $\text{CoFe}_2\text{O}_4$  nanopillars embedded in a perovskite  $\text{BaTiO}_3$  matrix as demonstrated by Zheng *et al.*<sup>117</sup> The good interfacial bonding between the ferromagnetic and ferroelectric phases in the nanostructured films could significantly enhance the ME coupling. The (001)-oriented  $\text{CoFe}_2\text{O}_4$ - $\text{BaTiO}_3$  composites were grown by pulsed laser deposition on  $\text{SrRuO}_3$  electrodes deposited on  $\text{SrTiO}_3$  substrates. As shown in Figure 13(a), the  $\text{CoFe}_2\text{O}_4$  nanopillars were 20-30 nm in diameter with an average spacing equal to the diameter. Superconducting quantum interference device (SQUID) magnetometer measurements showed a saturation magnetization ( $M_s$ ) of  $\sim 350 \text{ emu/cm}^3$  and a strong anisotropy field between the out-of-plane [001] and in-plane [100] directions, which was derived to be  $\sim 35 \text{ kOe}$ . Near the ferroelectric Curie temperature of  $\text{BaTiO}_3$  ( $T_c \sim 390 \text{ K}$ ) a distinct drop was observed in the magnetization as shown in Figure 13(b), which manifests ME coupling. The lattice mismatch-induced compression in  $\text{CoFe}_2\text{O}_4$  is reduced below  $T_c$  due to the tetragonal distortion in  $\text{BaTiO}_3$ , and the magnetization is reduced as the magnetostriction in  $\text{CoFe}_2\text{O}_4$  is negative. The magnetization change observed for a control sample, a multilayered laminated nanostructure, was negligible. Electric field induced reversal of the magnetization was later observed at room temperature for  $\text{CoFe}_2\text{O}_4$  columnar structures embedded in a  $\text{BiFeO}_3$  matrix grown by pulsed laser deposition in a similar fashion on  $\text{SrTiO}_3$  substrates with  $\text{SrRuO}_3$  bottom electrodes.<sup>118</sup> A longitudinal magnetic ME coefficient of  $\alpha_M = \delta M / \delta E = 1 \times 10^{-2} \text{ Gauss-cm/V}$  was estimated. In both cases discussed above the nanostructures were epitaxial both in-plane

and out-of-plane (three dimensional heteroepitaxy) as verified by X-ray diffraction and high resolution TEM studies.

Nan *et al.*<sup>119</sup> investigated theoretically the magnetic field-induced electric polarization in ferroelectric-ferromagnetic nanostructured films using a Green's function approach. The calculations clearly showed that the ME effect was significantly larger in (001)-oriented nanostructured films having ferromagnetic nanopillars (with radius much smaller than the height) embedded in a ferroelectric matrix than those having nanolaminates connected through a single contact plane creating a large in-plane constraint.

A synthesis method combining sol-gel and electrochemical deposition processes using anodized nanoporous alumina membranes has been developed to grow  $\text{NiFe}_2\text{O}_4$ -PZT core-shell nanowire arrays.<sup>120</sup> The PZT nanotubes were fabricated in anodized alumina membranes, which were then filled with  $\text{Ni}_{33}\text{Fe}_{67}$  alloy by electroplating. The subsequent oxidation resulted in the formation of 30  $\mu\text{m}$  long  $\text{NiFe}_2\text{O}_4$ -PZT core-shell nanowire arrays with an average core diameter of  $\sim 140$  nm and a circular shell with a mean thickness of  $\sim 30$  nm. No measurements on the ME effect have been performed on such structures yet.

### 3. Applications

Ferrites are an important class of materials for use in microwave passive devices such as phase shifters, circulators, filters, isolators, and resonators.<sup>103, 121</sup> Depending on the frequency of operation, different types of ferrite materials are needed and used. Because

ferrites are magnetic dielectric materials (unlike magnetic metals which are conductive) they permit electromagnetic penetration and thus interaction between the electromagnetic wave and magnetization within the ferrite. Ferrite devices permit the control of microwave propagation by a static or switchable DC magnetic field. The devices can be reciprocal or nonreciprocal, and linear or nonlinear. What is certain is that their development requires a strong knowledge of magnetic materials, electromagnetic theory, and microwave circuit theory.

A transmit/receive module which is commonly used in microwave systems is ideal for representing many microwave passive components. A schematic diagram of a phased-array antenna module containing a transmit/receive circuitry is illustrated in [Figure 14](#). The module contains two transmitter/receiver switches (typically made of high speed pseudomorphic modulation doped FETs), amplifiers, a phase shifter, and two circulators. Phase shifters, circulators, filters, and isolators are made possible due to the unique microwave properties of the ferrites. Critical fundamental properties of all microwave ferrites as pertained to passive devices can be grouped as follows.<sup>121</sup>

- **Faraday Rotation** : The rotation of the plane of polarization of a TEM wave as it propagates through a ferrite in the direction of the magnetization. Application of Faraday effect has allowed the development of the isolators for total waveguide band for all standard waveguides. A typical Faraday rotation device is composed of a cylindrical waveguide loaded by a longitudinally magnetized ferrite rod, details of which are provided in [Section 3.4](#), “isolators”.

- ***Ferromagnetic resonance (FMR)*** : The strong absorption that can occur when an elliptically polarized RF magnetic field is perpendicular to the direction of magnetization. See [Sections 4.1, 4.2, and 4.6](#) in [Part 1 \[1\]](#) for details.
- ***Field displacement*** : The displacement of the field distribution transverse to the direction of propagation resulting in more or less field in the ferrite region.
- ***Nonlinear effects*** : At higher power levels amplification and frequency doubling are possible and subsidiary losses can occur.
- ***Spin waves*** : Short-wavelength waves of magnetization that can propagate at any angle with respect to the direction of magnetization. If the wavelength of such a wave is comparable to the dimensions of the ferrite sample, it is called a magnetostatic wave (MSW).

### 3.1. Phase shifters

Microwave phase shifters are important elements for use in oscillators and phased array antenna systems. Traditional ferrite phase shifters of millimeter and sub-millimeter wave bands are based on Faraday rotation for electromagnetic waves in axially magnetized ferrite rods in waveguides. The introduction of phase-array radar has spawned a lot of interest in fast-response, electrically controlled phase shifters. The ferrite digital phase shifter, or latching phase shifter as it may also be called, is a passive device in which a toroid of square-loop ferrite is placed so as to interact with the microwave signal. For example, if the ferrite slabs, which are magnetized in the same direction, extend from the top to the bottom of a waveguide are placed against each of the sidewalls of the waveguide, a phase shift of  $360^\circ$  may be obtained with a loss of less than 1 dB in  $X$



band.<sup>127</sup> The applied field cannot be too high to cause ferrite resonance losses. Therefore, for a given phase shift per unit length, the maximum value of applied field determines the minimum thickness of the ferrite slab required. There exists also an upper limit for thickness because when the ferrite slabs are too thick, a cutoff phenomenon occurs giving rise to high attenuation even at magnetic fields well below that which corresponds to the resonance. A nonreciprocal phase shifter that has different phase shifts in opposite directions of propagation in a waveguide may be obtained with one ferrite slab or with two slabs symmetrically placed, with respect to the center of the guide, but oppositely magnetized.

A nonreciprocal Faraday rotation phase shifter is shown in Figure 15. The principle of operation of a phase shifter can be described as follows. A rectangular waveguide mode entering at the left is converted to a circular waveguide mode with a short transition section. A quarter-wave dielectric plate oriented  $45^\circ$  from the electric field vector converts the wave to a right-hand circularly polarized wave by providing a  $90^\circ$  phase difference between the field components that are parallel and perpendicular to the plate. In the ferrite-loaded region the phase delay is  $\beta_+z$ , which can be controlled with the bias field strength. The second quarter-wave plate converts the wave back to a linearly polarized field. The operation is similar for a wave entering at the right except now the phase delay is  $\beta_-z$  which means the phase shift is nonreciprocal. The ferrite rod is biased longitudinally in the direction of propagation with a solenoid coil. This type of phase shifter can be made reciprocal by using nonreciprocal quarter-wave plates to convert a linearly polarized wave to circular polarization for either propagation direction.

For application in radar systems, which do not require broad frequency bands, phase shifters have been developed for operating frequencies up to 100 GHz with an operation frequency band of 90-100 GHz (within 10% of the resonant frequency).<sup>122</sup> This type of phase-shifters may produce a maximum value of controlled phase shift of up to  $500^\circ$  and have average losses of 0.7 - 1.2 dB at 35 GHz.<sup>122</sup> The loss increases to 2.0-2.7 dB when the frequency is increased to 100 GHz. The total control cycle time, time required to achieve the controlled phase shift maximum, depends on the construction and intended application of the phase-shifter and varies from 10  $\mu$ s up to 200  $\mu$ s. Phase-shifters that provide a controlled phase shift of  $450^\circ$  at average losses 1.3 dB at frequency 70 GHz are typical.<sup>123</sup>

Ferrite-film miniature delay lines are also of interest for high-frequency signal processing.<sup>124,125</sup> These devices are based on the propagation of magnetostatic spin waves (MSWs) in the ferrite film which is situated across two microstrip transducers. The electromagnetic (EM) signal fed to the input transducer excites MSWs in the film that propagates toward the output microstrip where it is converted back to the EM signal. The group velocity and the wavelength of the MSWs are two orders of magnitude smaller than those of the EM waves of the same frequency. This makes possible a propagation delay time of about 10–500 ns for a propagation distance of several millimeters in the film.

An interesting reciprocal ferrite phase shifter has been investigated by Reggia and Spencer<sup>126</sup> (Figure 16) in which a longitudinally magnetized ferrite rod is coaxially and centrally located in a rectangular waveguide. In this configuration large phase shifts have been obtained with low applied magnetic fields. The observations have been explained by concentration of most of the electromagnetic energy in the ferrite material due to its relatively high dielectric constant ( $\sim 10 \epsilon_0$ ) giving rise to large phase shifts as the applied field is varied with accompanying changes in permeability.

All of the above mentioned devices require an electromagnet or solenoidal magnetic field for EM control since a bias magnetic field  $H$  is necessary for the operation and frequency tuning of these devices. This requires high electrical power for operation and involves large power dissipation, and it is bulky. Moreover, such a magnetic tuning is inherently slow and noisy. Just as critical, it should be noted this makes the device miniaturization difficult and incompatible with integrated circuit technology. However, development of new generation of radar and communication systems created a need for novel tunable signal processing devices with possibility of rapid switching from one frequency of operation to another.

### 3.2. Circulators

As in the case of phase shifters, a circulator is also a passive microwave component with three or more ports. The ports can be accessed in such a way that when a signal is applied to any port it is transferred to the next port, the first port being counted as following the last in numeric order. When one port of a three port circulator is terminated in a matching load, it would act as an isolator. Isolators and circulators are the most widely used ferrite

type non-reciprocal passive microwave components. There are three types of waveguide lines predominantly used in microwave systems: rectangular waveguides, coaxial lines, and strip (microstrip) lines including co-planar waveguides. In all cases, single-mode propagation conditions are attempted.

The three port version of circulators, called the Y- junction circulators and the isolators based on them, are the most widely used and they can be constructed in the waveguide or stripline form. The former is usually an H-plane version although E-plane versions can also be made. Considerably wide range of applications is provided by 4-port circulators in microstrip forms. But the rf powers in both types of circulators decrease rapidly with increasing frequency because of limited possibilities of standard single-mode waveguides.<sup>127</sup>

In microwave communications and ranging systems relying on a single antenna aperture for both sending and receiving (as in cell phones), the function of circulators or switches is primarily to facilitate the routing of outgoing and incoming signals to the transmitter or receiver as needed, as shown in Figure 14. Detailed design theories for circulators have been developed primarily for rectangular waveguide, stripline, microstrip line, and image guide.<sup>128,129,130,131</sup> As mentioned above, circulators fall into two main categories, namely 4-port waveguide circulators and 3-port "turnstile" or "Y-junction" circulators. The 4-port waveguide circulators are based on Faraday rotation of propagating waves in a magnetized material. The basis for a 3-port circulator is on cancellation of waves propagating over two different paths near a magnetized material. As alluded to above, the three-port circulator is the most frequently used type of circulator. A circulator utilizing

the Faraday rotation is schematically shown in **Figure 17**. As seen from the figure, the circulator is a planar junction with three waveguides spaced at  $120^\circ$  angular intervals. Centrally located ferrite post, the properties and dimensions of which are set up so that each arm is perfectly matched at a given frequency, is the key to the operation of the circulator. As the geometrical symmetry indicates if all the power into one of the ports is made to come out of the adjacent port, then this will hold for all three ports, and the device would function as a circulator.<sup>132,127,133,134</sup>

EM wave entering port 1 will not emerge from port 3. Instead, when traveling from port 1 to port 2, the electric field  $E$  is rotated clockwise  $45^\circ$  in the ferrite and is therefore in the right direction to emerge from port 2. On the other hand,  $E$  of the wave traveling from port 2 toward port 1, having been rotated another  $45^\circ$  is in the wrong direction to pass to port 1, but in the right orientation to pass to port 3. By direction we mean polarization. Thus it emerges from port 3. On the other hand  $E$  of the wave from port 3 travels toward port 2, rotates an additional  $45^\circ$ , making the total rotation  $90^\circ$ . Therefore it is reflected from port 2 but emerges out of port 1 since  $E$  of the wave traveling from port 2 to port 1 will rotate another  $45^\circ$ , and is therefore, in the wrong direction to emerge from guide port 3. However, it is in the right direction to emerge from port 1. The nomenclature circulator comes about because the energy goes from port 1 to port 2, and then to port 3, and back to port 1 again. The attenuation from port 1 to port 2 is typically about 1 dB (the lower the better) while that from port 1 to port 3 is in the range of 10-35 dB (the higher the better)

Elaborating further, circulators can be based on field-dependent phase shifters or on phase shifters which shift phase of electromagnetic waves of different polarization by different amounts. In the device shown in **Figure 17**, an EM wave fed into port 1 comes out through waveguide port 2, that into port 2 comes out of 3, and that into 3 comes out of 1. This is possible if the phase shift between the ports is  $60^\circ$  in one direction, but  $120^\circ$  in the opposite direction. The symmetry of the device divides the input at any port into two paths. Recombining at each of the two ports, the two halves of the signal are  $180^\circ$  out of phase at one (rejection), but exactly in phase at the other (transmission).

Microwave integrated circuits require components with ever decreasing dimensions. However, the microstrip circulators require strict tolerance of the ferrite discs fitting into holes drilled in the dielectric substrate. Therefore, the fabrication costs are high. One approach in the past has been to use “drop-in” type circulators at higher frequencies where tolerances are small.<sup>135</sup> A drop-in microstrip circulator is schematically shown in **Figure 17(b)**. There is a need for simplified drop-in type circulators which can be easily incorporated within a planar geometry. Considerable fabrication simplification has been achieved by placing the ferrite disc on top of a dielectric substrate in a circulator design by Stern and Babbitt<sup>136</sup> who showed that these circulators exhibited low insertion losses and a high isolation near 35 GHz.

### 3.3. Filters

A microwave filter is in essence a two-port network employed to control the frequency response by transmitting frequencies within a pass band preferably with no loss and fully

attenuating those falling outside the pass band (stop band). As in just about all microwave systems and components, investigation of filters is important and also it dates back to World War II. Tools have been developed for filter design among which is the insertion loss method. In this method a cascade of relatively simple two-port filter sections is used in order to achieve the desired frequency response.<sup>131</sup> Tunable filters would have added advantages in the microwave system and could be made adaptable to changing challenges.

Microwave filters and oscillators that are electronically tunable *e.g.* over a decade in frequency rely on FMR in ferrites (see Section 4.6 in Part 1).[1] FMR is known to result in absorption of incident microwave energy at a characteristic frequency determined by properties of a given ferrite. The FMR frequency is dependent on the anisotropy field,  $H_a$ , which can be modified by chemical composition of the ferrite material. Typically,  $H_a$  is supplemented by an externally applied bias field,  $H_o$ , which increases the FMR frequency. Applied stress can also have the same effect. In fact, strain can be induced through electromechanical coupling using a piezo material for electrical tuning which is attractive (see Section 3.6).

The basic idea of the magnetic resonance filter can best be described using Figure 18. Two coils have their axes aligned at right angles to each other, and a small ferrite sample is placed at the intersection of the coil axes. When the ferrite sample is not magnetized, power is not transferred between the coils because the loop axes are orthogonal to each other and there is no interaction with the ferrite. When an external DC magnetic field  $H_0$  is applied in the  $z$ -direction and AC current ( $I_x$ ) is applied to the input coil (x-coil),

however, the magnetic moment of the electrons in the ferrite precess around the  $x$ -axis. This produces an RF magnetic moment along the  $y$ -axis and induces a current ( $I_y$ ) in the  $y$ -coil. The precession angle and the induced voltage in the output coil ( $y$ -coil) are maximum at ferromagnetic resonance, which is determined by the DC magnetic field applied to ferrite. The filter function is achieved when RF signals deviate from the dipole resonant frequency by more than some amount and do not couple to the ferrite sphere. The radius of the coupling loops acts to control the external Q-factor of the resonator, the minimum values of which are determined by the excitation of MSW resonances.<sup>137</sup> The external Q-factor is determined by the volume of the resonator and the material and the details of the coupling circuits. Efforts have focused on size reduction, compatibility with packaging, and integration into higher level assemblies. Yttrium iron garnet (YIG) tuned filters are widely used in microwave communication systems with frequencies ranging from 500 MHz to 26.5 GHz, as they can cover a broad frequency bandwidth of up to a decade with excellent power handling capability and tuning linearity.<sup>121,138</sup>

Because hexaferrites have a large anisotropy field,  $H_a$ , they have been used in tunable filters operating at 60 GHz and above.<sup>139</sup> Use of these ferrites resulted in a 50% reduction in external magnet power required. The negative permeability shown by ferrite materials at frequencies higher than the FMR enables MSW propagation in structures with small cross section over a limited range of frequencies. Filters can be built using MSW concepts in both delay line or resonator configurations. Filters based on MSW delay lines have been demonstrated in the 3-7 GHz range with a bandwidth of 30-50 MHz.<sup>138</sup> By careful adjustment, MSW straight edge resonators can be attained through placement of a



ferrimagnetic resonator cavity on a thin film transducer structure. Hexagonal ferrite bandpass filters have also been achieved with loop coupling. However, the more common method relies on the use of waveguide inputs and outputs and multiple ferrite spheres instead of a single one as in Figure 18. For example, in a two-sphere filter, where the two spheres are synchronously tuned by applying a DC bias magnetic field, the coupling between the spheres is provided by an iris in a conducting wall separating the input and output waveguides.<sup>137</sup> By changing the iris diameter and the sphere size and by adjusting the sphere spacing the coupling between the spheres can be changed, i.e. bandwidth, filter insertion loss, and off-resonance isolation can be controlled.<sup>140</sup> Similar to YIG filters the input and output waveguides can be crossed at  $90^\circ$  angles to create a magnetic field mode mismatch (RF magnetic fields in the two waveguides perpendicular to each other at the iris) and increase the off resonance isolation. If a ferrite material with a high  $H_a$  is available the applied magnetic field needed to tune to high frequencies could be greatly reduced. One, two, three and four sphere filters have been produced using hexagonal ferrites for millimeter wave operation.<sup>139,141,142</sup>

### 3.4. Isolators

An isolator is a two-port device that transfers the forward power from input to output with little attenuation but dissipates the power propagating in the opposite direction. The typical applications of isolators include the coupling of an RF microwave generator to a load. The advantage is that almost all the entire power from the generator can be delivered to the load while the reflected power from a mismatched load does not flow back to the generator. A microwave isolator is a transmission line with nonreciprocal

attenuation. Isolators have important applications in microwave systems. For example, one application has to do with reducing the frequency pulling of an oscillator caused by reflections from the load. Another application involves high-gain traveling-wave tube amplifiers. Isolators offer certain advantages over circulators in regard to size and cost. In applications that do not require the full range of circulator capabilities, a small low-cost isolator may be preferable over a circulator converted into an isolator by connecting a matched load to one of its ports. A ferrite isolator has three necessary components: a transmission line, a ferrite part, and a DC biasing magnetic field applied to the ferrite. There are three types of isolators classified by the principle of operation: resonance isolator, field-displacement isolator (also known as edge/side mode or peripheral mode), and junction isolator (Faraday isolator). A junction isolator can be realized by terminating one of the ports of a circulator with a matched load as mentioned above.

The most commonly used isolator is the resonance isolator. The operation of this kind of isolator requires biasing the ferrite material at its resonance. Advantages of resonance isolator over other isolators are the simple design and relatively small size of the ferrite disc used. A schematic of a resonance isolator is shown in Figure 19. The stub of the length  $\lambda/8$ , where  $\lambda$  is the wavelength, is connected to the main line so that the currents in the stub and in the main line are in quadrature. A ferrite disc is placed in the center of the junction, where the magnetic field is polarized circularly. Compensation of the reactance of the stub is obtained by using an additional stub of the length  $3\lambda/8$ . The diameter ( $d_f$ ) of the disc should be equal to  $2-3 W$ , where  $W$  is the width of the stub. The basis for operation relies on the phenomenon of ferromagnetic resonance between the circularly

polarized rf magnetic field and the precessing electron spins in the ferrite. One of the disadvantages of resonance isolators is the large external magnetic field that has to be applied to the ferrite. A resonance isolator consists of a transmission line which operates in a mode that provides a circularly polarized rf field in some region, and a ferrite piece which is situated in this region and magnetized perpendicular to the plane of circular polarization. When an electromagnetic wave propagates along one direction of the transmission line, the sense of rotation of the polarized rf magnetic field is such that it is synchronous with the precessional motion of certain electron spins in the ferrite. The frequency  $f$  at which ferromagnetic resonance absorption occurs in the ferrite cylinder can be derived approximately by using relationships described in [Section 4](#) in [Part 1](#).<sup>[1]</sup> Because of damping effects associated with the precession, rf energy is absorbed in the ferrite. The magnitude of the applied DC magnetic field determines the frequency of precession which is chosen to be equal to the signal frequency of the rf signal. In this case the precessional motion becomes strong, the dissipation of rf energy in the ferrite becomes large, and thus the electromagnetic wave is attenuated. This is called FMR absorption. If the wave propagates in the reverse direction, the rf magnetic field is circularly polarized in the opposite sense and does not interact with the precessing electron spins. Therefore, the wave remains essentially unattenuated in this direction.

The “edge-mode” isolator consists of a wide strip conductor on a ferrite substrate that is magnetized normal to its plane.<sup>121</sup> A resistive sheet is placed along one edge of the strip conductor. Operation of the device is through the field displacement induced by the gyromagnetic properties of the magnetized ferrite. Because the strip conductor must be

very wide in order to produce the desired nonreciprocal attenuation, the characteristic impedance is very low.

Ferrite isolators using a helical transmission line have been developed many decades ago.<sup>143</sup> The main relative advantage of this type of isolator is that an external magnetic bias field is not needed. This has been achieved by using closed rings of soft ferrites with a square-loop magnetization curve. Although this type of isolator is designed primarily for use in traveling-wave tubes, it must also find other applications to be viable. By appropriate modifications, it can be used not only as an isolator, but also as a switch or a modulator with helical as well as hollow waveguide and coaxial lines. Figure 20(a) shows a schematic representation of the above discussed isolator. The two essential components of the isolator are a helical transmission line and a ferrite cylinder. The remanent magnetization,  $M_r$ , to saturation magnetization,  $M_s$ , ratio, i.e. squareness ratio  $M_r / M_s$ , for the ferrite should approach one. The ferrite cylinder is permanently magnetized in circumferential direction achieved by passing a current through the cylinder as shown in Figure 20(b). The passing current magnetizes the cylinder circumferentially and saturates the ferrite if the magnetic field produced by the current is sufficiently large for the particular ferrite. Because the ferrite is in the form of a closed ring, it remains nearly saturated even when the current is removed. The rf magnetic field outside the helical transmission line is circularly polarized in a plane perpendicular to the magnetization in the ferrite. This results in nonreciprocal attenuation at the ferromagnetic resonance frequency of the ferrite. The directions of propagation that give large and small loss are

indicated in Figure 20 for the direction of magnetization indicated by  $\mathbf{M}$ . If the magnetization is reversed, the directions of large and small loss will be interchanged.

Isolators can also be constructed from circulators. When one port of a three port circulator is terminated in a matching load, it would function as an isolator. Figure 21 illustrates a sample junction microwave isolator where the ferrite element is placed in the waveguide, and a magnetic bias field is applied externally (ideally the internal bias would be sufficiently large obviating the need for an external magnetic field to be applied). A waveguide, circular in cross section for coaxial varieties, is nearly filled with ferrite material. The ferrite slab is situated in this plane and must therefore be relatively thin. Electromagnetic wave traveling in one direction in the ferrite slab possesses one direction of circular polarization, while that in the opposite direction has the other. The sense of rotation of a circularly polarized electromagnetic wave propagating in one direction is such that it is synchronous with precessional motion of electron spins in the ferrite because of which the rf energy is absorbed in the ferrite. The electromagnetic waves propagating in reverse direction, however, have the opposite sense and do not interact with the precessing electron spins. The magnitude of the applied dc magnetic field determines the frequency of the precession and is chosen so that it is equal to the signal frequency of the rf signal.

Microwave isolators have also been constructed by making use of the large ratio of permeability  $\mu$  for the two polarizations, well away from resonance. For the polarization having lower permeability the waveguide has a higher cutoff frequency than in the

opposite polarization. In the region between the two cutoff frequencies the waveguide is unidirectional, meaning the wave outside of the band is not transmitted. The energy which is not propagated here is largely reflected back to its source, which may cause problems in high-power ferrite devices, since temperature can rise above the Curie point due to power dissipation.

### **3.5. Miniature antennas**

The antenna is a component that converts a wave propagating on *e.g.* a transmission line to plane waves in free-space (transmission), or vice versa (reception), and as such a critical component in communication and ranging systems. There exist a wide variety of antennas developed to suite a plethora of applications. *Wire antennas* are mostly used at lower frequencies, and have the advantage of being light weight, low cost, and simple in terms of design. This type of antennas includes dipole, monopole, loop, and sleeve dipole varieties. *Printed antennas* include printed slots, printed dipoles, and microstrip patch antennas. These types of antennas are mostly employed at microwave and millimeter wave frequencies. They can be fabricated by conventional photolithography methods along with the necessary feed circuitry on dielectric substrates. *Aperture antennas* are those with open-ended waveguides, rectangular or circular horns, reflectors, and lens varieties. These antennas are also used at microwave and millimeter wave frequencies. *Array antennas* feature a regular arrangement of antenna elements with a feed network. Pattern characteristics such as beam pointing angle and sidelobe levels can be controlled by adjusting the amplitude and phase distribution of the array elements. An important type of array antenna is the phased array, where variable phase shifters are used to

electrically scan the main beam of the antenna without moving parts for agility and compactness.

### 3.5.1. Microstrip Antennas

Of special interest to this review is the small sized antenna, among which is the microstrip antenna that is easily integrable with the other passive components on the microstrip substrate. The concept of the microstrip antennas dates back to the 1950s.<sup>144,145</sup> Since then they have received considerable attention owing to their relatively smaller back radiation, higher efficiency, larger bandwidth, and lower mutual coupling than the ferrite printed antennas. A *microstrip* device in its simplest form is composed of a sandwich of two parallel conducting layers separated by a single thin dielectric substrate. The lower conductor functions as a ground plane while the upper conductor may be a simple resonant rectangular or circular patch, a resonant dipole, or a monolithically printed array of patches or dipoles along with the associated feed network. The basic configuration of a microstrip antenna is a metallic patch printed on a thin grounded dielectric or ferrite substrate as shown in Figure 22.<sup>146</sup> Practical microstrip antennas have been developed for use at frequencies ranging from 400 MHz to 100 GHz. The driving force for the development of microstrip antennas has been the need for antennas with low-profile, low-weight, low-cost and polarization diversity that can easily be integrated into arrays or with microwave integrated circuits. The original microstrip antenna configurations have some disadvantages among which are the narrow bandwidth, spurious feed radiation, poor polarization purity, limited power capacity, and tolerance problems. For all practical purposes the bandwidths of these antennas are limited to about

2%-5% of the central (resonant) frequency. Therefore, much of the developments in microstrip antennas have centered on attempts to overcome these problems in order to meet increasingly stringent systems requirements. This effort has involved the development of novel microstrip antenna configurations as well as the development of accurate and versatile analytical models for their design and optimization.

Different shape patches including rectangular,<sup>147,148</sup> circular,<sup>149,150</sup> and square spiral<sup>154</sup> have been developed. The antenna element is fed with either a coaxial line through the bottom of the substrate, or by a coplanar microstrip line. Despite steady progress many challenges remain for increased performance, among which are narrow bandwidth, poor polarization purity, limited power capacity, and tolerance problems. The focus on microstrip antennas has been aimed overcoming the aforementioned obstacles in order to meet the increasing systems requirements. The efforts involved development of novel microstrip antenna configurations and optimization using various accurate and versatile analytical models. Three types of losses are encountered in microstrip antennas: conductor loss, dielectric loss, and surface wave excitation.<sup>151</sup> Typically, conductor and dielectric losses in a microstrip element are very small (except for extremely thin substrates), and usually account for a few percent loss in the radiation efficiency. Unwanted surface waves at the dielectric substrate can also be excited by the antenna. Because they do not contribute to the primary radiation pattern of the antenna, surface wave power is generally considered as the main loss mechanism.



When in the transmitting mode, the antenna is driven with a voltage between the feed probe and the ground plane. This excites current on the patch and a vertical electric field (vertical polarization) between the patch and the ground plane. The dielectric substrate is usually electrically thin ( $d < 0.05\lambda_0$ ), so the electric field components parallel to the ground plane must be very small throughout the substrate. The patch element resonates when its length  $L$  is near  $\lambda/2$ , leading to relatively large current and field amplitudes. The antenna can be viewed as a cavity with slot-type radiators at  $z = 0$  and  $z = L$ , with equivalent magnetic currents,  $\mathbf{M} = \mathbf{E} \times \hat{n}$  radiating in the presence of the grounded dielectric substrate, where  $\hat{n}$  is the unit vector normal to the ground plane and  $\mathbf{E}$  is the electric field between the patch and the ground plane.

The efficiency and bandwidth of a microstrip element is shown vs. the substrate thickness in [Figure 23](#), where two important trends are observed: the bandwidth increases with substrate thickness and decreases with increasing substrate permittivity,  $\epsilon$ . The surface wave power generated by a single element decreases with substrate thickness and dielectric constant. It is, therefore, desirable to have an electrically thick substrate with a low dielectric constant for better antenna performance. However, a thin substrate with a high dielectric constant is preferred for microstrip transmission lines and microwave circuitry. This then necessitates a compromise between good antenna performance and good circuit performance. The root cause of this problem is the diverging electrical functions of the antenna radiation and circuitry where antennas require loosely bound fields for radiation into space, while circuitry requires tightly bound fields to prevent undesired radiation or out coupling.

### 3.5.2. Miniature antennas using ferrites

As part of the renewed interest in ferrites, in particular the thin-film technology, insertion of ferrimagnetic thin films in microwave and millimeter-wave integrated circuits is also extending to cover miniature antennas. Applications of ferrite technology in millimeter-wave scanning array antennas are considered critically important. To reiterate, this is to a large extent due to the fact that ferrites belong to a material group with nonreciprocal characteristics and can be tuned electronically with external electric field. The use of biased ferrite layers in the printed circuit form to obtain novel antenna and array characteristics has already been investigated extensively, both from the theoretical and experimental points of view.<sup>144,148,151,152,153,154</sup> Consistent with the overall driving forces mentioned above, integration of ferrite technology into microwave-millimeter wave integrated circuits provides miniaturization, lower cost, and compatibility in monolithic microwave integrated circuits (MMIC).

High permittivity and/or high permeability dielectric materials can be used to reduce the antenna size. Among the antennas using high permittivity material is the conventional cavity backed slot (CBS) antenna. The high permittivity of dielectrics used to miniaturize CBS antennas results in a reduction of bandwidth, efficiency, and gain. To circumvent this set of problems, ferrites with their high permeability, instead of high permittivity dielectrics, have been used. Because of their anisotropic and frequency dependent features, ferrites possess attractive properties as far as passive microwave components including devices under consideration, antennas, are concerned. The most attractive

feature is naturally the electronic tunability. Because the material properties of the ferrites can be tuned by a biasing static magnetic field produced by a coil or an electromagnet, unlike the standard dielectrics (in ferroelectric materials the permittivity can be changed with electric field), the resonance frequency can be dynamically tuned. Ideally with composite bilayers, tuning with electric field would be possible. It should be noted that the magnetic polarization of the medium can also be controlled simply by the amount of DC current applied to the Faraday rotator coils. With such tuning several frequency bands can be transmitted and received using the same antenna. This translates to reduction of the number of antennas, and therefore cost, volume, weight, and complexity. Also high dielectric constant of the ferrites brings about an additional reduction in the antenna dimensions. These unique properties of ferrite antennas have been recognized independently as early as late 1950s by several researchers.<sup>155,156,157</sup> Tuning by magnetic coils, however, is inconsistent with ultimate miniaturization, making the electrical tuning by using ferroelectric and ferrite materials a more preferable method.

Microstrip antennas using ferrite substrates were simulated by Das and Chowdhury.<sup>158</sup> Through a theoretical analysis these authors showed the possibility of realizing microstrip resonator structures at low frequencies, where miniaturization is more critical due to long wavelengths involved, by building them on ferrimagnetic substrates, which possess both high dielectric permittivity and magnetic permeability.<sup>158</sup> The resonant frequency in a microstrip antenna is given by<sup>158</sup>

$$f_r = \frac{c}{2L_{eff} (\mu_{eff} \epsilon_{eff})^{1/2}} \left[ \sqrt{n^2 + m^2 \left( \frac{h}{w} \right)^2} \right]^{1/2}$$

**Equation 52**

where  $c$  is the speed of light in vacuum,  $\mu_{eff}$  and  $\epsilon_{eff}$  are the relative permeability and permittivity, respectively, of the substrate material,  $L_{eff}$  is the effective resonant length of the antenna,  $m$  and  $n$  are integers, and  $h$  and  $w$  are the height (metal thickness) and width, respectively, of the microstrip antenna. It is apparent that when the substrate material possesses large permittivity and permeability the effective length of the antenna can be reduced for a given resonance frequency. It should also be noted impedance matching is desirable in antennas to couple radiation efficiently and to have large bandwidth, which requires the ratio of permeability to permittivity to remain constant since the effective inductance of the microstrip antenna is given by

$$L = \frac{\mu_0 h n c}{2 w f_r} \sqrt{\frac{\mu_{eff}}{\epsilon_{eff}}}.$$

**Equation 53**

Larger bandwidth and smaller size (effective resonant length) were predicted at a particular frequency of operation for microstrip antennas on ferrite substrates relative to those on purely dielectric substrates.<sup>158</sup> Experiments performed by the same group<sup>159,160</sup> revealed resonant length and impedance bandwidth values in good agreement with the theoretical predictions.

There are various approaches for realizing ferrite-based antennas: bias fields can be applied in different directions, ferrite materials can be used as substrates or multilayers in combination with dielectrics. Patch antennas on ferrite substrates allow for radiation pattern control, frequency shifting, and scattering reduction, all of which can be achieved

by external magnetic field biasing coupled with the intrinsic magnetization of the ferrite medium. Again, ideally using the bilayer approach electrical tuning of magnetic property is possible, which is attractive for tunable as well as miniaturized antennas. When biased with a magnetic field the ferrite antennas exhibit a number of novel properties among which is 15-40% frequency tuning, the generation of two opposite hands of circular polarization, and the possibility of beam steering. The operational bandwidth of antennas is in the range of 1 – 100 GHz using a single element antenna or array antennas. The physical size of the antenna at the low-frequency end, however, is too large to be practical for many applications. In other words, the profile becomes prohibitively large because the ground plane or the cavity spacing must be a quarter wavelength at the lowest frequency of operation to ensure that the direct and reflected waves are in phase in the forward direction.

The radiation frequency spectrum of a rectangular microstrip patch antenna deposited on a ferrite substance has been measured.<sup>161</sup> In this particular investigation, the ferrite substrate was made of YIG material with a thickness  $d = 1.25$  mm, permittivity  $\epsilon_r = 14$ , and a saturation magnetization  $4\pi M_s = 1700$  G. The patch was  $L = 1.8$  cm long and  $W = 1.4$  cm wide, and was fed by a coaxial line along one edge of the patch antenna. An electromagnet was used to externally bias the device and the maximum external field applied was 31 Oe at the center of the patch antenna. Two different radiation modes whose frequencies behaved differently under the application of a biasing magnetic field were noted. These two modes of radiation have been identified as a transverse mode ( $\perp$ ), whose radiation frequency increased with increasing magnetic field, and a longitudinal

mode ( $\parallel$ ), whose radiation frequency decreased with applied magnetic field. The longitudinal mode has been assigned to the propagation direction parallel to magnetization. Similarly, the transverse mode is associated with magnetization perpendicular to the propagation direction. A theoretical model was formulated for radiation of these two modes based on a multi domain configuration of the ferrite substrate. Using the rf permeability  $\mu_{\parallel(\perp)}$  for the longitudinal (transverse) mode, the resonance frequencies for the  $TM_{100}$  and  $TM_{010}$  modes were calculated by

$$f_{100}^{\parallel(\perp)} = \frac{c}{L\sqrt{(\epsilon_r\mu_{\parallel(\perp)})}}; f_{010}^{\parallel(\perp)} = \frac{c}{W\sqrt{(\epsilon_r\mu_{\parallel(\perp)})}}$$

Equation 54

and a good agreement between theoretical and experimental data was observed.

Yang<sup>152</sup> investigated the effects of an in-plane biased ferrite cover layer on the scattering characteristics of microstrip antennas by taking advantage of a full-wave moment analysis. Included in the analysis were such physical effects as the magnetic loss, magnetostatic waves, and dynamic surface waves. The geometry of the microstrip antenna studied in this particular investigation is shown in Figure 24. Significant radar cross section (RCS) reduction at resonance was observed if *i*)  $\mu_{\text{eff}}$  is much less than zero, and *ii*) the bias field is parallel to the main resonant current. It is well known that in dielectric ferrite materials an incident plane wave splits into two waves, namely the ordinary and extraordinary waves. It was shown that in such microstrip antennas having a ferrite cover layer the existence of a decaying extraordinary wave in the ferrite layer can decrease or prohibit the incident fields from reaching the antenna which results in

significant RCS reduction. As a result almost all of the antenna radiation power is converted into magnetostatic waves and little radiates into the medium of propagation. Analysis also demonstrated that microstrip antennas with a ferrite cover could be designed as switchable antennas. The control bias can switch the antenna from one state to another within a fairly broad frequency range. For a rectangular patch, significant RCS reduction was noted at resonances at which patch current is predominantly in the direction of the biased field.<sup>152</sup>

For many applications it is highly important that the polarization is electronically controlled and changed instantly *e.g.* from the polarization present to the next desired polarization. Another method to electronically achieve all the polarizations on the Poincaré sphere<sup>iii</sup> in a single antenna is a dual polarized antenna whereby the amplitude and phase of both ports can be varied independently. An alternate antenna design is composed of a half-wavelength and a quarter-wavelength phase shifter inside a circular waveguide with independent rotation drive for each phase shifter.

Dunn *et al.*<sup>162</sup> actually demonstrated a ferrite antenna that is capable of producing any polarization on the Poincaré sphere in the frequency range of 9.0 to 11.4 GHz. The ferrite antenna used consists of two Faraday rotators with a quarter-wavelength phase shifter between them. A cross sectional view of the antenna is displayed in **Figure 25**. In terms of the physical dimensions, the antenna shown in **Figure 25** has a diameter of 3.25 inches with an overall length of 8.12 inches that is slightly larger than the waveguide itself. The

---

<sup>iii</sup> named after Henry Poincaré; a three-dimensional graphical representation of the state of polarization of a light beam used to describe the polarization and changes in the polarization of a propagating electromagnetic wave.

polarization rotation of a Faraday rotator is nonreciprocal due to the ferrite hysteresis. The ferrite pencils have a hysteresis loop which must be considered when trying to achieve repeatable antenna measurements. It was discovered that a dispersion existed in the measured results depending on the history of the coil current. Essentially, a guided wave at the input port of the antenna undergoes a transition from rectangular waveguide to a dielectrically loaded circular waveguide. The wave travels through the input Faraday rotator, the quarter wavelength phase shifter, and the output Faraday rotator before being radiated into the free space through a dielectric rod aperture. All possible polarizations of the electromagnetic wave are attainable with this antenna including linear, circular, and elliptical polarizations. Any tilt angle of the elliptical polarization and any orientation of the linear polarization are also possible. The polarization of the ferrite antenna can be electronically switched to a different polarization instantly. Measured data showed very small cross-polarization values of 35 dB, axial ratios of less than 1.5 dB and a *voltage standing wave ratio* (VSWR) of less than 2.

To circumvent reduction in the antenna gain for broadband configurations at low frequencies due to metallic cavity backings, Kramer *et al.*<sup>154</sup> designed a reflective surface consisting of a ferrite and conductive coating. This approach proved to significantly improve antenna performance at lower frequencies as compared to the typical electrically conducting ground plane. The purpose of the ferrite material used in the outer region is to maintain the free-space antenna gain at low frequencies. On the other hand, the conductive center region served to increase the gain at higher frequencies. The backing tapers off to a conductive coating toward the center which makes it suitable for high



frequency operation. Such ferrite to metallic hybrid surface has been shown to improve the antenna performance significantly at lower frequencies without compromising the high frequency gain.

To summarize, microstrip antennas particularly those incorporating ferrites are one of the most innovative topics in antenna technology today, and this trend is likely to continue because the characteristics of microstrip antennas make them very attractive from the perspective of miniaturization and tunability desired in systems, particularly mobile varieties and phased array forms. It is not just the electrical characteristics of the basic microstrip antenna that are appealing but also the mechanical and fabrication features such as low-cost, lightweight, conformability, and easy integration with integrated circuits. Development aimed to improving the electrical characteristics of the microstrip antenna, such as increased bandwidth, novel feeding techniques, and control of spurious feed radiation are warranted which call for electrically tunable high permeability low-loss ferrites. The modeling of microstrip antennas and arrays is another issue where much work remains and doing so would provide versatile and accurate predictions of component properties. Materials with electric or magnetic anisotropy really form the backbone of this burgeoning technology in microstrip antennas and arrays. Incorporation of ferrite materials, which have received some but arguably insufficient attention to date for microstrip antenna applications, could pave the way for frequency agility, polarization agility, and beam steering in a thin and compact package.

### **3.6. Electrically tunable magnetic based passive components using magnetoelectric (ME) coupling**

In all passive microwave components, the challenges lie in size reduction, elimination of external bias, and electrical tunability. Also compatibility with packaging and or integration with other components on a preferably common substrate with higher level assemblies are highly desirable. Ferroelectric/ferromagnetic(or ferrimagnetic) bilayers (replacement for multiferroics using a bilayer stack) have been used for tuning magnetic properties in ferrites<sup>76,77, 163, 164, 165, 166, 167, 168</sup> and for various electrically controlled microwave passive components such as phase shifters,<sup>165,168</sup> resonators,<sup>77,166</sup> and delay lines.<sup>125</sup> Such pseudo-multiferroic structures are composed of ferrimagnetic and ferroelectric materials and the tunability is realized through the variation of a bias magnetic field that changes the magnetic permeability of the ferrite. In addition, application of an electric field  $E$  to ferroelectric brings about a compressive or tensile strain, depending on the direction of  $E$ , which gets transmitted to the ferrite resulting in a deformation of the ferrimagnetic film and leads to a change in magnetization  $M$  or the internal magnetic field in the ferrite. Ferrite-piezoelectric bilayers are ideal for studies of wide-band magnetoelectric interactions between the magnetic and electric properties that are mediated by mechanical forces. Such structures show a variety of magnetoelectric phenomena including giant low-frequency ME effects and resonance enhancement of ME coupling at electromechanical and magnetoacoustic resonance, and provide the possibility of simultaneous magnetic and electrical tuning.<sup>57,68,114</sup> Such a combination of ferrite and ferroelectric materials can be realized in a layered or composite structure. Microwave devices, fabricated using such ferrite-ferroelectric structures in a wide frequency range, are capable of fast electric switching between several closely situated discrete frequencies.

Tunability in microwave devices can be achieved by changing the dielectric constant ( $\epsilon_r$ ) of the dielectric layer by an applied electric field and/or the permeability ( $\mu_r$ ) of the magnetic layer by an applied magnetic field. The change is notable in ferroelectric materials in terms of the permittivity, and ferrites in terms of the permeability. Changes in the dielectric constant and/or the permeability, which may be considerably large near the Curie point, alters the resonance frequency  $f_r = 1/(2\pi\sqrt{LC})$  or the phase velocity  $v_p = 1/\sqrt{LC}$ , where the capacitance  $C$  and the inductance  $L$  per unit length are adjusted by varying  $\epsilon_r$  and  $\mu_r$ , respectively. When substantial changes in  $\epsilon_r$  and  $\mu_r$  are induced simultaneously, which may be achieved through the ME coupling, it is possible to keep the characteristic impedance  $Z_0 = \sqrt{L/C}$  constant so that the insertion loss in microwave devices such as phase shifters will not increase.

The ME effect may be utilized for tuning in devices where the piezoelectric material may be used to strain the magnetic material and change its properties such as the ferromagnetic resonance. Two-phase systems comprising PZT and magnetic garnet layers can be used as Faraday rotators, where the amount of rotation may be tuned by applying an electric field to the PZT. The electric field-induced polarization has been used in a field-effect transistor geometry to modify the charge density in the magnetic channel.<sup>169</sup>

An all-perovskite field effect device was fabricated using PZT as the ferroelectric gate and  $\text{La}_{0.7}\text{Ca}_{0.3}\text{MnO}_3$  as the magnetic channel grown on (001)-oriented single crystal  $\text{LaAlO}_3$  substrates by pulsed laser deposition, which allowed enhanced interface characteristics. When a positive voltage is applied to the gate, the ferroelectric

polarization causes positive charge buildup at the bottom side of the PZT gate, which attracts electrons from the p-type  $\text{La}_{0.7}\text{Ca}_{0.3}\text{MnO}_3$  channel. This results in depletion of the magnetic channel by holes. Consequently, the channel resistance increases at positive gate bias and decreases at negative gate bias. A modulation of channel conductance of more than a factor of 3 and a 3% change in the channel resistance after 45 min without power were demonstrated. Comparing the device characteristics with that of PZT/ $\text{La}_{0.7}\text{Ca}_{0.3}\text{MnO}_3$  capacitors grown under the same conditions, the channel modulation in the field effect device was proven to be due to the field effect rather than charge injection. Similar results have been observed in another study for inverted (back gated) field effect configurations having PZT gates and  $\text{La}_{0.7}\text{Ca}_{0.3}\text{MnO}_3$ ,  $\text{Na}_{0.7}\text{Sr}_{0.3}\text{MnO}_3$ ,  $\text{La}_{0.7}\text{Ba}_{0.3}\text{MnO}_3$ , or  $\text{La}_{0.5}\text{Ca}_{0.5}\text{MnO}_3$  channels.<sup>170</sup> The 50 nm-thick channels were deposited on PZT gate layers (150 nm) on conductive (100)-oriented Nb:SrTiO<sub>3</sub> substrates by pulsed laser deposition. The magnitude of the electroresistance was much larger in  $\text{La}_{0.7}\text{Ca}_{0.3}\text{MnO}_3$  channels than in others. The maximum electroresistance in  $\text{La}_{0.7}\text{Ca}_{0.3}\text{MnO}_3$  channels was also found to be much stronger, 76 % for an electric field of  $4 \times 10^5$  V/cm, than reported before,<sup>169</sup> and was observed to change sign with changing gate bias polarity. These results show that nonvolatile field effect devices can be realized using perovskite structure ferroelectric gate and a magnetoresistive channel materials.

Tunable microwave devices with superconductor/ferroelectric/ferromagnetic multilayers have also been proposed.<sup>171</sup> In addition to electrically controlled superconductor/ferroelectric structures such as  $\text{YBa}_2\text{Cu}_3\text{O}_7/\text{SrTiO}_3$ <sup>172</sup> and  $\text{YBa}_2\text{Cu}_3\text{O}_7/\text{Ba}_{1-x}\text{Sr}_x\text{TiO}_3$ ,<sup>173</sup> and magnetically controlled superconductor/magnetic structures such as

YBa<sub>2</sub>Cu<sub>3</sub>O<sub>7</sub>/Ferrite<sup>174</sup> and YBa<sub>2</sub>Cu<sub>3</sub>O<sub>7</sub>/YIG,<sup>175</sup> which can be used in filters, oscillators, and phaseshifters, YBa<sub>2</sub>Cu<sub>3</sub>O<sub>7</sub>/PZT/La<sub>0.7</sub>Sr<sub>0.3</sub>MnO<sub>3</sub> (200nm/30nm/30nm) superconductor/ferroelectric/ferromagnetic trilayer structures have been demonstrated, where simultaneous tuning of electrical and magnetic properties either with electrical or magnetic fields can be possible. The trilayer structures were grown by pulsed laser ablation on (001)-oriented LaSrGaO<sub>4</sub> and (La<sub>0.3</sub>Sr<sub>0.7</sub>)(Al<sub>0.65</sub>Ta<sub>0.35</sub>)O<sub>3</sub> substrates. The surface resistance of the YBa<sub>2</sub>Cu<sub>3</sub>O<sub>7</sub> was measured to be 1.32 mΩ at 77 K, below the critical temperature (87 K), which promotes the usefulness of these trilayer structures in microwave circuits.

The magnetic sensor devices based on ME coupling are of particular interest over the commonly used superconducting quantum interferometer device (SQUID) magnetometers, as they would cost less and can have cryogen-free room temperature operation. Detection of small magnetic fields has already been demonstrated using strain coupled ME composites made of a (001)-oriented 0.7[Pb(Mg<sub>1/3</sub>Nb<sub>2/3</sub>O<sub>3</sub>)-0.3[PbTiO<sub>3</sub>] (PMN-PT) single crystal laminated between two Terfenol-D strips (12 mm long, 6 mm wide).<sup>176</sup> The ME voltage induced by the magnetic field applied along the long axis of the strips across the thickness or the transverse direction of the piezoelectric layer was measured over a broad range of AC magnetic fields, 10<sup>-11</sup> to 10<sup>-3</sup> T. The EM voltage coefficient was 2.2 V/cm-Oe at a DC magnetic field of 400 Oe. The limit of sensitivity of the laminate to small magnetic field variations was 4 x 10<sup>-11</sup> T, which corresponds to an ME voltage of 30 nV. Induced ME voltage changes of 1 nV was suggested to be feasible using a lock-in detection system, corresponding to magnetic fields in the picoTesla range.

Similar laminated structures were used to demonstrate voltage gain using the ME effect.<sup>177</sup> The AC magnetic field was excited using a solenoid around the laminated composite and a voltage generator,  $V_{in}$ , which generated an AC magnetic field in the plane of the composite along the long axis. The induced ME voltage,  $V_{out}$ , was measured as a function of the input voltage frequency, and the maximum voltage gain was  $\sim 260$  at the resonance frequency (21.3 kHz) corresponding to the longitudinal vibrational mode of the laminate. The maximum voltage gain was naturally dependent on the DC magnetic field magnitude due to the field dependent magnetostriction of Terfenol-D. Such ME composite structures act as transformers, and they have the advantage of not requiring secondary coils with high-turns ratio like the conventional transformers, have significantly higher voltage gains, wider bandwidths, and higher power handling capability due to Terfenol-D compared to piezoelectric transformers, low input impedance and high output impedance, and may potentially be used in miniature solid state power transformers.

In microwave devices such as resonators, filters, and phases shifters utilizing ferrites, a bias magnetic field is used for operation and frequency tunability. The magnetic tuning can be achieved in a very wide range of frequencies, but it is inherently slow, noisy, and requires large power levels and massive equipment to produce static magnetic fields. Two-phase systems combining ferrite and ferroelectric materials can also provide frequency tunability over a relatively narrow range through the ME effect by electrical tuning, which is faster than traditional magnetic tuning and consumes almost no power. **Table 6** lists some of the ME coupling coefficients obtained from electrical field tuning in

piezoelectric/ferromagnetic bilayers. These two-phase ME systems provide the possibility of simultaneous magnetic and electrical tuning in miniaturized forms, where the magnetic tuning can be used over a wide range and the electrical tuning can be used for fast switching over a narrow frequency range.

In microwave delay lines employing ferroelectric-ferrite bilayers electrical tuning of the delay time by 25% has been demonstrated.<sup>125</sup> Schematics of the microwave delay line are shown in **Figure 26**. A 4.1  $\mu\text{m}$ -thick single crystal YIG layer grown on a (111)-oriented GGG substrate (2 mm x 25 mm) was bonded to a 0.5 mm-thick (001) single crystal PMN-PT ferroelectric (4 mm x 4 mm) using a fast-dry epoxy. The ferroelectric was poled perpendicular to the sample surface and the bilayer was placed on top of two microstrip transducers fabricated by photolithography on alumina substrates and separated by a distance of 8 mm. Application of a microwave electromagnetic signal to the input transducer launches magnetic spin waves in the ferrite film, which are converted back to electromagnetic waves at the output transducer. The wavelength and the group velocity of the magnetic spin waves, which are much smaller than those for the electromagnetic waves, can be controlled by the bias magnetic field or the electric field applied to the ferroelectric, introducing a change in the delay time. For a magnetic field applied parallel to the sample plane, an electric field (perpendicular to the sample plane) of 8 kV/cm could produce more than 25% decrease in the delay time, from 180 to 120 ns, within the transmission band (3.59 - 3.65 GHz). The delay time  $\tau$  was estimated from the phase shift  $\varphi$  measured as a function of the frequency  $f$  using  $\tau(f) = (1/2\pi) \partial \varphi / \partial f$ .

As discussed in Section 2.2.2 an electrical tuning range of up to 25 MHz has been realized for a YIG/PZT resonator structure shown in Figure 4.<sup>77</sup> A wider frequency tuning range has recently been demonstrated for resonators based on bilayers of single crystal YIG and PMN-PT.<sup>178</sup> A 7.5  $\mu\text{m}$ -thick YIG film grown on a (111) GGG substrate by liquid phase epitaxy was epoxy bonded onto a 500  $\mu\text{m}$ -thick (001)-oriented poled PMN-PT slab having Cr/Au (30 nm / 200 nm) electrodes on both surfaces. The bilayer was then placed on a microstrip transducer shorted at one end with the GGG substrate side facing the transducer. Compared to the standalone YIG film on the GGG substrate, the main FMR mode frequency shifted to a slightly higher value (from 4.8081 GHz to 4.8447 GHz at 1012 Oe) for the YIG/PMN-PT bilayer resonator. A similar shift was observed also when a copper plate was placed on the standalone YIG sample, which was well explained by the lowest spin wave mode dispersion equation derived from the theory for dipolar magnetostatic spin waves.<sup>187</sup> Figure 27 shows the frequency response for the YIG sample with and without the PMN-PT slab, and with the copper plate. It is evident from the broadening absorption linewidth and reduced peak absorption that the combination of YIG film with metallized PMN-PT slab leads to higher losses than the combination of YIG film and copper plate.

The increased loss in the YIG/PMN-PT bilayer was attributed by the authors to Ohmic losses in PMN-PT and to thin electrodes deposited on the PMN-PT slab surfaces.<sup>178</sup> However, it should be noted that the dielectric loss in PMN-PT may also have a significant contribution as especially highly piezoelectric ferroelectrics, particularly PMN-based relaxors, exhibit much higher loss tangent than low permittivity dielectrics at



microwave frequencies.<sup>179,180,181</sup> Since the skin depth at the FMR frequency (e.g. 1134 nm at 4.8081 GHz for Au) is significantly larger than the thickness of the electrodes on PMN-PT high microwave losses, therefore broader FMR linewidth and reduced peak absorption, are observed for the YIG/PMN-PT bilayer. Consequently, the thickness of the electrode between the YIG and PMN-PT layers is an extremely important parameter for the microwave applications of such bilayers. Note that for the resonator shown in **Figure 4** the Ag electrode thickness was 5  $\mu\text{m}$  (skin depth for Ag is 905 nm at 5 GHz) and the absorption width of the YIG/PZT bilayer was reported to be 3.4 MHz,<sup>77</sup> which is much smaller than  $\sim 22$  MHz for the YIG/PMN-PT bilayer with thin electrodes.<sup>178</sup> On the other hand, as repeatedly expressed throughout the discussion of the ME effect, as the thickness of the electrode and the bonding layer between the piezoelectric and magnetostrictive constituents is increased, the electromechanical coupling gets smaller.

For the resonator utilizing the bilayers of single crystal YIG and PMN-PT a frequency shift of 45 MHz was observed at an electric field of  $E = 8$  kV/cm for  $\mathbf{H}$  perpendicular to the resonator plane and  $E$  in the direction of the initial poling field for PMN-PT.<sup>178</sup> The shift was lower, 22 MHz, for the same electric field magnitude when  $\mathbf{H}$  was along the bilayer plane (see **Figure 28**). Wider tuning range in this YIG/PMN-PT resonator when compared to the YIG/PZT resonator in **Figure 4** (25 MHz shift at 10 kV/cm)<sup>77</sup> is most probably due to higher mechanical deformation (larger piezoelectric effect) in PMN-PT than in PZT and to larger electromechanical coupling resulting from a thinner electrode between the bilayer constituents.

The YIG-PZT bilayer phase shifter based on microwave ME effects at FMR has been reported by Tatarenko *et al.*<sup>168</sup> The design of this particular phase shifter is shown in **Figure 29**. The phase shifter consists of a 1 mm wide microstrip on a 1 mm thick back side metallized alumina (relative dielectric constant of 10) ground plane, a YIG-PZT resonator, and microstrip stubs of lengths  $\lambda/8$  and  $3\lambda/8$  that produce a circularly polarized microwave magnetic field within the resonator. The PZT/YIG/GGG trilayer structure is situated on top of the alumina microstrip. The ME resonator consisted of a PZT plate with a thickness of 0.5 mm and an area of  $5 \times 5 \text{ mm}^2$  and an epitaxial (100) YIG film with a thickness of 124  $\mu\text{m}$  and an area of  $4 \times 2.5 \text{ mm}^2$  on a 0.5 mm thick gadolinium gallium garnet (GGG) substrate. The bonding between YIG film and PZT was accomplished with a 0.08 mm thick layer of ethyl cyanoacrylate which is a fast-dry epoxy. This YIG-PZT phase shifter is based on microwave ME effects at FMR. The piezoelectric deformation of PZT by application of an electric field,  $E$ , manifests itself as a magnetic field shift in the FMR profile for YIG causing a shift in the phase for the propagating microwave field. When  $E = 5\text{--}8 \text{ kV/cm}$  was applied across PZT, corresponding phase shifts of  $\Delta\phi = 90^\circ\text{--}180^\circ$  were demonstrated. The  $\Delta\phi$  vs.  $E$  characteristics was linear or nonlinear depending on the applied magnetic field or frequency. **Figure 30** shows the phase characteristics for  $H_0 = 2720 \text{ Oe}$  bias field, where the variation of the real part of the permeability,  $\mu'$ , with  $H$  is linear. The frequency shift  $\Delta\phi$  was 2 MHz for  $E = 5 \text{ kV/cm}$ , and it varied linearly with  $E$ . Similar phase shift characteristics were measured at 5 GHz. The insertion loss varied from a minimum of 1.5 – 2 dB at 5 GHz to a maximum of 3 – 4 dB at 9.6 GHz.

An electric field tunable microwave bandpass filter based on ferromagnetic resonance in a YIG/PZT bilayer has been suggested.<sup>182</sup> In this filter approach the tunability is achieved through magnetoelectric coupling which manifests itself as a shift in ferromagnetic resonance. The ME effect induced FMR field shift would then facilitate rapid electric field tuning with near-zero power consumption (if the piezoelectric material is of high resistivity), reduced noise, and compatibility with integrated circuit technology. A 125 MHz tuning range for  $E = 0 - 3$  kV/cm and an insertion loss of 5 dB at 6.5 GHz have been demonstrated. The quest for narrow band tunable filters with very low loss has paved the way for the development of ferrite tuned high-temperature superconducting filters as well.<sup>183</sup> However, the ferrite loss at low temperatures must be reduced significantly in order to use this effect for practical applications.

In microwave devices composed of ferroelectric and ferrite layers electric tunability can alternatively be achieved by changing the dielectric constant of the ferroelectric constituent by applying an electric field rather than using the magnetoelectric coupling that is based on changing the magnetization or the internal magnetic field of the ferrite component through magnetostriction. Such dielectric tuning has been clearly demonstrated in resonators phase shifters containing YIG and BaSrTiO<sub>3</sub> (BST) bilayers.<sup>165,166,184,185</sup>

To achieve wide-band electrical tuning optimization of in-plane dimensions of the bilayer structures is required, for which theories of spin wave dispersion in layered films have been developed.<sup>186</sup> What is referred to as “spin waves” are the magnetic waves that have

wavelengths greater than the lattice parameter and propagate to distances much larger than their wavelength. In the case of layered ferromagnetic/ferroelectric structures a full electrodynamic theory of hybrid electromagnetic spin waves taking into account the dipole-dipole and exchange interactions should be used to derive the spin wave dispersion.<sup>186</sup> The theoretical model can however be simplified significantly if the phase velocity of pure electromagnetic waves in ferromagnetic films is assumed to be much higher than that of spin waves,<sup>187</sup> which may not really be valid in the case of layered structures involving ferroelectrics with high dielectric constants ( $\sim 10^3$ ).<sup>186</sup> The dispersion relations in layered structures containing a ferromagnetic layer and dielectric layers with high dielectric constants have found to exhibit strong hybridization between the spin and electromagnetic waves.<sup>186</sup> The geometry of the layered structure, the direction of bias magnetization, and the respective wave propagation direction are all effective on the level of hybridization, which was estimated to be stronger for hybrid surface waves propagating in tangentially magnetized nonsymmetrical layered structures. The dispersion and therefore the hybridization can be varied by electrically tuning the dielectric constant of the ferroelectric layer or/and the strain through the piezoelectric effect, providing the possibility for dual (electrically and magnetically) tunable microwave devices.

When only the dipole-dipole interaction in the spin-wave system is taken into account and the exchange interactions are excluded, the waves are called dipolar spin waves (or magnetostatic waves). The dispersion of the magnetostatic waves for the lowest index

thickness mode, which is the only mode excited for exchange boundary conditions of unpinned surface spins, can be written as<sup>166,187</sup>

$$\omega^2(kL) = \left[ \gamma H + \gamma 4\pi M_s \frac{1}{kL} (1 - e^{-kL}) \right] \left[ \gamma H + \gamma 4\pi M_s \left( 1 - \frac{1}{kL} (1 - e^{-kL}) \right) \sin^2 \varphi \right]$$

**Equation 55**

where  $\omega$  is the frequency,  $k$  is the in-plane wave number,  $H$  is the in-plane internal bias field,  $4\pi M_s$  is the saturation magnetization ( $\sim 1750$  Oe for YIG),  $\gamma$  is the gyromagnetic ratio,  $L$  is the film thickness, and  $\varphi$  is the angle between the spin wave propagation and the bias field  $\mathbf{H}$ . For a resonator having a small aspect ratio (thickness to lateral size) a strong pinning of the magnetization at the lateral edges can be assumed leading to quantized values of the wavenumber for the discrete resonator eigenmodes

$$k_{qr} = \pi \sqrt{\left(\frac{q}{a}\right)^2 + \left(\frac{r}{b}\right)^2}$$

**Equation 56**

where  $q$  and  $r$  are integers and  $a$  and  $b$  are the lateral (in-plane) dimensions of the resonator. Angle  $\varphi$  in Equation 55 satisfies

$$\sin^2 \varphi = \left( \frac{1}{k_{qr}} \frac{q}{a} \right)^2$$

**Equation 57**

Using Equation 55, Equation 56, and Equation 57 discrete frequencies of eigenmodes for the bilayer resonator structures can be obtained for spin waves propagating in-plane of

the bilayer when the internal magnetic field is in plane. Similar equations can be obtained for arbitrary directions of propagation and magnetic fields.<sup>187</sup>

The theoretical estimates have been shown to agree well with the experimental results on YIG/BST resonator structures.<sup>166</sup> A 8  $\mu\text{m}$ -thick single crystal YIG layer grown on a (111)-oriented GGG substrate having in plane dimensions of 1 mm and 1.5 mm was attached to a 300  $\mu\text{m}$ -thick BST ferroelectric slab coated with metal films on both sides. A microstrip line of 0.5 mm width was fabricated on the back surface of the GGG substrate and used to excite the resonator. The resonance frequencies in these YIG/BST resonators ( $\sim 5.26$  GHz) having a bandwidth of 3.5 MHz could be tuned electrically in a range of 8 MHz using voltages up to 1000 V applied to the ferroelectric BST layer. By optimizing the in-plane dimensions of both the YIG and BST layers to excite the hybridized wave mode with a wave number that would allow strong coupling between the YIG and BST resonators, electrical tuning was significantly improved.<sup>184</sup> A 500  $\mu\text{m}$ -thick ceramic BST slab and a 7  $\mu\text{m}$ -thick YIG (111) of in plane dimensions  $3 \times 5 \text{ mm}^2$  and  $0.5 \times 1.5 \text{ mm}^2$ , respectively, were attached together with a 50 nm-thick Cr electrode on the BST surface in contact with the YIG resonator. At an electric field of 18 kV/cm applied across the BST slab the resonance frequency of the coupled resonator structure was observed to shift by 54 MHz (1.5 % of the central resonant frequency, 3.64 GHz).<sup>184</sup>

The resonator hybrid modes observed for the BaM/PZT bilayers<sup>106</sup> discussed in [Section 2.2.2](#) (results shown in [Figure 7](#)) have also been shown to agree well with the discrete wavenumbers described in [Equation 56](#). The reflected power as a function of the

frequency measured under  $H_0 = 5980$  Oe for a BaM/PZT bilayer consisting a 185  $\mu\text{m}$ -thick single crystal BaM slab (4.8 mm x 2.4 mm in-plane dimensions) is shown in **Figure 31**. The peaks labeled 1 through 4 were found to correspond to  $(q,r)$  modes of (1,1), (3,1), (1,3), and (5,1), respectively.

When compared to the YIG/PZT bilayer phase shifters discussed above<sup>168</sup> a much higher differential phase shift has been demonstrated<sup>165</sup> in a dual (electric and magnetic field) tunable microwave phase shifter fabricated using BST as the ferroelectric material. Using a bilayer consisting a single-crystal YIG film (5  $\mu\text{m}$  on GGG) and a ceramic BST slab (500  $\mu\text{m}$ ) an electrical tunability of the differential phase shift  $\Delta\phi$  as high as  $650^\circ$  was achieved in a frequency range of 4.5–8 GHz through tuning of the dielectric constant of BST by applying an electric field of up to 20 kV/cm across the BST slab.

## 4. Summary and Outlook

Frequency tuning by external magnetic fields is not as attractive as electrical tuning which can be achieved if the magnetic property of the material is sensitive to the field through magnetoelectric (ME) coupling. In the so-called multiferroic materials such as  $\text{TbMnO}_3$ ,  $\text{TbMn}_2\text{O}_5$ ,  $\text{BiFeO}_3$ ,  $\text{Cr}_2\text{O}_3$ , and  $\text{BiMnO}_3$ , which possess simultaneously both the ferroelectric and ferromagnetic properties, ME coupling can be obtained. However, this coupling is very small to be practical since the ligand-field hybridization of a transition metal cation by its surrounding anions, which is often responsible for conventional ferroelectricity, requires that the  $d$  orbitals of the cations be unoccupied, thus precluding ferromagnetism. Besides, the relevant phase transitions, below which magnetoelectric

behavior observed, are often well below room temperature. What is most attractive, however, is the use bilayer structures, one constituent of which is highly piezoelectric and the other ferromagnetic. In such a structure, the electric field applied across the piezoelectric material transmits the resulting strain to the magnetic material mechanically. The transmitted mechanical strain then, through the magnetostriction coefficient, causes a change in the magnetic permeability which forms the basis for electrical tuning. These hybrid structures can be implemented in the form of either "multilayers" consisting of alternating layers of the ferroelectric phase and the ferro/ferrimagnetic phase or heterostructures consisting of nanostructure of the ferro/ferrimagnetic phase embedded in a ferroelectric matrix.

Also important is the miniaturization that can be obtained in passive components owing to large magnetic susceptibility afforded by many of these ferromagnetic materials. As discussed, particularly in the antenna section, this is very important in applications using the lower end of the rf spectrum where the air wavelength is very long. Similar benefits also accrue as a result of large dielectric constants that accompany these materials. Furthermore, the dielectric constant can also be tuned with electric field in sister materials, such as some perovskites, again aiding in achieving tunability with small voltage variations.

One caveat is that in multilayers grown epitaxially, the ME coupling effect is weakened due to the clamping effect of the substrate unless they are free standing membranes. When accomplished, electrical tuning coupled with high dielectric permittivity and



magnetic susceptibility could lead to miniature microwave components and/or make operation at very high frequencies possible without the need for increased size and weight common in conventional approaches. Tunable and frequency agile antennas would pave the way for multiband operation as well as portable phased array antennas with far reaching consequences.

## 5. Acknowledgments

The research at VCU is made possible by funds from the Office of Naval Research under direction of the program monitor, Dr. Ingham Mack and his predecessor, Dr. C. E. C. Wood. The authors would like to thank Professors Y.-K. Hong, J.-G. Yoon, C. Vittoria, and C. M. Srinivasan, and Dr. Cole Litton for useful discussions and in some cases manuscript and sample exchange, and graduate student E. Rowe for proofreading the manuscript.

## FIGURE CAPTIONS

**Figure 1:** (a) Schematic illustrations of a multilayer structure with alternating layers of piezoelectric and ferro/ferromagnetic phases on a substrate, and (b) of a self-assembled nanostructured thin film of the ferro/ferromagnetic phase embedded in a ferroelectric matrix on a substrate.

**Figure 2:** The coordinate system for a free body composed of a magnetostrictive and a piezoelectric layer. To measure the transverse and the longitudinal ME coefficients, the applied magnetic field should be in the sample plane and normal to the sample plane, respectively.

**Figure 3:** Transverse magnetoelectric voltage coefficient at 120 and 300 K as a function of static magnetic field  $H$  for a two-layer structure consisting of 200  $\mu\text{m}$  films of LSMO and PZT. The bias field  $H$  and a 100 Hz AC magnetic field  $\delta H_x$  are applied parallel to each other and parallel to the sample plane, and the induced electric field is measured perpendicular to the sample plane. The open (filled) circles are the data points for increasing (decreasing)  $H$ . The lines are guides to the eye. (After Srinivasan *et al.*<sup>17</sup>)

**Figure 4:** Diagram showing a microstripline resonator with a bilayer of lead zirconate titanate (PZT) bonded to (111) yttrium iron garnet (YIG) film on gadolinium gallium garnet (GGG) substrate. (After Fetisov and Srinivasan.<sup>77</sup>)

**Figure 5:** (a)  $S_{11}$  reflection parameter as a function of frequency for electric fields of 0 and  $\pm 10$  kV/cm with a bias magnetic field of 1.12 kOe parallel to the bilayer plane. The absorption peaks correspond to the FMR in YIG. (b) Electrical tuning of the YIG-PZT

resonator at 5 GHz for  $H$  parallel and perpendicular to the bilayer plane. (After Fetisov and Srinivasan.<sup>77</sup>)

**Figure 6:** Measured field shift at  $E=8$  kV/cm as a function of YIG-to-PMN-PT volume ratio for in-plane and out-of plane  $H$ . The lines are guides to the eye. (After Shastri *et al.*<sup>76</sup>)

**Figure 7:** (a) Microwave absorption as a function of frequency  $f$  under a static magnetic field of  $H_0 = 5980$  Oe for different values of electric field  $E$  applied across polycrystalline PZT plate bonded to 185  $\mu\text{m}$ -thick single crystal BaM. (b) Electric field induced shift in the FMR frequency for a BaM/PZT bilayer with 95  $\mu\text{m}$ -thick single crystal BaM under  $H_0 = 6020$  Oe. (After Srinivasan *et al.*<sup>106</sup>)

**Figure 8:** ME voltage vs. static magnetic field measured with a transverse geometry at three different temperatures of 50, 120, and 300 K. The open (filled) symbols are the data taken with increasing (decreasing)  $H$ . The largest peak-to-peak ME voltage swing is  $\sim 28$   $\mu\text{V}$ , occurring at 120 K. The inset is the in-plane lattice contraction as a function of  $H$  measured at selected temperatures, taken from Ref. 188. (After Wu *et al.*<sup>56</sup>).

**Figure 9:** Magnetization of a 50 nm-thick  $\text{La}_{0.67}\text{Sr}_{0.33}\text{MnO}_3$  films grown on a (001)  $\text{BaTiO}_3$  substrate as a function of the temperature. The magnetic field is applied along the [100] direction. The inset shows the hysteresis loops at temperatures below ( $T_1$ ) and above ( $T_2$ ) the tetragonal to monoclinic phase transition temperature (278 K). (After Li *et al.*<sup>109</sup>)

**Figure 10:** Longitudinal ME voltage coefficient as a function of the AC magnetic field frequency for a multilayer containing of 11 layers of 13  $\mu\text{m}$ -thick  $\text{NiFe}_2\text{O}_4$  and 10 layers of 26  $\mu\text{m}$ -thick PZT. The solid line represents the theoretical calculations. The inset shows the impedance for a 10-mm disk of PZT as a function of the frequency. (After Bichurin *et al.*<sup>70</sup>)

**Figure 11:** The coordinate system for a bilayer free body composed of plate-like magnetostrictive and piezoelectric layers.

**Figure 12:** Frequency dependences of the ME voltage coefficient for Permendur-PZT bilayer structures with a coupling coefficient  $\beta$  of (a) 1.0 and (b) 0.4. (After Filippov.<sup>112</sup>)

**Figure 13:** (a) TEM planar view image showing  $\text{CoFe}_2\text{O}_4$  nanopillars embedded in the  $\text{BaTiO}_3$  matrix. (b) Magnetization as a function of the temperature measured at  $H=100$  Oe. The top curve shows the data for the self assembled nanostructure, while the bottom curve is for the multilayered laminated nanostructure showing negligible change in magnetization. (After Zheng *et al.*<sup>117</sup>)

**Figure 14:** Schematic diagram of a phased-array antenna module where HPA depicts high power amplifier, and LNA low noise amplifier. After Adam *et al.*<sup>121</sup>

**Figure 15:** A nonreciprocal Faraday rotation phase shifter.

**Figure 16:** Reggia-Spencer reciprocal phase shifter.

**Figure 17:** Schematic diagram (a) and photograph (b) of a fabricated ferrite circulator.  
(Courtesy of J. Young and Y.- K. Hong)

**Figure 18:** Coupling structure for a single-stage YIG sphere filter. (After Carter.<sup>137</sup>)

**Figure 19:** A schematic of a resonance isolator.

**Figure 20:** (a) Nonreciprocal attenuator. (b) The magnetization of the ferrite cylinder is achieved by passing a current (I) through its central axis. (After Enander.<sup>143</sup>)

**Figure 21:** A sample junction ferrite microwave isolator.

**Figure 22:** Different types of microstrip antennas: (a) rectangular microstrip patch antenna, (b) circular microstrip patch antenna, (c) open-circuit microstrip radiator, (d) microstrip dipole antenna. (After Carver and Mink.<sup>146</sup>)

**Figure 23:** Efficiency and bandwidth of a microstrip antenna versus substrate thickness normalized to wavelength. (After Pozar.<sup>144</sup>)

**Figure 24:** Geometry of a microstrip antenna with an in-plane biased ferrite cover layer.  
(After Yang.<sup>152</sup>)

**Figure 25:** Configuration of the variable polarization ferrite antenna. (After Dunn *et al.*<sup>162</sup>)

**Figure 26:** A delay line based on a YIG/PMN-PT bilayer. (After Fetisov and Srinivasan.<sup>125</sup>)

**Figure 27:** Frequency responses of the stand-alone YIG sample (dash curve), YIG/PMN-PT resonator (solid curve), and YIG sample with a rectangular copper piece on top (dash-dot curve). (After Ustinov *et al.*<sup>178</sup>)

**Figure 28:** FMR frequency spectra for the YIG/PMN-PT resonator measured at various electric fields for  $H = 1012$  Oe applied parallel to the resonator plane. (After Ustinov *et al.*<sup>178</sup>)

**Figure 29:** Schematics of a magnetoelectric (ME) nonreciprocal microwave phase shifter showing a ME resonator of yttrium iron garnet (YIG) film on gadolinium gallium garnet (GGG) substrate bonded to lead zirconate titanate (PZT), and microstrip transducers and stubs. (After Tatarenko *et al.*<sup>168</sup>)

**Figure 30:** The phase angle  $\phi$  vs. frequency  $f$  characteristics at 9.6 GHz for  $E = 0$  and 5 kV/cm. The applied bias field is  $H_0 = 2720$  Oe, which corresponds to a region in which the variation of the real part of the permeability  $\mu'$  with the magnetic field is linear. (After Tatarenko *et al.*<sup>168</sup>)

**Figure 31:** Reflected power as a function of the frequency for a BaM/PZT bilayer with a 185  $\mu\text{m}$ -thick ferrite under a static magnetic field of 5980 Oe applied along the c-axis of BaM. (After Srinivasan *et al.*<sup>106</sup>)

## TABLES

**Table 1:** Room temperature saturation magnetostriction values for some magnetostrictive materials.<sup>11</sup>

Material	Saturation magnetostriction $\lambda_s^{(MS)}$ ( $10^{-6}$ )
Fe	-7
Fe-3.2% Si	9
Ni	-33
Ni – 4 wt % Co	-31
Permalloy, 45 % Ni- 55 % Fe	27
Permalloy, 82 % Ni – 18 % Fe	0
Alfer, 87 % Fe – 13 % Al	30
Fe <sub>80</sub> B <sub>20</sub>	30
Fe <sub>66</sub> Co <sub>18</sub> B <sub>15</sub> Si <sub>1</sub> – amorphous	35
NiFe <sub>2</sub> O <sub>4</sub>	-33
Ni <sub>0.98</sub> Co <sub>0.02</sub> Fe <sub>2</sub> O <sub>4</sub>	-32
Fe <sub>3</sub> O <sub>4</sub>	40
Permendur, 49 % Co - 49 % Fe – 2 % V	70
CoFe <sub>2</sub> O <sub>4</sub>	-110
Co <sub>1.1</sub> Fe <sub>1.9</sub> O <sub>4</sub>	-250
SmFe <sub>2</sub>	-1560
TbFe <sub>2</sub>	1753
Terfenol D, Tb <sub>0.3</sub> Dy <sub>0.7</sub> Fe <sub>1.93</sub>	2000
DyZn [001] at 4.2K	5300
Y <sub>3</sub> Fe <sub>5</sub> O <sub>12</sub>	1.1
BaFe <sub>12</sub> O <sub>19</sub>	15

**Table 2:** Parameters for the constituents necessary to calculate the ME effect in  $\text{CoFe}_2\text{O}_4$  /  $\text{BaTiO}_3$  and  $\text{CoFe}_2\text{O}_4$  / PZT bilayer structures.<sup>12</sup>

Parameter	$\text{CoFe}_2\text{O}_4$	$\text{BaTiO}_3$	PZT-4
${}^m q_{zx}$ [ $10^{-12}$ m/A]	556	-	-
${}^m q_{zz}$ [ $10^{-12}$ m/A]	1880	-	-
${}^p d_{zx}$ [ $10^{-12}$ C/N]	-	-78	-123
${}^p d_{zz}$ [ $10^{-12}$ C/N]	-	190	289
$s_{xx}$ [ $10^{-12}$ m <sup>2</sup> /N]	6.48	7.25	12.3
$s_{xy}$ [ $10^{-12}$ m <sup>2</sup> /N]	-2.37	-3.15	-4.05
$\varepsilon_{zz}^T / \varepsilon_0$	10	1345	1300



**Table 3:** ME voltage coefficients in mV/cm-Oe units for CoFe<sub>2</sub>O<sub>4</sub> / BaTiO<sub>3</sub> and CoFe<sub>2</sub>O<sub>4</sub> / PZT bilayer structures calculated for different values of volume fractions of the magnetostrictive ( ${}^mV$ ) and the piezoelectric ( ${}^pV$ ) phases.  $(\alpha_E^*)_{zz}$  is the ME voltage coefficient per unit thickness of the piezoelectric phase, obtained by multiplying  $(\alpha_E)_{zz}$  with the volume fraction  ${}^pV$ .<sup>12</sup>

${}^mV$	${}^pV$	$(\alpha_E)_{zz}$	$(\alpha_E^*)_{zz}$
CoFe <sub>2</sub> O <sub>4</sub> on BaTiO <sub>3</sub>			
0.10	0.90	146	132
0.50	0.50	818	409
0.90	0.10	1662	166
CoFe <sub>2</sub> O <sub>4</sub> on PZT-4			
0.10	0.90	226	204
0.50	0.50	990	495
0.90	0.10	1585	158

**Table 4:** Magnetoelectric coupling coefficients measured for various multiferroic single phase materials.

Material	ME coefficient		Ref.
	$\alpha_M = \mu_0 \delta M / \delta E$ (ps/m)*	$\alpha_E = \delta E / \delta H$ (mV/cm-Oe)**	
Cr <sub>2</sub> O <sub>3</sub>	4.13 (at 295 K)		19, 23
TbMn <sub>2</sub> O <sub>5</sub>	21 (at 28 K)		36
LiCoPO <sub>4</sub>	30.6 (at 4.2 K)		45
LiNiPO <sub>4</sub>	1.7 (at 20 K)		28
(YBiLaPr) <sub>3</sub> (FeGa) <sub>5</sub> O <sub>12</sub>	30 (at 294 K)		46
TbPO <sub>4</sub>	36.7 (at 1.9 K)		47
BiFeO <sub>3</sub>		0.3 (at 20 K)	49,50
La <sub>0.7</sub> Sr <sub>0.3</sub> MnO <sub>3</sub> /PMN-PT (001) bilayer	60000 (at 300 K)		72

\* To convert from the SI ps/m units to cgs Gauss-cm/V units the magnetic ME coefficient  $\alpha_M$  should be divided by  $4\pi\epsilon_0\epsilon_r$ , where  $\epsilon_r$  is the relative permittivity of the material.

\*\* To convert from the cgs mV/cm-Oe units to SI (V/m)/(A/m) units, the electrical ME coefficient  $\alpha_E$  should be divided by  $10^4/4\pi$ .

**Table 5:** ME voltage coefficients for some two-phase systems. The measurements were performed at room temperature unless indicated. The frequency values in parentheses next to the ME voltage coefficients indicate the electromechanical resonance frequencies at which these coefficients are measured.

Ferroelectric constituent	Magnetostrictive constituent	Type	$\alpha_E = \frac{\partial E}{\partial H}$ (mV/cm-Oe)	Reference
Pb(Zr <sub>1-x</sub> Ti <sub>x</sub> )O <sub>3</sub> (PZT)	Tb <sub>1-x</sub> Dy <sub>x</sub> Fe <sub>2-y</sub> (Terfenol-D) / $\mu$ -metal (high-permeability Ni-Fe alloys)	laminated composites	~3500	Ref. 52, trilayer with Terfenol-D on both sides of PZT
PMN-PT single crystal	Terfenol-D	laminated composites	~2460 (~30800 at 78 kHz)	Ref. 53
BaTiO <sub>3</sub> (BTO)	CoFe <sub>2</sub> O <sub>4</sub>	composites	1.48	Ref. 54
PMN-PT single crystal	Tb <sub>40</sub> Fe <sub>60</sub> /Fe <sub>50</sub> Co <sub>50</sub>	magnetostrictive layer sputtered	24	Ref. 55
Pb(Zr <sub>0.3</sub> Ti <sub>0.7</sub> )O <sub>3</sub>	La <sub>1.2</sub> Sr <sub>1.8</sub> Mn <sub>2</sub> O <sub>7</sub> melt-grown single crystal	Epitaxial PZT, sol-gel	~750	Ref. 56, 120 K LSMO Ruddlesden-Popper phase
PZT	NiFe <sub>2</sub> O <sub>4</sub>	laminated composites	1500	Ref. 57, Multilayers
PZT	Ni <sub>0.8</sub> Zn <sub>0.2</sub> Fe <sub>2</sub> O <sub>3</sub>	bonded composites	430	Ref. 58, Trilayer with ferrite on both sides of the PZT
PZT	La <sub>0.7</sub> Sr <sub>0.3</sub> MnO <sub>3</sub>	laminated composites	32	Ref. 17
PZT	La <sub>0.7</sub> Ca <sub>0.3</sub> MnO <sub>3</sub>	laminated composites	3	Ref. 17
PZT	Permendur (Co-Fe-V alloy)	bonded composites	640 (85000 at ~ 330 kHz)	Ref. 59, Trilayer with permendur on both sides of PZT
PZT	Terfenol-D	laminated composites	4680	Ref. 60
Pb(Zr <sub>0.52</sub> Ti <sub>0.48</sub> )O <sub>3</sub>	NiFe <sub>2</sub> O <sub>4</sub>	Epitaxial, PLD, grown on (001) SrTiO <sub>3</sub> :Nb substrates	16	Ref. 61, Ferrite nanoparticles in PZT
PbZr <sub>0.57</sub> Ti <sub>0.43</sub> O <sub>3</sub>	NiFe <sub>2</sub> O <sub>4</sub>	composites	80	Ref. 62
BaTiO <sub>3</sub>	Ni <sub>0.94</sub> Co <sub>0.01</sub> Cu <sub>0.05</sub> Fe <sub>2</sub> O <sub>4</sub>	composites	0.64	Ref. 63
PbZr <sub>0.52</sub> Ti <sub>0.48</sub> O <sub>3</sub>	CoFe <sub>2</sub> O <sub>4</sub>	laminated composites	163	Ref. 64, PZT on both sides of CoFe <sub>2</sub> O <sub>4</sub>
(Bi <sub>1/2</sub> Na <sub>1/2</sub> )TiO <sub>3</sub> - (Bi <sub>1/2</sub> K <sub>1/2</sub> )TiO <sub>3</sub> - BaTiO <sub>3</sub>	Terfenol-D	laminated composites	407	Ref. 65, Terfenol disks on both sides of ferroelectric
PZT-5	Terfenol-D	laminated composites	1100	Ref. 66
Pb(Zr <sub>0.52</sub> Ti <sub>0.48</sub> )O <sub>3</sub>	Terfenol-D	composites	8700 (at 59.2 kHz)	Ref. 67
Pb(Zr <sub>0.52</sub> Ti <sub>0.48</sub> )O <sub>3</sub>	NiFe <sub>2</sub> O <sub>4</sub>	composites	6700 (at 132.6 kHz)	Ref. 68
PZT	Terfenol-D	laminated composites	10960 (at 20.03 kHz)	Ref. 69, Trilayer with Terfenol-D on both sides of PZT
PZT	NiFe <sub>2</sub> O <sub>4</sub>	composites	1200 (at 350 kHz)	Ref. 70, Multilayers
PZT	Ni <sub>0.8</sub> Zn <sub>0.2</sub> Fe <sub>2</sub> O <sub>3</sub>	composites	4200 (at 308.5 kHz)	Ref. 71

**Table 6:** ME coupling coefficients obtained from the ferromagnetic resonance frequency shifts achieved by electrical field tuning in piezoelectric/ferromagnetic bilayers.  $\gamma = 2\pi \times 2.8$  MHz/Oe is the gyromagnetic ratio.

Sample	Applied field (kV/cm)	$\alpha_f = \frac{\delta H}{\delta E}$ (Oe-cm/kV)	$\frac{\delta f}{\delta E} = \frac{\gamma}{2\pi} \frac{\delta H}{\delta E}$ (MHz-cm/kV)	Reference
YIG (111) (15 $\mu\text{m}$ on GGG) - ceramic PZT (500 $\mu\text{m}$ )	10	0.88	2.5	77
Laminated/sintered multilayers of $\text{Li}_{0.5}\text{Fe}_{2.5}\text{O}_4$ (15 $\mu\text{m}$ ) – PZT (15 $\mu\text{m}$ )	80	0.25	0.7	104
YIG (111) (4.9 $\mu\text{m}$ on GGG)- PMN-PT (001) (500 $\mu\text{m}$ )	8	5.4	15.1	76
YIG (111) (7.5 $\mu\text{m}$ on GGG) PMN-PT (001) (500 $\mu\text{m}$ )	8	1.95	5.63	178
$\text{BaFe}_{12}\text{O}_{19}$ (BaM) (185 $\mu\text{m}$ single crystal) - ceramic PZT	10	0.29	0.8	106

Ü. Özgür *et al.*

Journal of Materials Science: Materials in Electronics

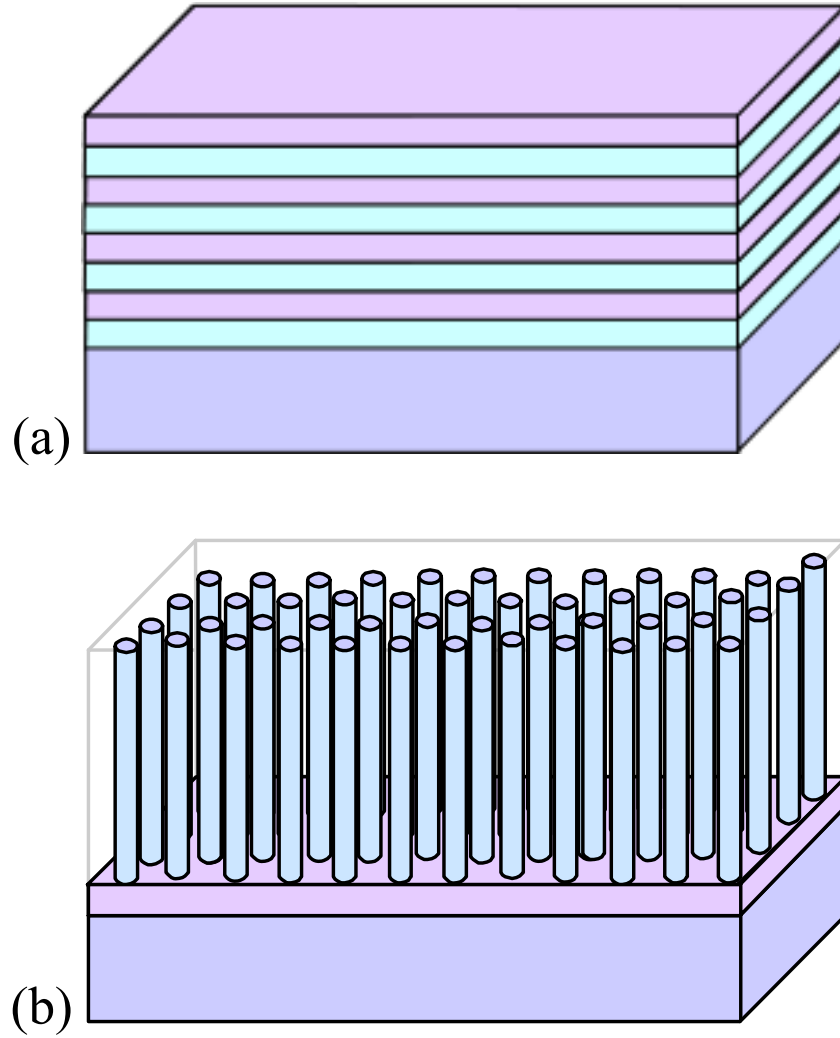


**Figure 32**

Schematic illustrations of a multilayer structure with alternating layers of piezoelectric and ferro/ferromagnetic phases on a substrate, and (b) of a self-assembled nanostructured thin film of the ferro/ferromagnetic phase embedded in a ferroelectric matrix on a substrate.

Ü. Özgür *et al.*

Journal of Materials Science: Materials in Electronics

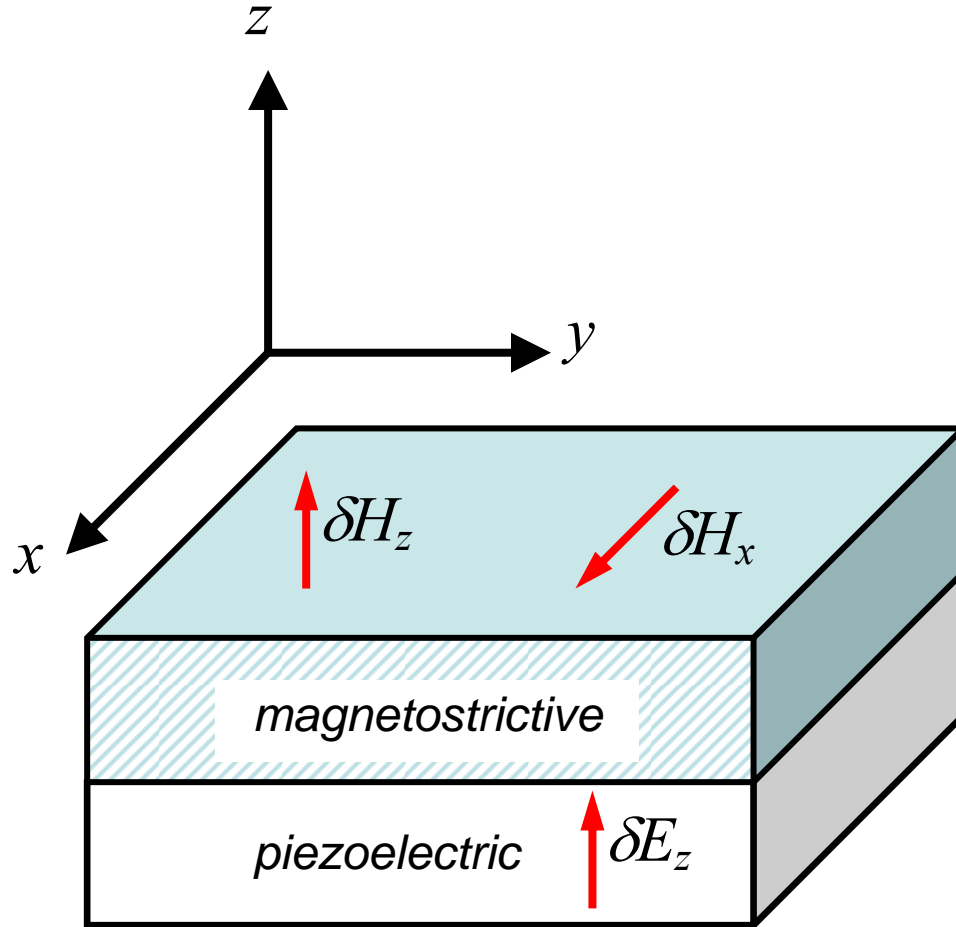


**Figure 33**

The coordinate system for a free body composed of a magnetostrictive and a piezoelectric layer. To measure the transverse and the longitudinal ME coefficients, the applied magnetic field should be in the sample plane and normal to the sample plane, respectively.

Ü. Özgür *et al.*

Journal of Materials Science: Materials in Electronics

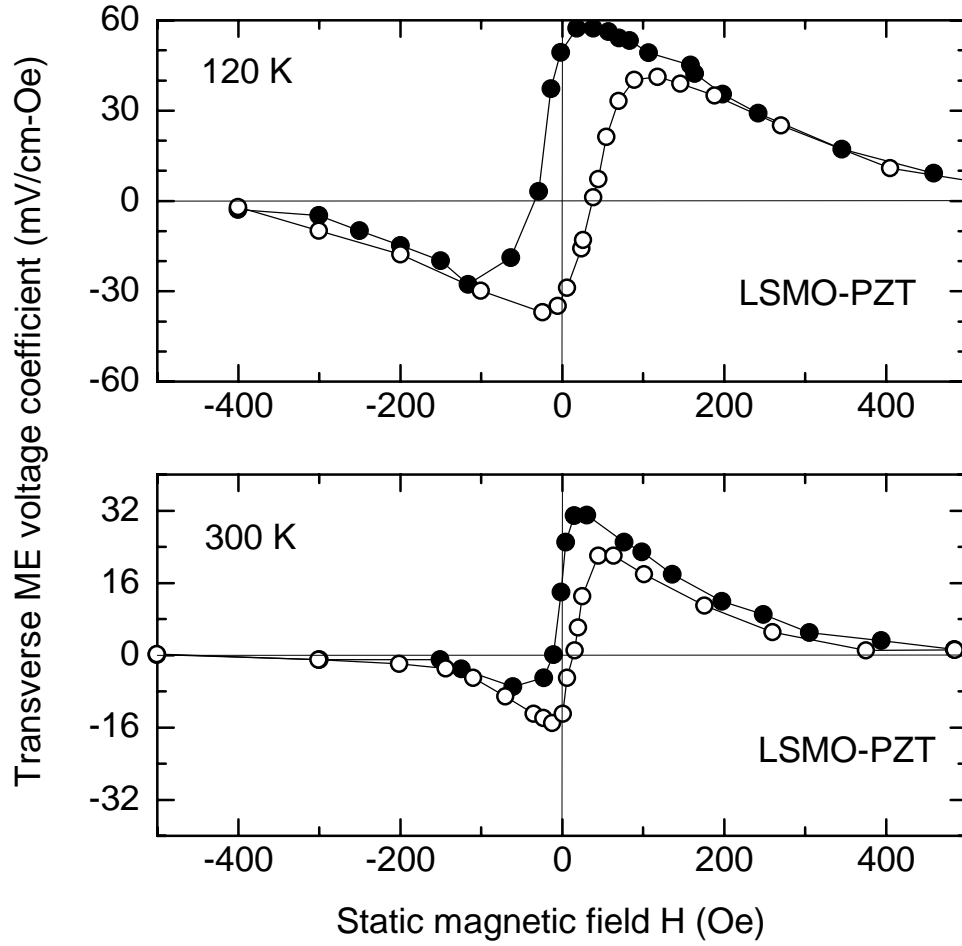


**Figure 34**

Transverse magnetoelectric voltage coefficient at 120 and 300 K as a function of static magnetic field  $H$  for a two-layer structure consisting of 200  $\mu\text{m}$  films of LSMO and PZT. The bias field  $H$  and a 100 Hz AC magnetic field  $\delta H_x$  are applied parallel to each other and parallel to the sample plane, and the induced electric field is measured perpendicular to the sample plane. The open (filled) circles are the data points for increasing (decreasing)  $H$ . The lines are guides to the eye. (After Srinivasan *et al.*)



Ü. Özgür *et al.*

Journal of Materials Science: Materials in Electronics

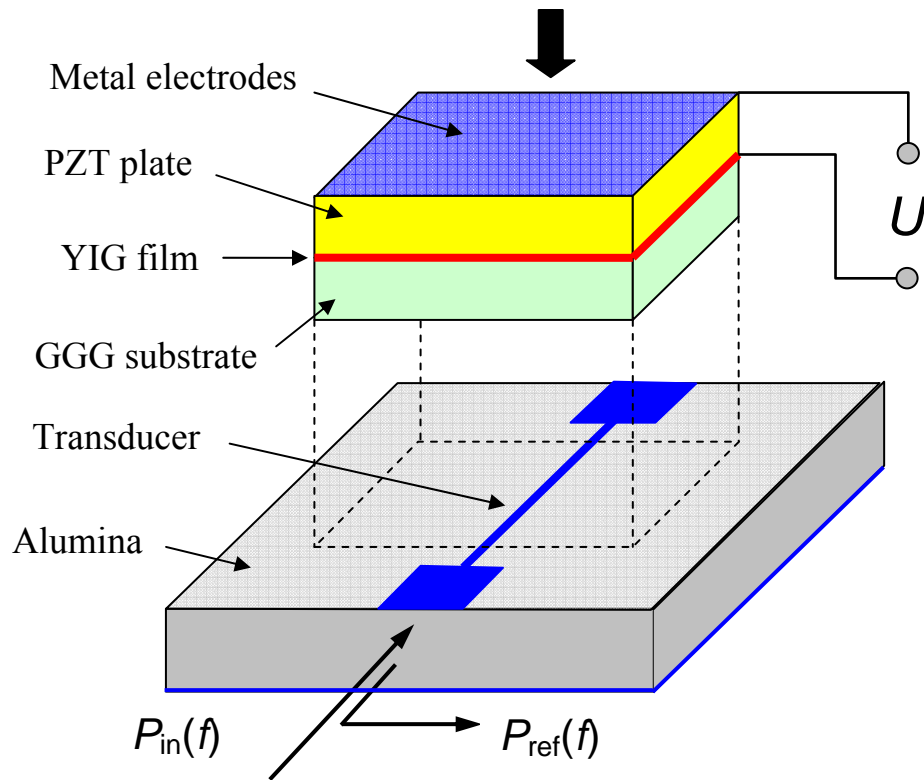


**Figure 35**

Diagram showing a microstripline resonator with a bilayer of lead zirconate titanate (PZT) bonded to (111)\_yttrium iron garnet (YIG) film on gadolinium gallium garnet (GGG) substrate. (After Fetisov and Srinivasan)

Ü. Özgür *et al.*

Journal of Materials Science: Materials in Electronics

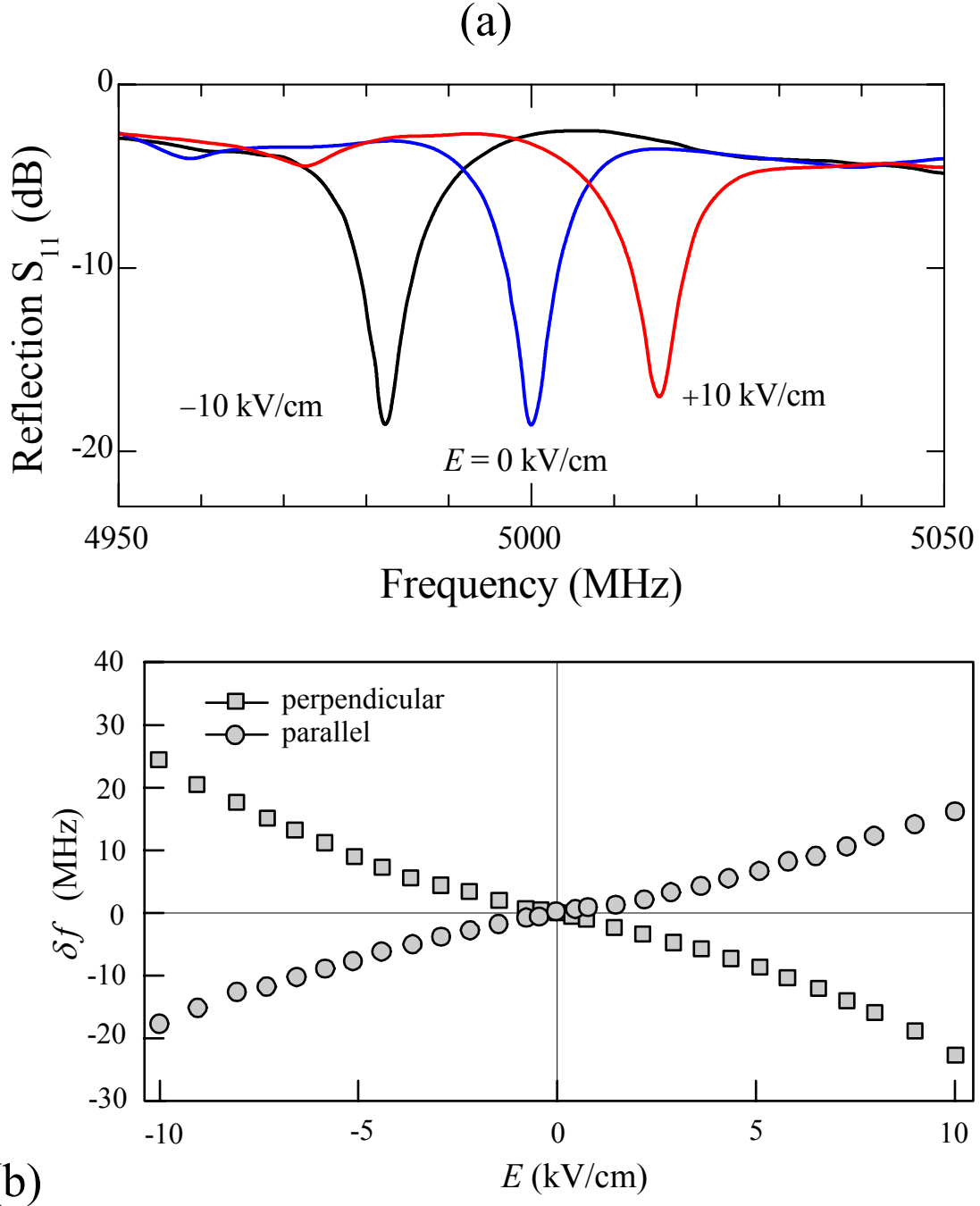


**Figure 36**

(a)  $S_{11}$  reflection parameter as a function of frequency for electric fields of 0 and  $\pm 10$  kV/cm with a bias magnetic field of 1.12 kOe parallel to the bilayer plane. The absorption peaks correspond to the FMR in YIG. (b) Electrical tuning of the YIG-PZT

Özgür *et al.*, submitted to Journal of Materials Science: Materials in Electronics, 2009  
Microwave Ferrites, Part 2: Passive components and electrical tuning

resonator at 5 GHz for  $H$  parallel and perpendicular to the bilayer plane. (After Fetisov and Srinivasan)

Ü. Özgür *et al.*

Journal of Materials Science: Materials in Electronics

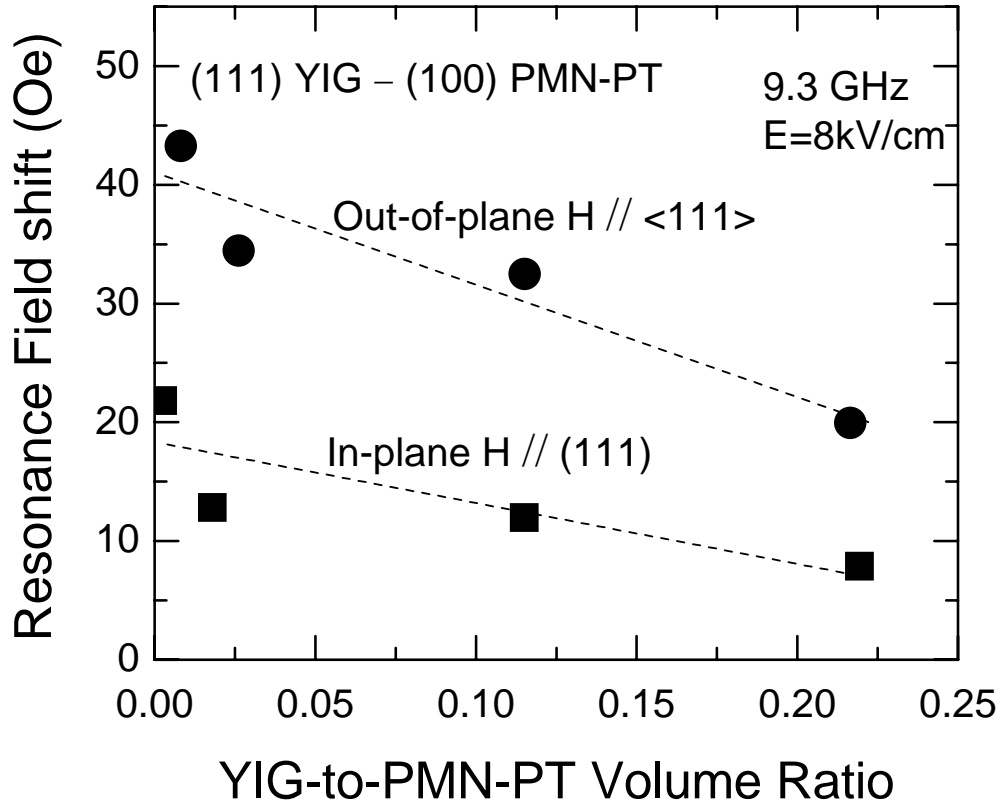
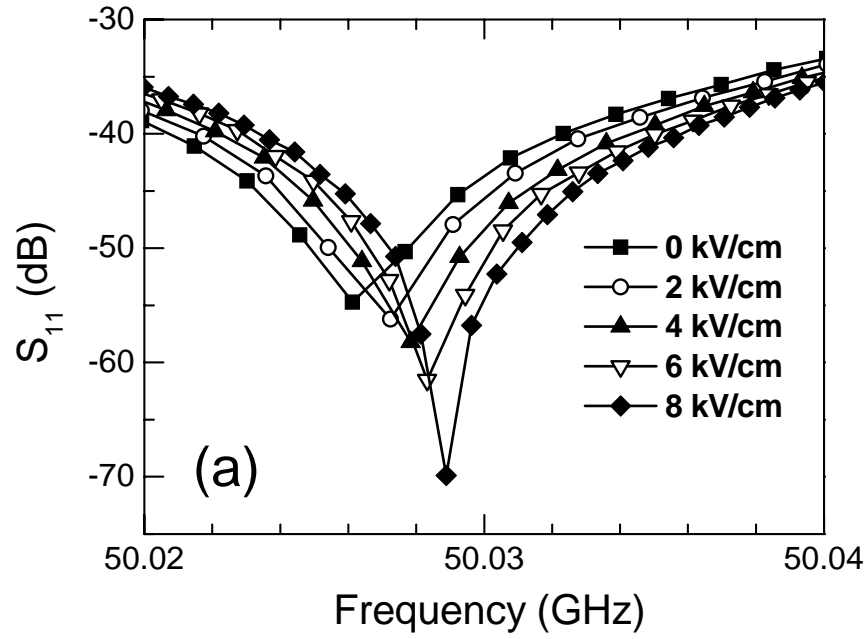


**Figure 37**

Measured field shift at  $E=8$  kV/cm as a function of YIG-to-PMN-PT volume ratio for in-plane and out-of plane  $H$ . The lines are guides to the eye. (After Shastri *et al.*)

Ü. Özgür *et al.*

Journal of Materials Science: Materials in Electronics



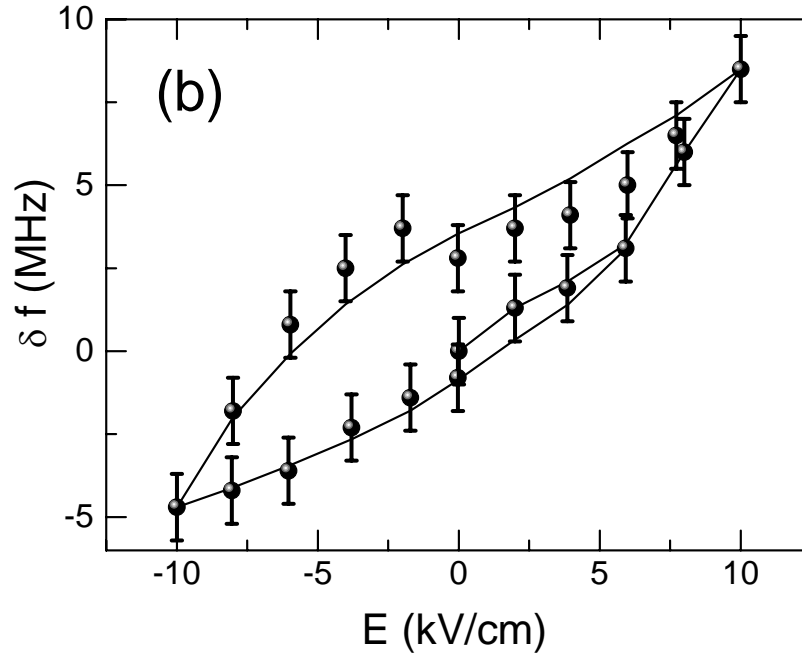


**Figure 38**

(a) Microwave absorption as a function of frequency  $f$  under a static magnetic field of  $H_0 = 5980$  Oe for different values of electric field  $E$  applied across polycrystalline PZT plate bonded to 185  $\mu\text{m}$ -thick single crystal BaM slab. (b) Electric field induced shift in the FMR frequency for a BaM/PZT bilayer with 95  $\mu\text{m}$ -thick single crystal BaM under  $H_0 = 6020$  Oe. (After Srinivasan *et al.*)

Ü. Özgür *et al.*

Journal of Materials Science: Materials in Electronics

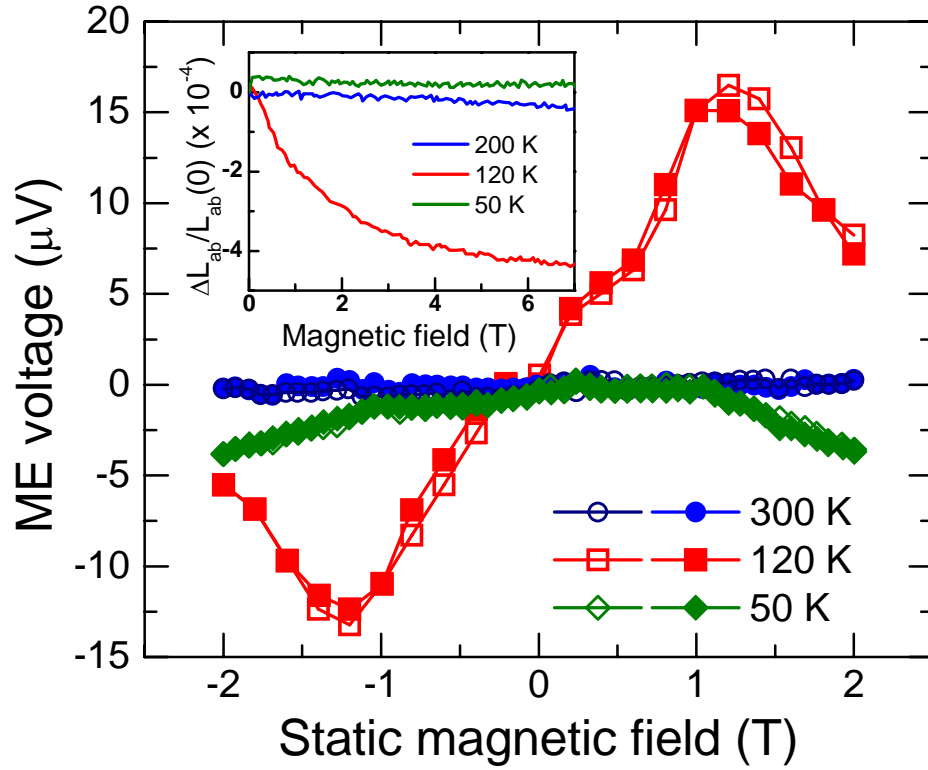


**Figure 39**

ME voltage vs. static magnetic field measured with a transverse geometry at three different temperatures of 50, 120, and 300 K. The open (filled) symbols are the data taken with increasing (decreasing)  $H$ . The largest peak-to-peak ME voltage swing is  $\sim 28 \mu\text{V}$ , occurring at 120 K. The inset is the in-plane lattice contraction as a function of  $H$  measured at selected temperatures, taken from Ref. (After Wu *et al.*)

Ü. Özgür *et al.*

Journal of Materials Science: Materials in Electronics

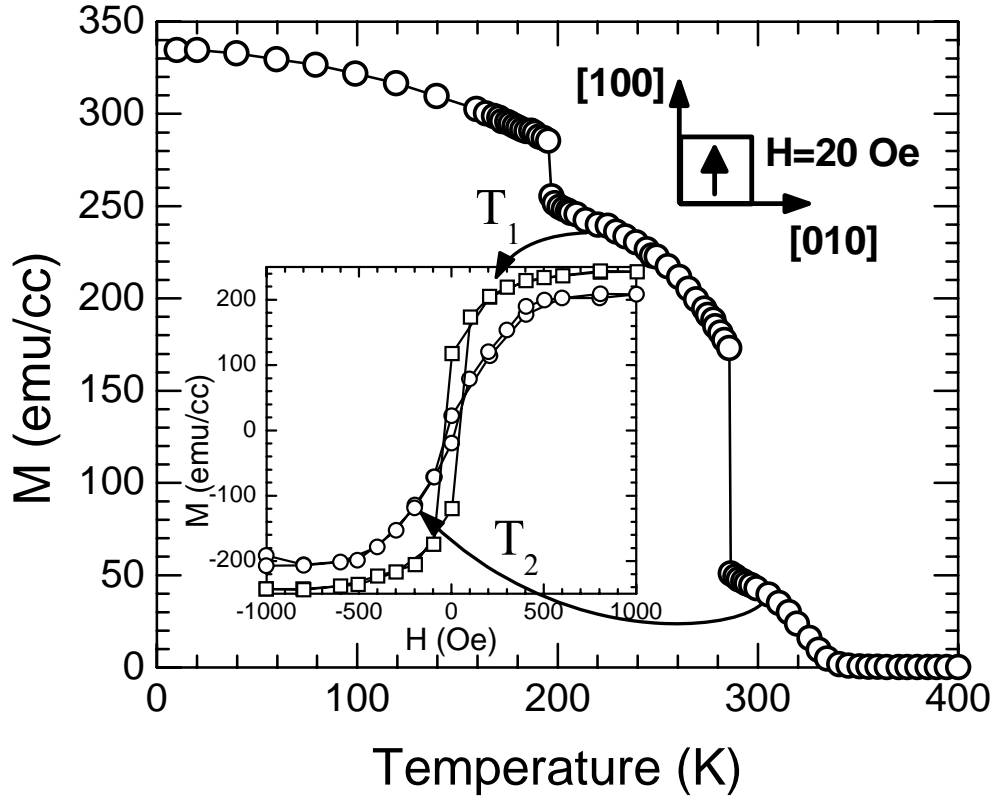


**Figure 40**

Magnetization of a 50 nm-thick  $\text{La}_{0.67}\text{Sr}_{0.33}\text{MnO}_3$  films grown on a (001)  $\text{BaTiO}_3$  substrate as a function of the temperature. The magnetic field is applied along the  $[100]$  direction. The inset shows the hysteresis loops at temperatures below ( $T_1$ ) and above ( $T_2$ ) the tetragonal to monoclinic phase transition temperature (278 K). (After Li *et al.*)



Ü. Özgür *et al.*

Journal of Materials Science: Materials in Electronics

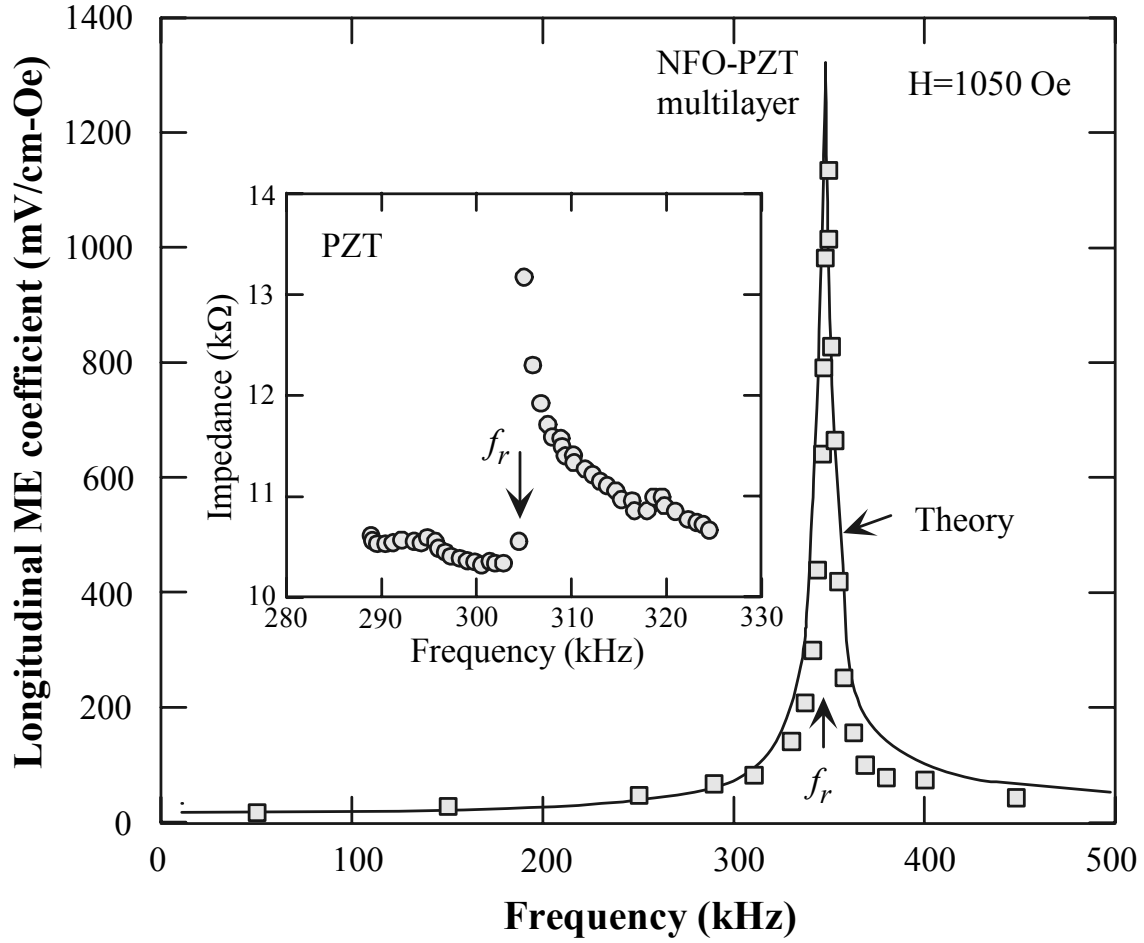


**Figure 41**

Longitudinal ME voltage coefficient as a function of the AC magnetic field frequency for a multilayer containing 11 layers of 13  $\mu\text{m}$ -thick  $\text{NiFe}_2\text{O}_4$  and 10 layers of 26  $\mu\text{m}$ -thick PZT. The solid line represents the theoretical calculations. The inset shows the impedance for a 10-mm PZT disk as a function of the frequency. (After Bichurin *et al.*)

Ü. Özgür *et al.*

Journal of Materials Science: Materials in Electronics

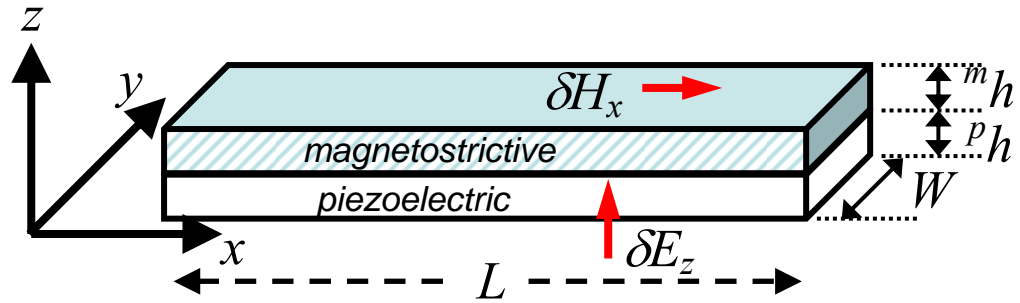


**Figure 42**

The coordinate system for a bilayer free body composed of plate-like magnetostrictive and piezoelectric layers.

Ü. Özgür *et al.*

Journal of Materials Science: Materials in Electronics

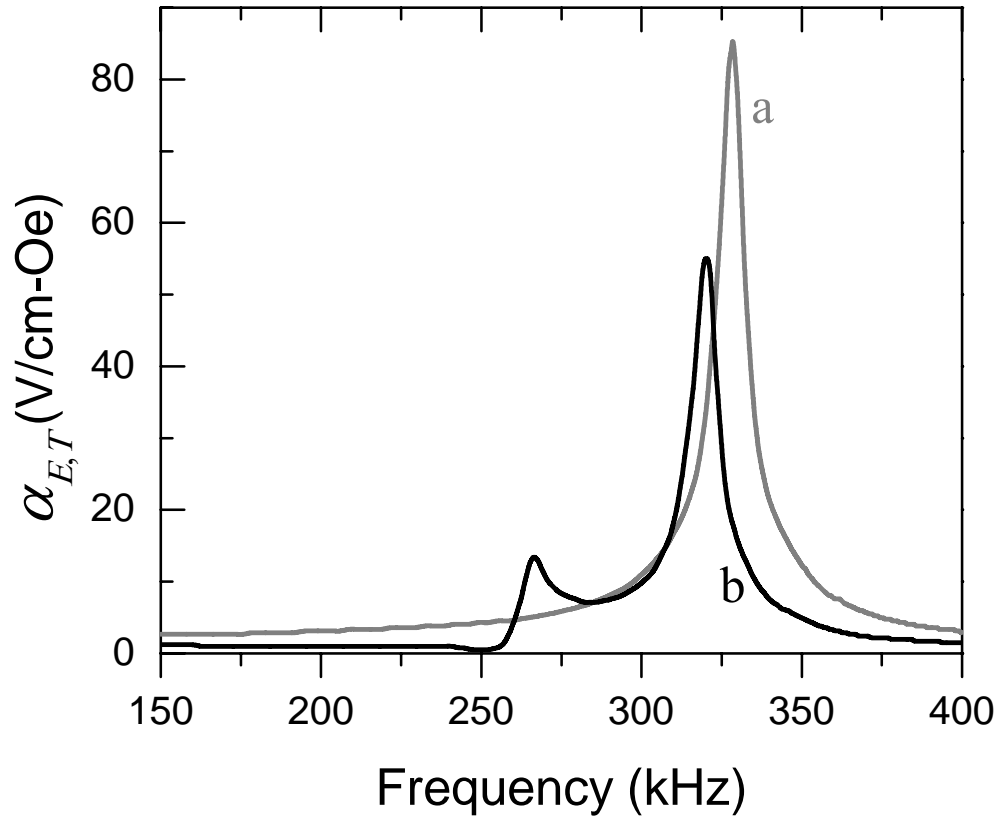
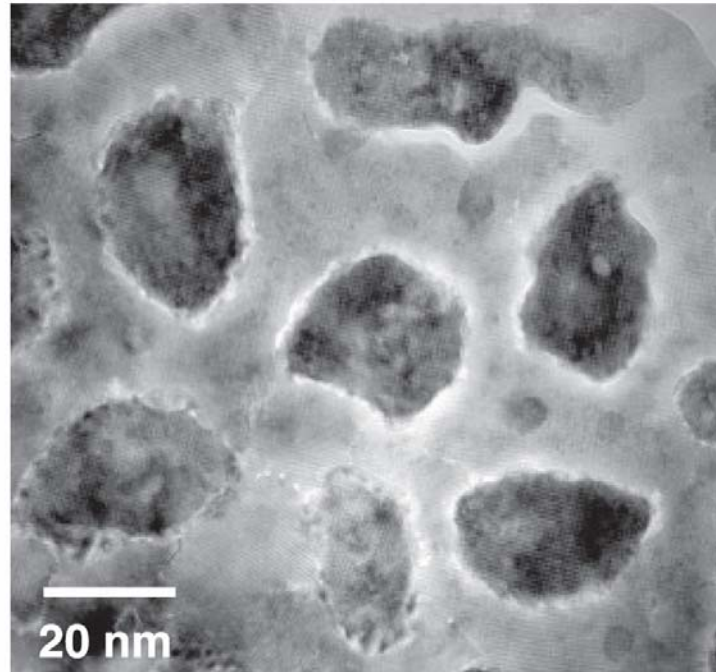


**Figure 43**

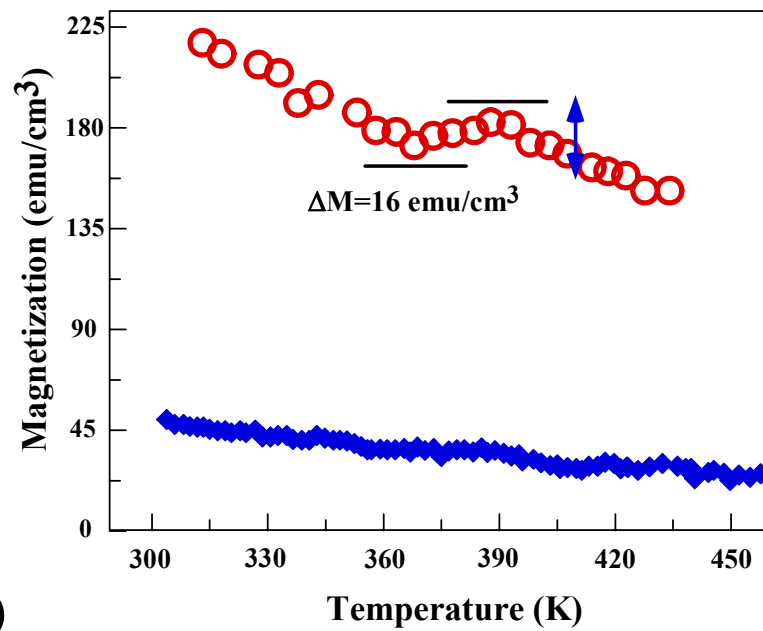
Frequency dependences of the ME voltage coefficient for Permendur-PZT bilayers structures with a coupling coefficients  $\beta$  of (a) 1.0 and (b) 0.4. (After Filippov)

Ü. Özgür *et al.*

Journal of Materials Science: Materials in Electronics



(a)



(b)

**Figure 44**

(a) TEM planar view image showing CoFe<sub>2</sub>O<sub>4</sub> nanopillars embedded in the BaTiO<sub>3</sub> matrix. (b) Magnetization as a function of the temperature measured at H=100 Oe. The

Özgür *et al.*, submitted to Journal of Materials Science: Materials in Electronics, 2009  
Microwave Ferrites, Part 2: Passive components and electrical tuning

top curve shows the data for the self assembled nanostructure, while the bottom curve is for the multilayered laminated nanostructure showing negligible change in magnetization. (After Zheng *et al.*)

Ü. Özgür *et al.*

Journal of Materials Science: Materials in Electronics

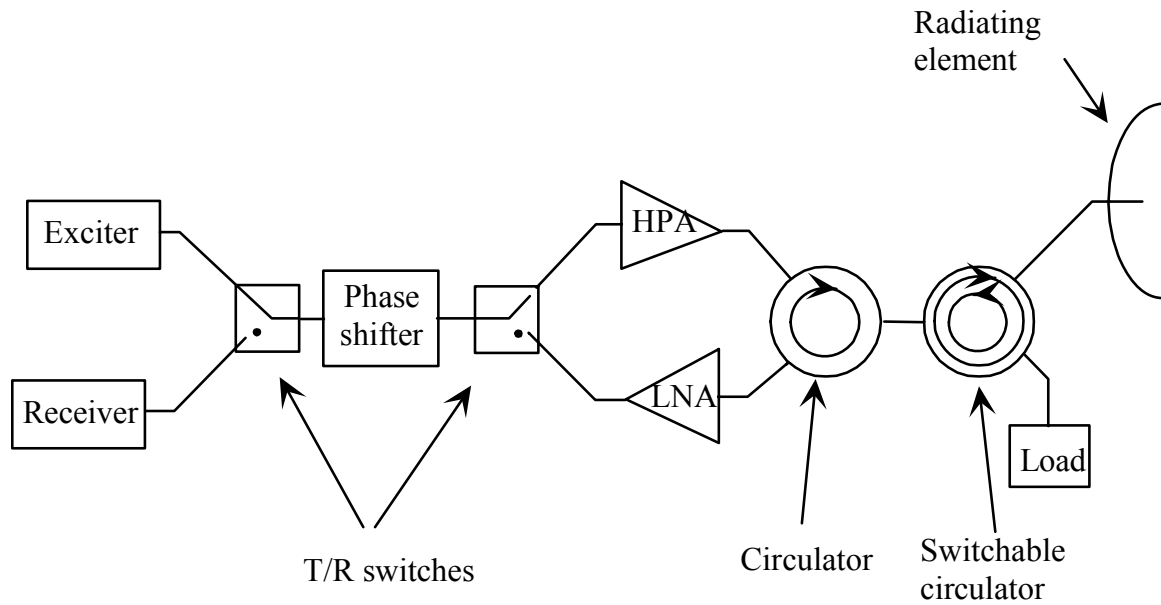


**Figure 45**

Schematic diagram of a phased-array antenna module where HPA depicts high power amplifier, and LNA low noise amplifier. After Adam *et al.*

Ü. Özgür *et al.*

Journal of Materials Science: Materials in Electronics

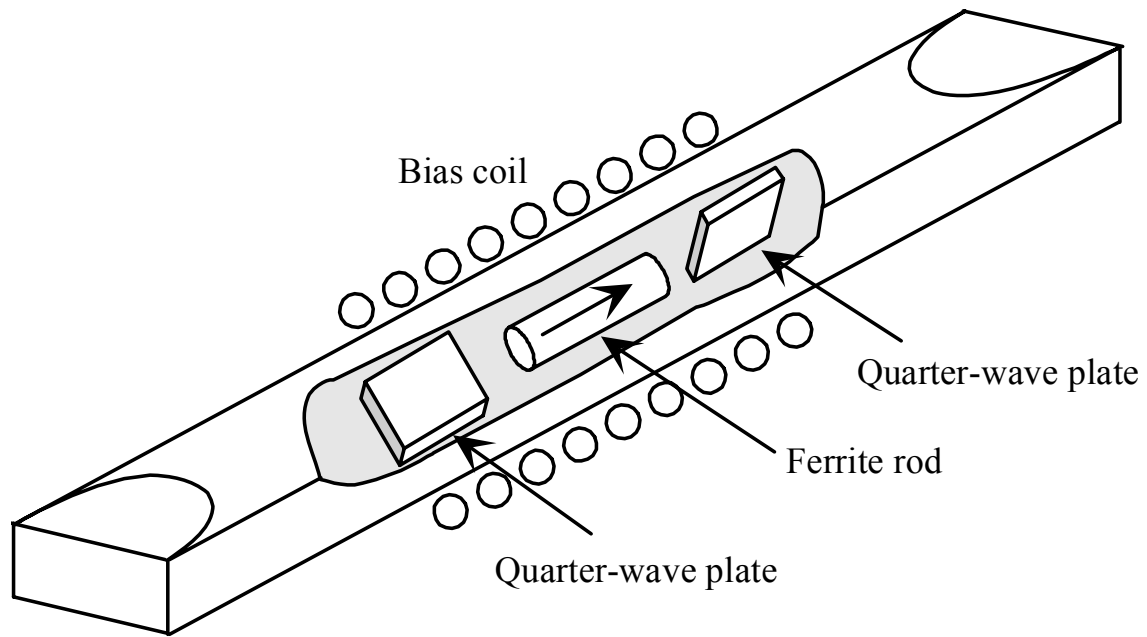


**Figure 46**  
A nonreciprocal Faraday rotation phase shifter.

Ü. Özgür *et al.*

Journal of Materials Science: Materials in Electronics

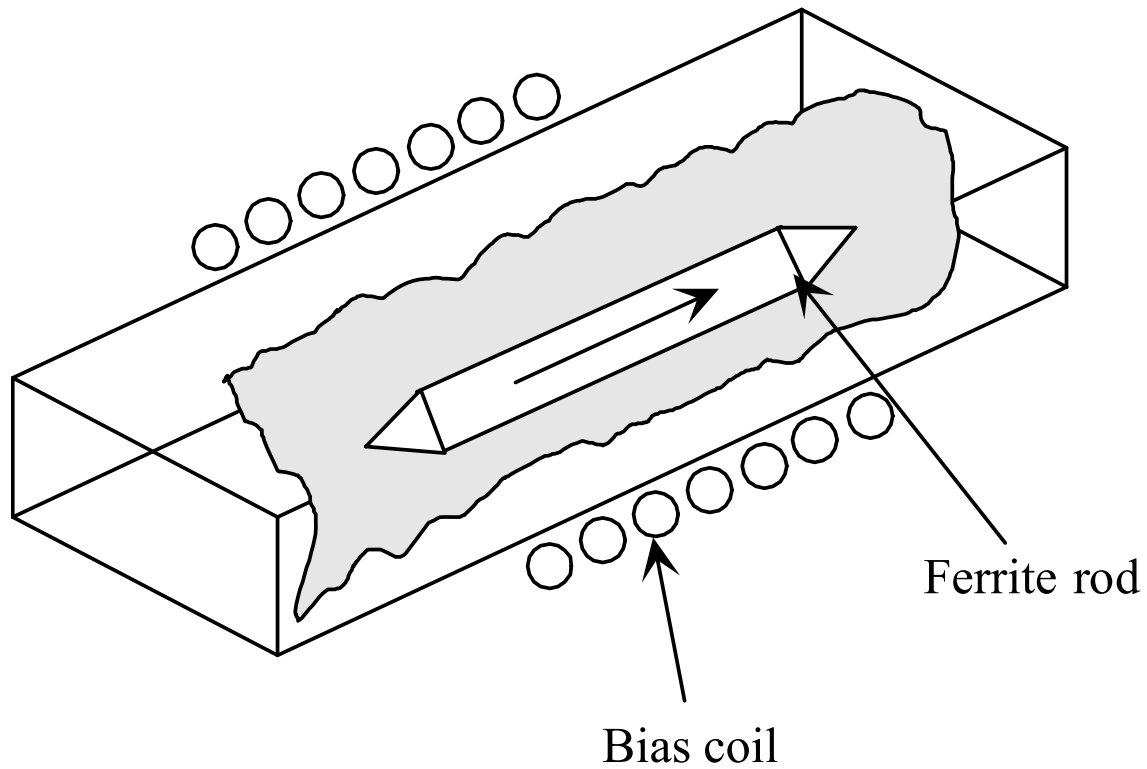


**Figure 47**  
Reggia-Spencer reciprocal phase shifter.



Ü. Özgür *et al.*

Journal of Materials Science: Materials in Electronics

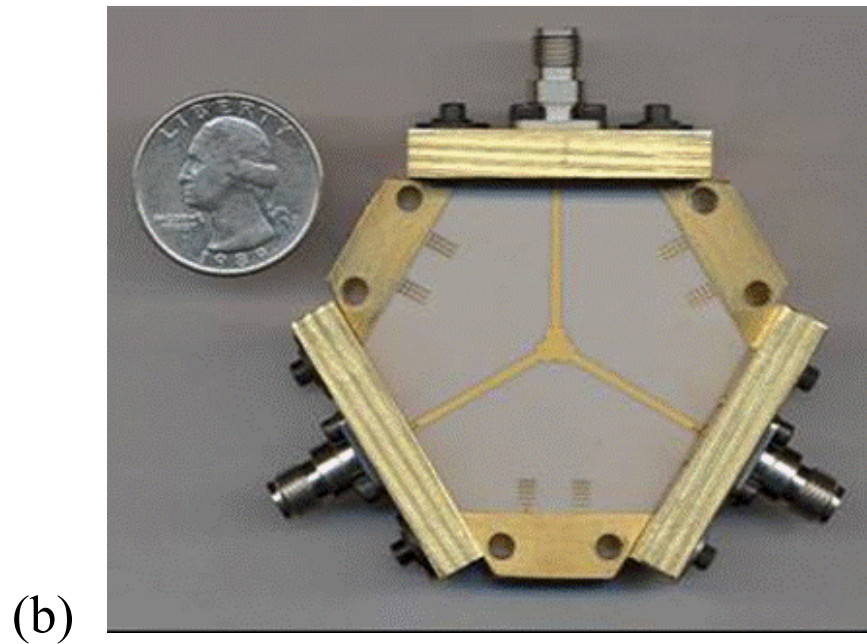
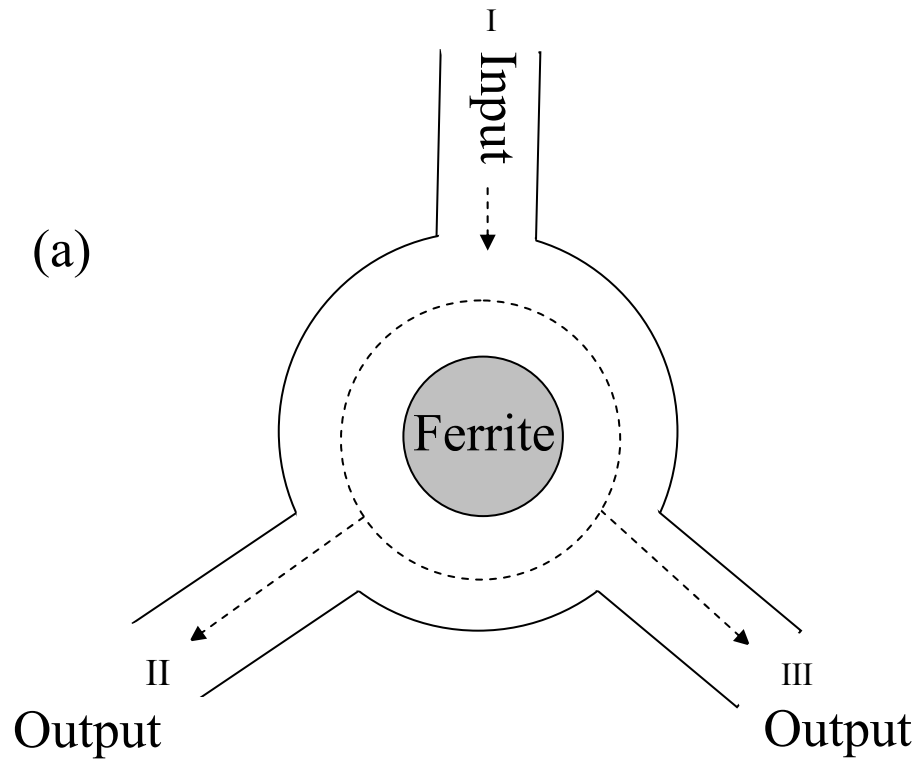


**Figure 48**

Schematic diagram (a) and photograph of a fabricated circulator (b). (Courtesy of J. Young and Y.-K. Hong)

Ü. Özgür *et al.*

Journal of Materials Science: Materials in Electronics

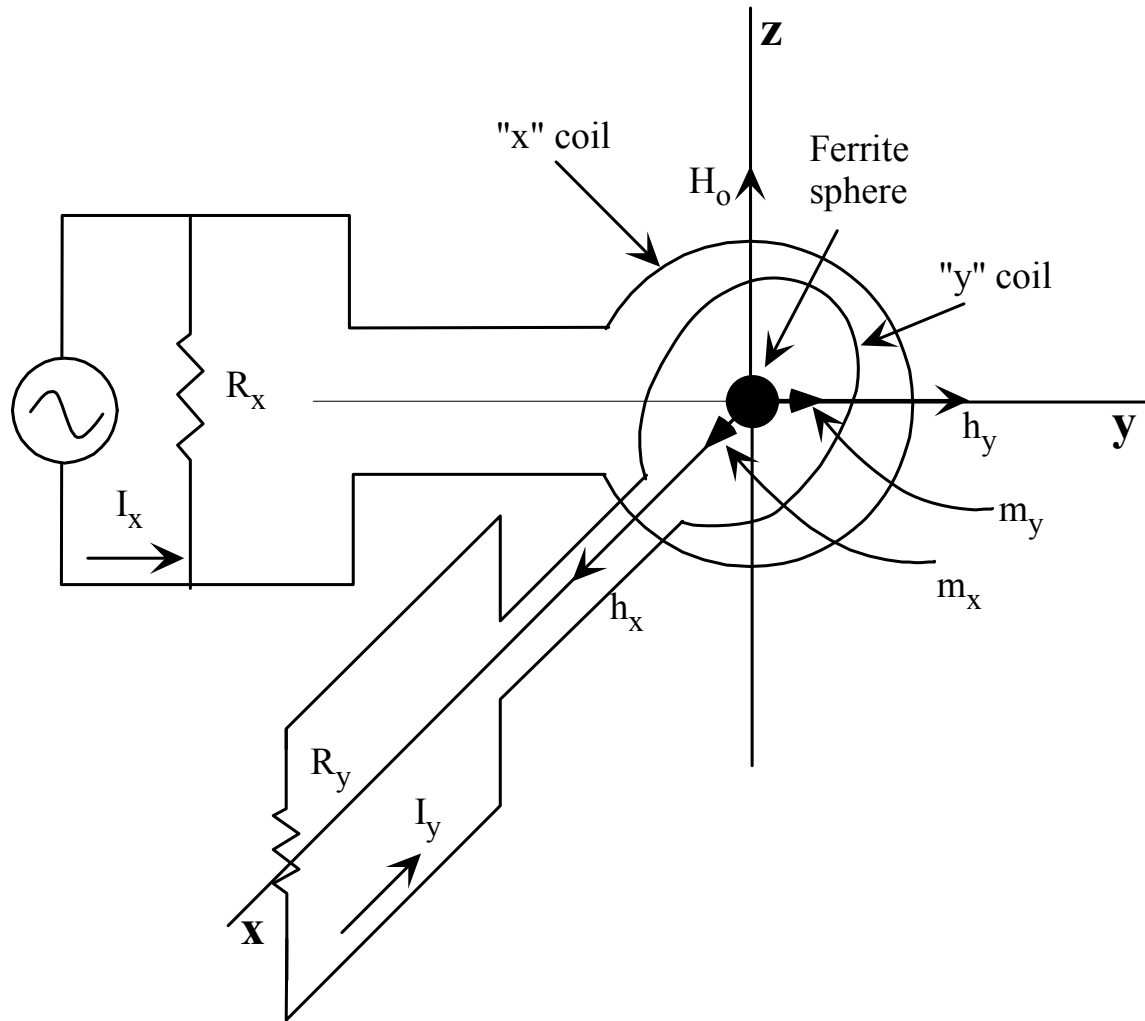


**Figure 49**  
Coupling structure for a single-stage YIG sphere filter. (After Carter.)

Ü. Özgür *et al.*

Journal of Materials Science: Materials in Electronics

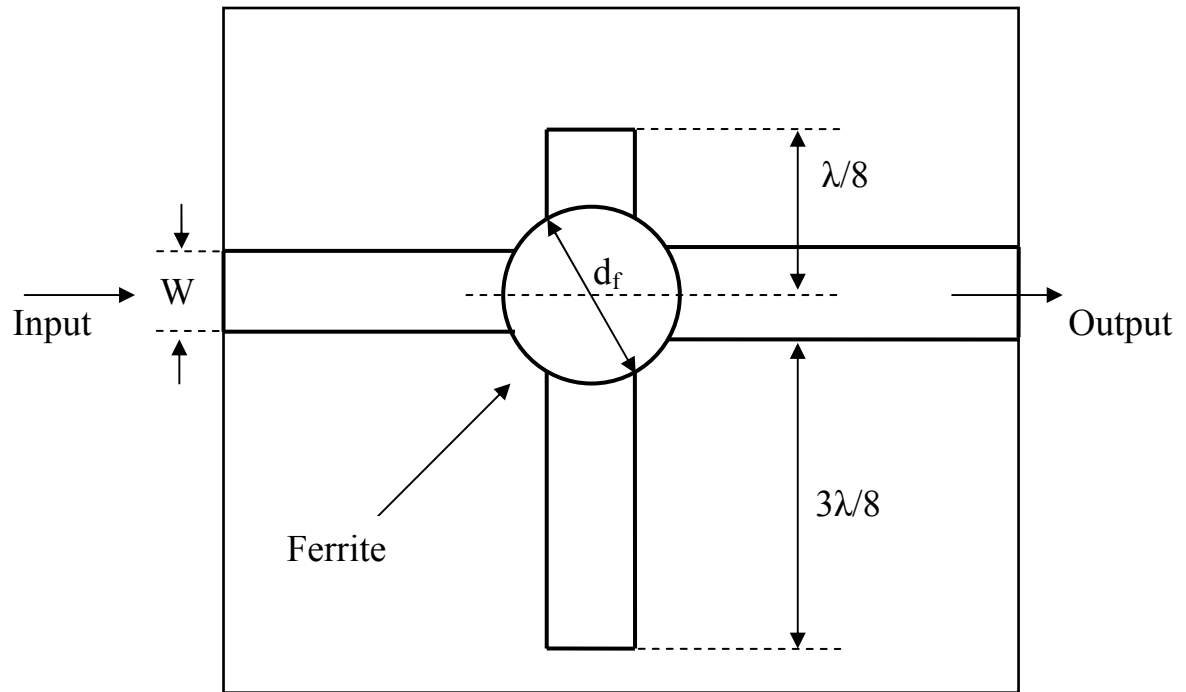


**Figure 50**  
A schematic of a resonance isolator.

Ü. Özgür *et al.*

Journal of Materials Science: Materials in Electronics

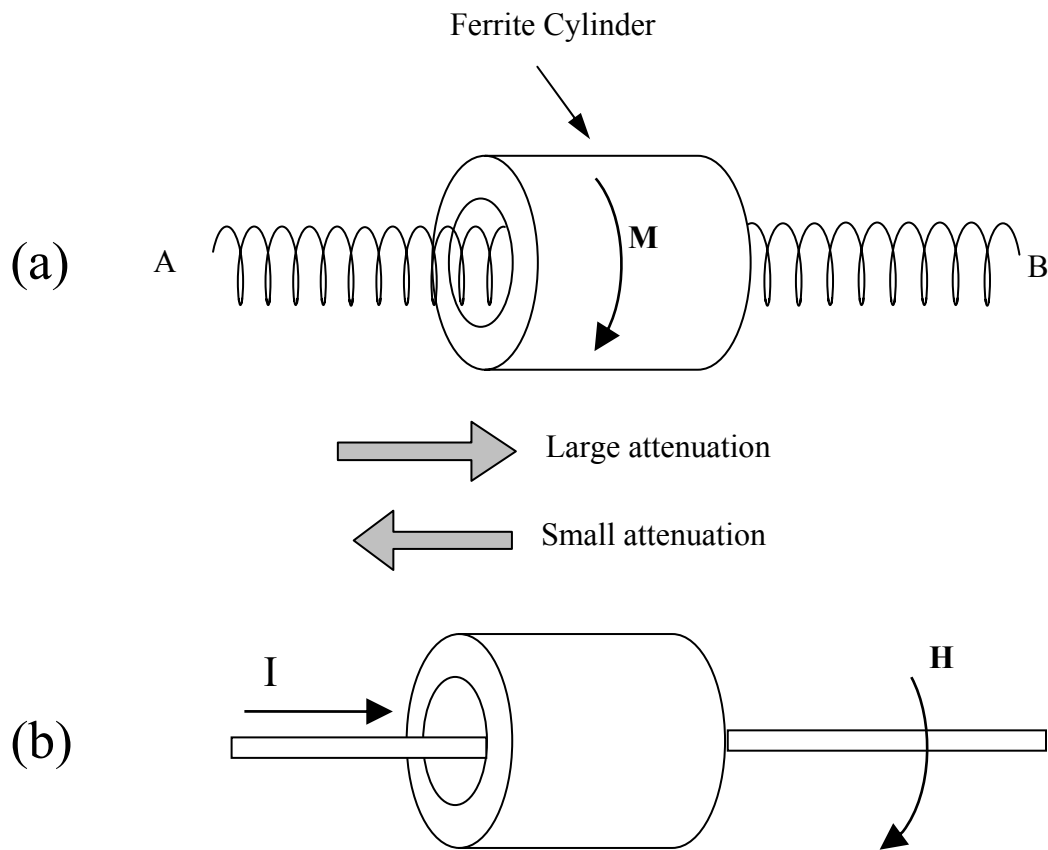


**Figure 51**

(a) Nonreciprocal attenuator. (b) The magnetization of the ferrite cylinder is achieved by passing a current ( $\mathbf{I}$ ) through its central axis. (After Enander.)

Ü. Özgür *et al.*

Journal of Materials Science: Materials in Electronics

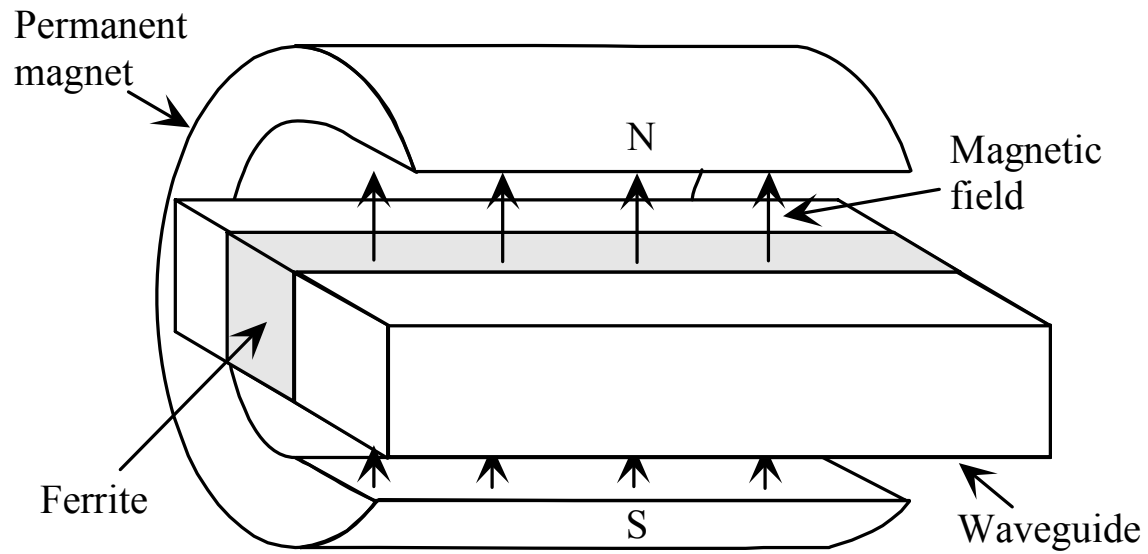


**Figure 52**  
A sample junction ferrite microwave isolator.

Ü. Özgür *et al.*

Journal of Materials Science: Materials in Electronics

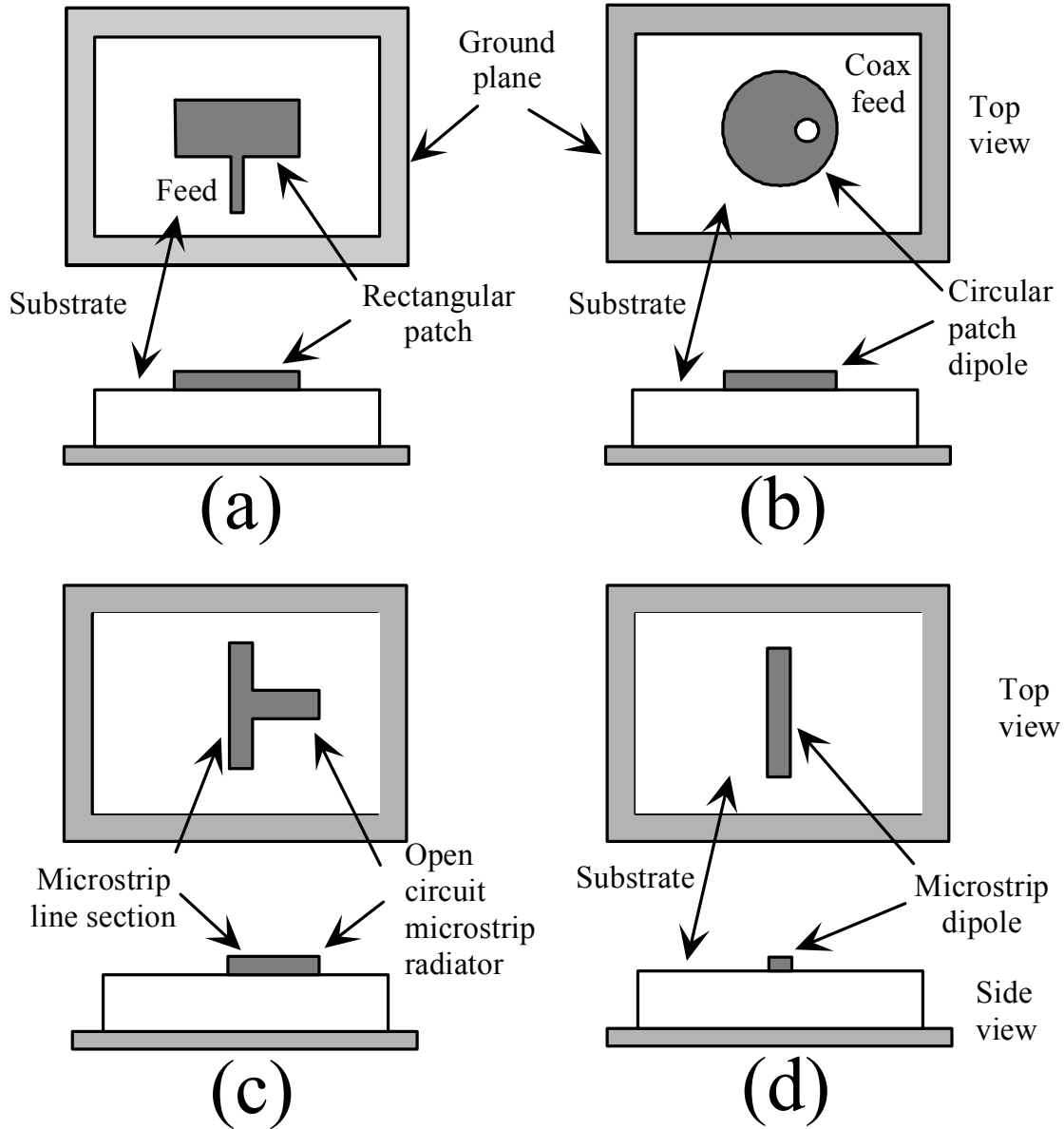


**Figure 53**

Different types of microstrip antennas: (a) Rectangular microstrip patch antenna. (b) Circular microstrip patch antenna. (c) Open-circuit microstrip radiator. (d) Microstrip dipole antenna. (After Carver and Mink.)

Ü. Özgür *et al.*

Journal of Materials Science: Materials in Electronics

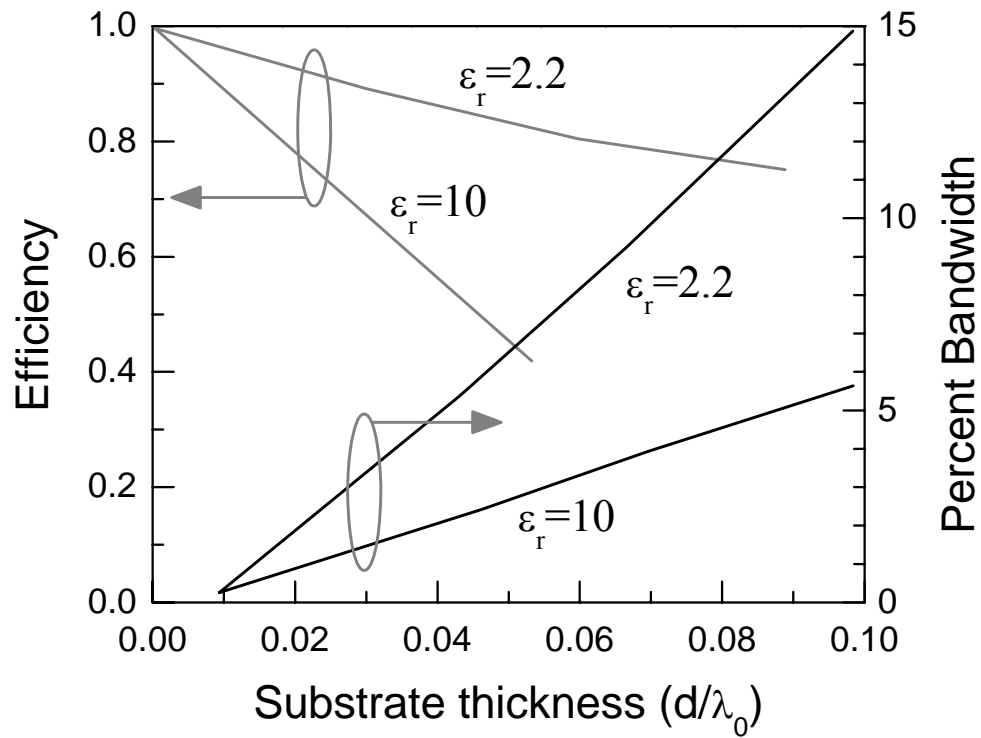


**Figure 54**

Efficiency and bandwidth of a microstrip antenna versus substrate thickness normalized to wavelength. (After Pozar.)



Ü. Özgür *et al.*

Journal of Materials Science: Materials in Electronics

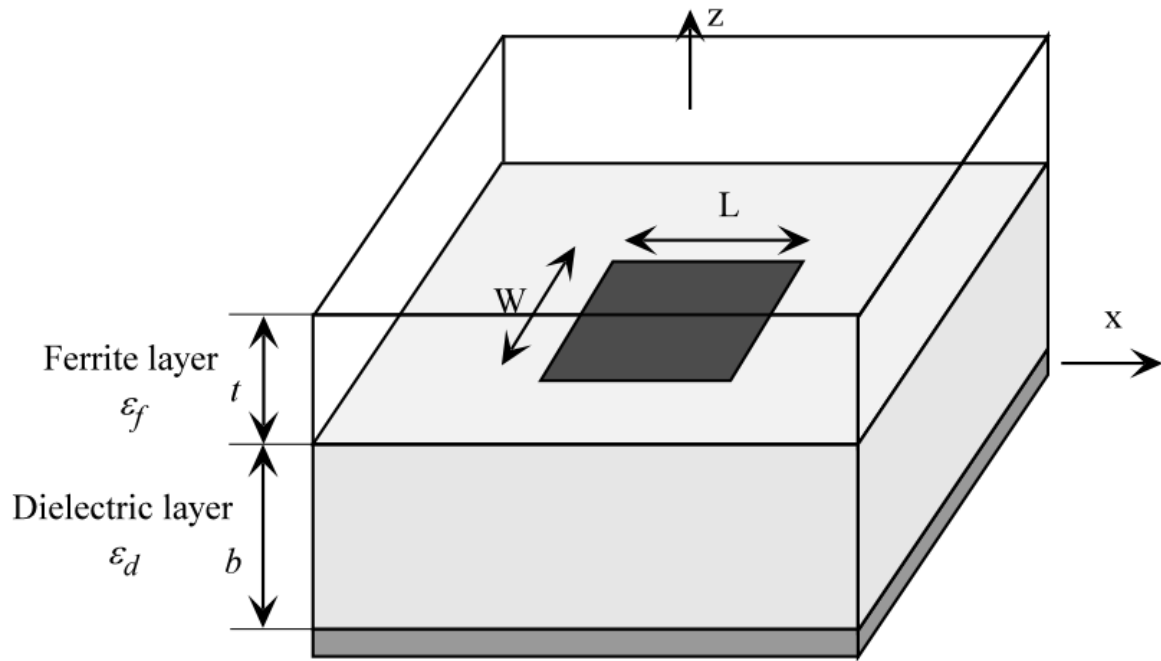


**Figure 55**

Geometry of a microstrip antenna with an in-plane biased ferrite cover layer. (After Yang.)

Ü. Özgür *et al.*

Journal of Materials Science: Materials in Electronics

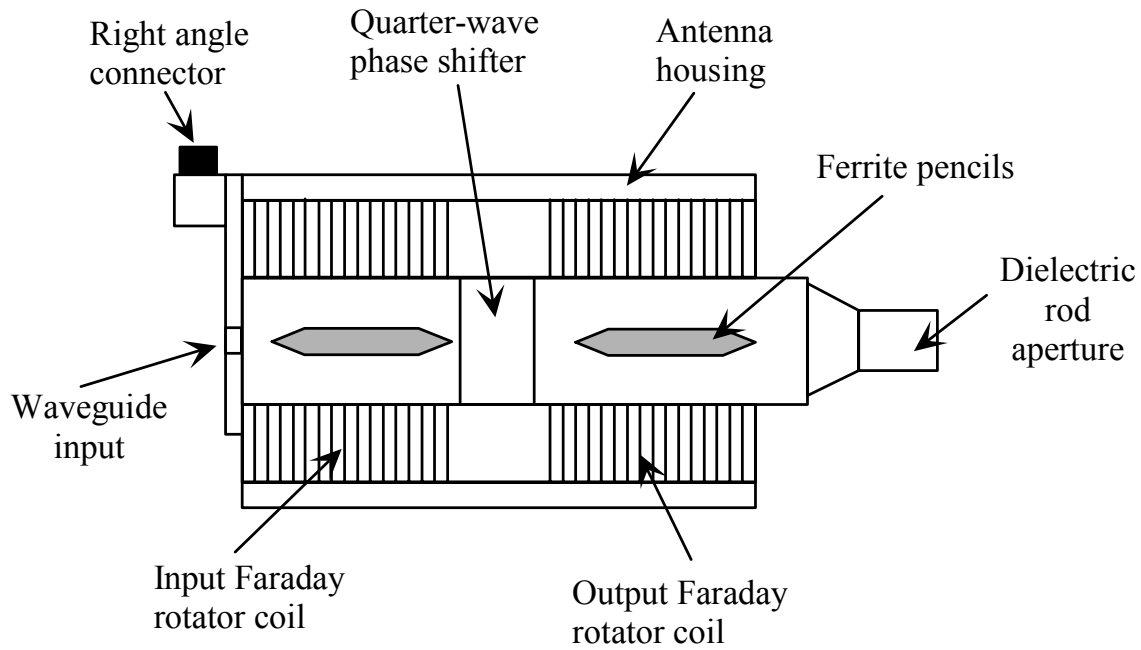


**Figure 56**

Configuration of the variable polarization ferrite antenna. (After Dunn *et al.*)

Ü. Özgür *et al.*

Journal of Materials Science: Materials in Electronics

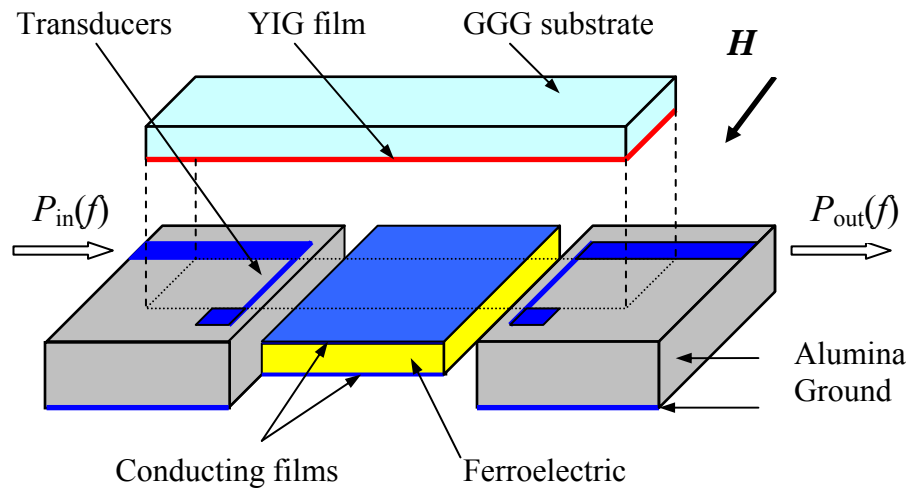


**Figure 57**

A delay line based on a YIG/PMN-PT bilayer. (After Fetisov and Srinivasan.)

Ü. Özgür *et al.*

Journal of Materials Science: Materials in Electronics

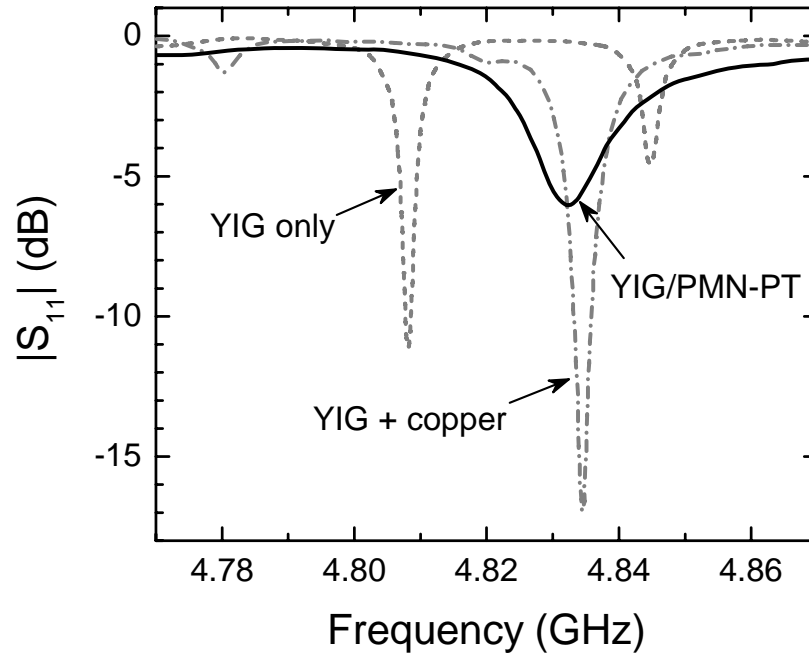


**Figure 58**

Frequency responses of the stand-alone YIG sample (dash curve), YIG/PMN-PT resonator (solid curve), and YIG sample with a rectangular copper piece on top (dash-dot curve). (After Ustinov *et al.*)

Ü. Özgür *et al.*

Journal of Materials Science: Materials in Electronics

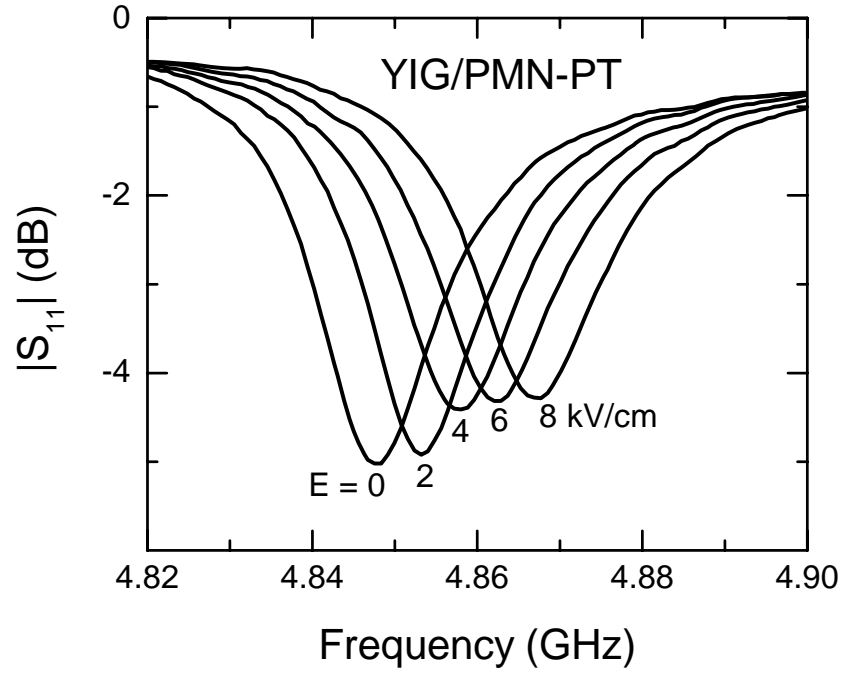


**Figure 59**

FMR frequency spectra for the YIG/PMN-PT resonator measured at various electric fields for  $H = 1012$  Oe applied parallel to the resonator plane. (After Ustinov *et al.*)

Ü. Özgür *et al.*

Journal of Materials Science: Materials in Electronics

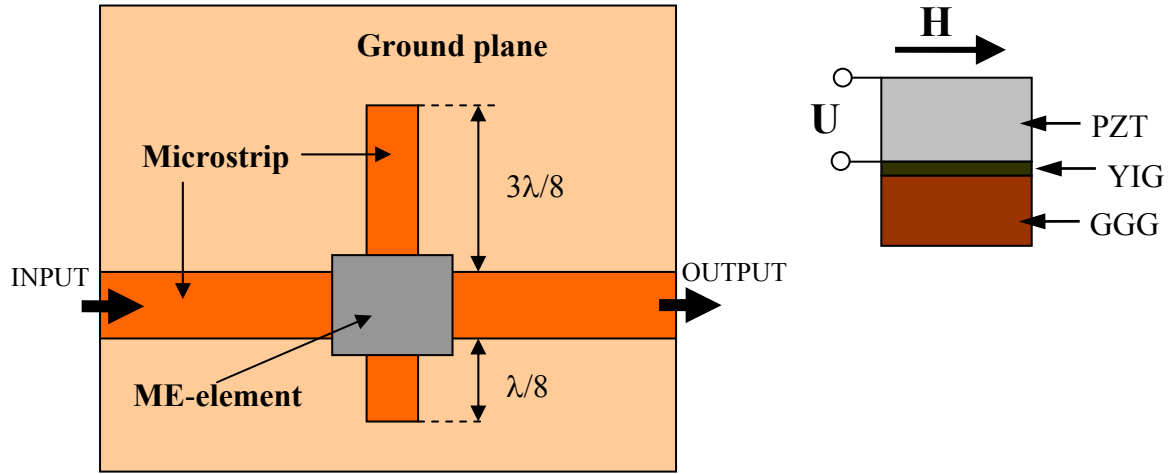


**Figure 60**

Schematics of a magnetoelectric (ME) nonreciprocal microwave phase shifter showing a ME resonator of yttrium iron garnet (YIG) film on gadolinium gallium garnet (GGG) substrate bonded to lead zirconate titanate (PZT), and microstrip transducers and stubs. (After Tatarenko *et al.*)

Ü. Özgür *et al.*

Journal of Materials Science: Materials in Electronics

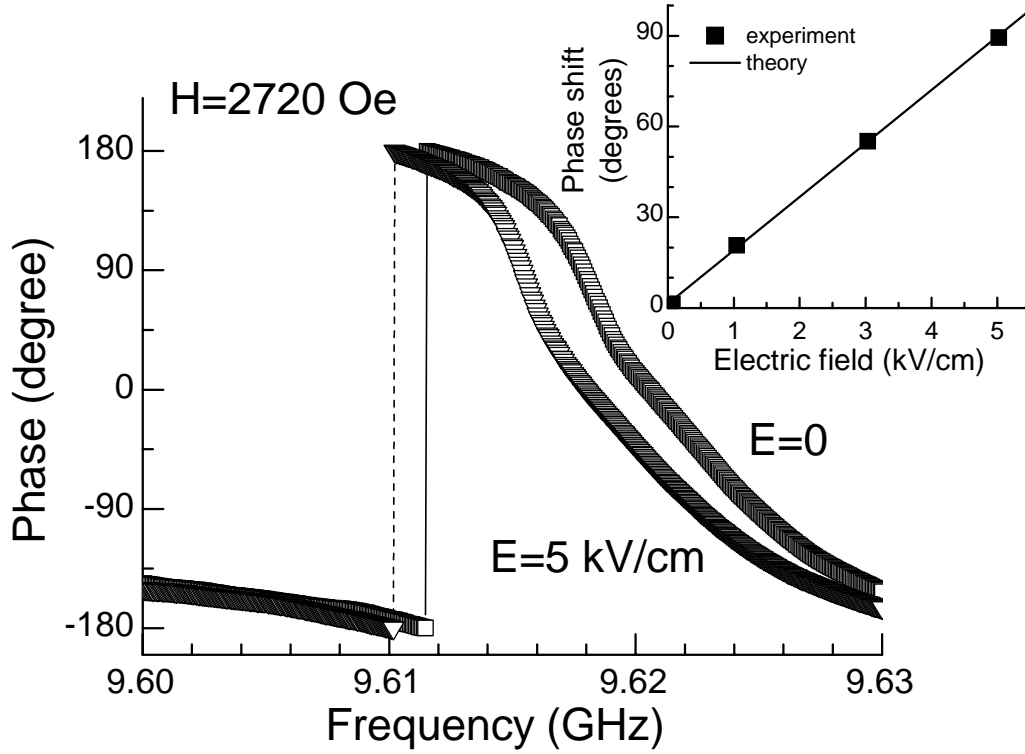


**Figure 61**

The phase angle  $\phi$  vs. frequency  $f$  characteristics at 9.6 GHz for  $E = 0$  and 5 kV/cm. The applied bias field is  $H_0 = 2720$  Oe, which corresponds to a region in which the variation of the real part of the permeability  $\mu'$  with the magnetic field is linear. (After Tatarenko *et al.*)

Ü. Özgür *et al.*

Journal of Materials Science: Materials in Electronics

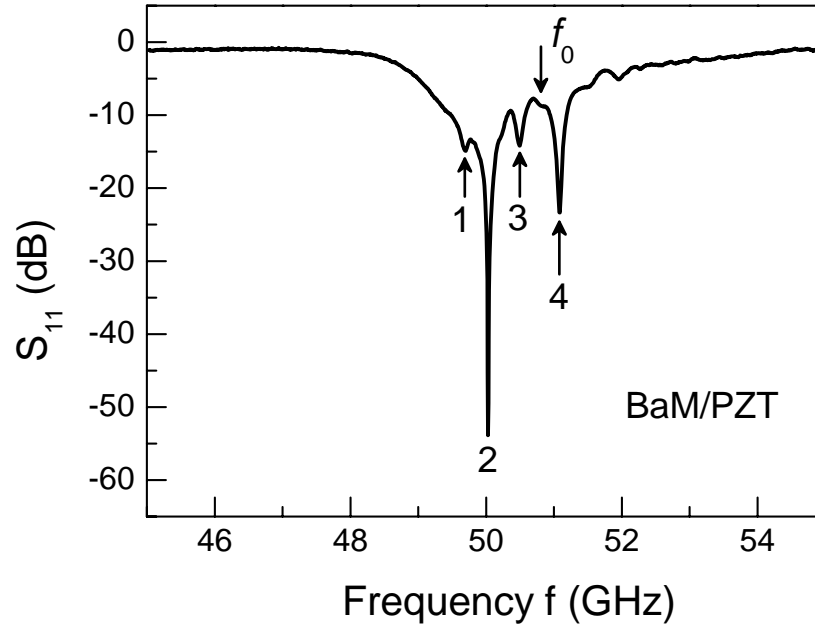


**Figure 62**

Reflected power as a function of the frequency for a BaM/PZT bilayer with a 185  $\mu\text{m}$ -thick ferrite under a static magnetic field of 5980 Oe applied along the c-axis of BaM. (After Srinivasan *et al.*)



## References

---

- <sup>1</sup> Ü. Özgür, Y. Alivov, and H. Morkoç, “Microwave Ferrites, Part 1: Fundamentals and self biasing”, to be published in J. Mater. Sci.: Materials in Electronics, 2009.
- <sup>2</sup> C. W. Nan, M. I. Bichurin, S. Dong, D. Viehland, and G. Srinivasan, J. Appl. Phys. **103**, 031101 (2008).
- <sup>3</sup> W. Eerenstein, N. D. Mathur, and J. F. Scott, Nature **442**, 759 (2006).
- <sup>4</sup> M. Fiebig, J. Phys. D **38**, R123 (2005).
- <sup>5</sup> S. L. Hou and N. Bloembergen, Phys. Rev. **138**, A1218 (1965).
- <sup>6</sup> R. E. Cohen, Nature **358**, 136 (1992).
- <sup>7</sup> N. A. Hill, J. Phys. Chem. B **104**, 6694 (2000).
- <sup>8</sup> K. Lefki and G. J. M. Dormans, J. Appl. Phys. **76**, 1764 (1994).
- <sup>9</sup> Etienne du Trémolet de Lacheisserie, “Magnetostriction: Theory and Applications of Magnetoelasticity”, CRC Press, Inc, Boca Raton, 1993, Chapter 2.
- <sup>10</sup> C. Kittel, Rev. Mod. Physics **21**, 541 (1949).
- <sup>11</sup> R. A. McCurie, “Ferromagnetic Materials, Structure and Properties”, Academic Press, San Diego, CA, 1994, page 91.
- <sup>12</sup> G. Harshé, J. P. Dougherty, and R. E. Newnham, Int. J. Appl. Electromag. Mat. **4**, 145 (1993).
- <sup>13</sup> J. Van Den Boomgard, A. M. J. G. Van Run, and J. Van Suchtelen, Ferroelectrics **10**, 295 (1976).
- <sup>14</sup> A. S. Zubkov, Elektrichestvo **10**, 77 (1978).
- <sup>15</sup> A. L. Kholkin, E. K. Akdogan, A. Safari, P.-F. Chauvy, and N. Setter, J. Appl. Phys. **89**, 8066 (2001).
- <sup>16</sup> S. Zhang, L. Lebrun, D.-Y. Jeong, C. A. Randall, Q. Zhang, and T. R. Shrout, J. Appl. Phys. **93**, 9257 (2003).
- <sup>17</sup> G. Srinivasan, E. T. Rasmussen, B. J. Levin, and R. Hayes, Phys. Rev. B **65**, 134402 (2002).
- <sup>18</sup> E. I. Dzyaloshinskii, Sov. Phys. JETP **10**, 628 (1959).
- <sup>19</sup> G. T. Rado and V. J. Folen, Phys. Rev. Lett. **7**, 310 (1961).
- <sup>20</sup> S. Foner and M. Hanabusa, J. Appl. Phys. **34**, 1246 (1963).
- <sup>21</sup> D. N. Astrov, Soviet Phys. JETP **11**, 708 (1961); D. N. Astrov, Soviet Phys. JETP **13**, 729 (1961).
- <sup>22</sup> V. J. Folen, G. T. Rado, and E. W. Stalder, Phys. Rev. Lett. **6**, 607 (1961).
- <sup>23</sup> J. P. Rivera, Ferroelectrics **161**, 165 (1994).

- <sup>24</sup> B. I. Al'shin and D. N. Astrov, Sov. Phys. JETP **17**, 809 (1963).
- <sup>25</sup> G. T. Rado, Phys. Rev. Lett **13**, 335 (1964).
- <sup>26</sup> R. P. Santoro, D. J. Segal, and R. E. Newnham, J. Phys. Chem. Solids **27**, 1192 (1966).
- <sup>27</sup> I. Kornev, M. Bichurin, J.-P. Rivera, S. Gentil, A. G. M. Jansen, H. Schmid, and P. Wyder, Phys. Rev. B **62**, 12247 (2000).
- <sup>28</sup> D. Vaknin, J. L. Zarestky, J. P. Rivera, and H. Schmid, Phys. Rev. Lett. **92**, 207201 (2004).
- <sup>29</sup> J. F. Scott, Phys. Rev B **16**, 2329 (1977).
- <sup>30</sup> B. Ponomarev, S. A. Ivanov, Yu F Popov, V. D. Negrii, and B. S. Redkin, Ferroelectrics **161**, 43 (1994).
- <sup>31</sup> E. Ascher, H. Rieder, H. Schmid, and H. Stössel, J. Appl. Phys. **37**, 1404 (1966).
- <sup>32</sup> G. A. Smolenskii and I. E. Chupis, Sov. Phys. Usp. **25**, 475 (1982).
- <sup>33</sup> T. Watanabe and K. Kohn, Phase Trans. **15**, 57 (1989).
- <sup>34</sup> G. A. Smolenskii, A. I. Agranovskaya, and V. A. Isupov, Sov. Phys. Solid State **1**, 442 (1959).
- <sup>35</sup> H. Tsujino and K. Kohn, Solid State Commun. **83**, 639 (1992).
- <sup>36</sup> N. Hur, S. Park, P. A. Sharma, J. S. Ahn, S. Guha, and S.-W. Cheong, Nature **429**, 392 (2004).
- <sup>37</sup> T. Kimura, G. Lawes, and A. P. Ramirez, Phys. Rev. Lett. **94**, 137201 (2005).
- <sup>38</sup> M. Fiebig, Th. Lottermoser, D. Frohlich, A. V. Goltsev, and R. V. Pisarev, Nature **419**, 818 (2002)
- <sup>39</sup> V. Laukhin, V. Skumryev, X. Martí, D. Hrabovsky, F. Sánchez,<sup>†</sup> M.V. García-Cuenca, C. Ferrater, M. Varela, U. Lüders, J. F. Bobo, and J. Fontcuberta, Phys. Rev. Lett. **97**, 227201 (2006)
- <sup>40</sup> A. Moreira dos Santos, S. Parashar, A. R. Raju, Y. S. Zhao, A. K. Cheetham, and C. N. R. Rao, Solid State Comm. **122**, 49 (2002).
- <sup>41</sup> T. Kimura, S. Kawamoto, I. Yamada, M. Azuma, M. Takano, and T. Yokura, Phys. Rev. B **67**, 180401 (2003).
- <sup>42</sup> J. Hemberger, P. Lunkenheimer, R. Fichtl, H.-A. Krug von Nidda, V. Tsurkan, and A. Loidl, Nature **434**, 364 (2005).
- <sup>43</sup> T. H. O'Dell, Phil. Mag. **16**, 487 (1967).
- <sup>44</sup> B. B. Krichevstov, V. V. Pavlov, R. V. Pasarev, and A. G. Selitsky, Ferroelectrics **161**, 65 (1994).
- <sup>45</sup> J. P. Rivera, Ferroelectrics **161**, 147 (1994).
- <sup>46</sup> B. B. Krichevstov, V. V. Pavlov, and R. V. Pisarev, JETP Lett. **49**, 535 (1989).

- <sup>47</sup> G. T. Rado, J. M. Ferrari, and W. G. Maisch, *Phys. Rev. B* **29**, 4041 (1984).
- <sup>48</sup> J. Wang, J. B. Neaton, H. Zheng, V. Nagarajan, S. B. Ogale, B. Liu, D. Viehland, V. Vaithyanathan, D. G. Schlom, U. V. Waghmare, N. A. Spaldin, K. M. Rabe, M. Wuttig, and R. Ramesh, *Science* **299**, 1719 (2003).
- <sup>49</sup> Yu. F. Popov, A. M. Kadomtseva, S. S. Krotov, D. V. Belov, G. P. Vorob'ev, P. N. Makhov, and A. K. Zvezdin, *Low. Temp. Phys.* **27**, 478 (2001).
- <sup>50</sup> A. K. Zvezdin, A. M. Kadomtseva, S. S. Krotov, A. P. Pyatakov, Yu. F. Popov, G.P. Vorob'ev, *J. Magnetism Magnetic Mater.* **300**, 224 (2006).
- <sup>51</sup> W. Eerenstein, F. D. Morrison, J. Dho, M. G. Blamire, J. F. Scott, and N. D. Mathur, *Science* **307**, 1203 (2005).
- <sup>52</sup> S. Dong, J. Zhai, J.-F. Li, and D. Viehland, *Appl. Phys. Lett.* **89**, 122903 (2006).
- <sup>53</sup> S. Dong, J. Zhai, F. Bai, J.-F. Li, and D. Viehland, *Appl. Phys. Lett.* **87**, 062502 (2005).
- <sup>54</sup> V. Corral-Flores, D. Bueno-Baques, D. Carrillo-Flores, and J. A. Matutes-Aquino, *J. Appl. Phys.* **99**, 08J503 (2006).
- <sup>55</sup> S. Stein, M. Wuttig, D. Viehland, and E. Quandt, *J. Appl. Phys.* **97**, 10Q301 (2005).
- <sup>56</sup> T. Wu, M. A. Zurbuchen, S. Saha, R.-V. Wang, S. K. Streiffer, and J. F. Mitchell, *Phys. Rev. B* **73**, 134416 (2006).
- <sup>57</sup> G. Srinivasan, E. T. Rasmussen, J. Gallegos, R. Srinivasan, Yu. I. Bokhan and V. M. Laletin, *Phys. Rev. B* **64**, 214408 (2001).
- <sup>58</sup> N. Zhang, Dekai Liang, T. Schneider, and G. Srinivasan, *J. Appl. Phys.* **101**, 083902 (2007).
- <sup>59</sup> G. Srinivasan, C. P. De Vreugd, V. M. Laletin, N. Paddubnaya, M. I. Bichurin, V. M. Petrov, and D. A. Filippov, *Phys. Rev. B* **71**, 184423 (2005).
- <sup>60</sup> J. Ryu, A. V. Carazo, K. Uchino, and H. E. Kim, *Jpn. J. Appl. Phys.* **40**, 4948 (2001).
- <sup>61</sup> H. Ryu, P. Murugavel, J. H. Lee, S. C. Chae, T. W. Noh, Y. S. Oh, H. J. Kim, K. H. Kim, J. H. Jang, M. Kim, C. Bae, and J.-G. Park, *Appl. Phys. Lett.* **89**, 102907 (2006).
- <sup>62</sup> J. Zhai, N. Cai, Z. Shi, Y. Lin, C.-W. Nan, *J. Phys. D* **37**, 823 (2004).
- <sup>63</sup> R. S. Devan and B. K. Chougule, *J. Appl. Phys.* **101**, 014109 (2007).
- <sup>64</sup> J.-P. Zhou, H.-C. He, Z. Shi, G. Liu, and C.-W. Nan, *J. Appl. Phys.* **100**, 094106 (2006).
- <sup>65</sup> Y. Jia, S. W. Or, J. Wang, H. L. W. Chan, X. Zhao, and H. Luo, *J. Appl. Phys.* **101**, 104103 (2007).
- <sup>66</sup> S. Dong and D. Viehland, *IEEE Transactions on Ultrasonics, Ferroelectrics, and Frequency Control* **50**, 1236 (2003).
- <sup>67</sup> J. G. Wan, J. M. Liu, H. L. W. Chan, C. L. Choy, G. H. Wang, and C. W. Nan, *J. Appl. Phys.* **93**, 9916 (2003).

- 
- <sup>68</sup> M. Zeng, J. G. Wan, Y. Wang, H. Yu, J.-M. Liu, X. P. Jiang, and C. W. Nan, *J. Appl. Phys.* **95**, 8069 (2004).
- <sup>69</sup> S. Dong, J. Cheng, J. F. Li, and D. Viehland, *Appl. Phys. Lett.* **83**, 4812 (2003).
- <sup>70</sup> M. I. Bichurin, D. A. Filippov, V. M. Petrov, V. M. Laletsin, N. Paddubnaya, and G. Srinivasan, *Phys. Rev. B* **68**, 132408 (2003).
- <sup>71</sup> N. Zhang, W. Ke, T. Schneider, and G. Srinivasan, *J. Phys.:Condens. Matter* **18**, 11013 (2006).
- <sup>72</sup> C. Thiele, K. Dörr, O. Bilani, J. Rödel, and L. Schultz, *Phys. Rev. B* **75**, 054408 (2007).
- <sup>73</sup> A. M. J. G. Vanrun, D. R. Terrell, and J. H. Scholing, *J. Mater. Sci.* **9**, 1710 (1974).
- <sup>74</sup> J. van den Boomgaard and R. A. J. Born, *J. Mater. Sci.* **13**, 1538 (1978).
- <sup>75</sup> N. Cai, J. Zhai, C. W. Nan, Y. Lin, and Z. Shi, *Phys. Rev. B* **68**, 224103 (2003).
- <sup>76</sup> H. S. Shastri, G. Srinivasan, M. I. Bichurin, V. M. Petrov, and A. S. Tatarenko, *Phys. Rev. B* **70**, 064416 (2004).
- <sup>77</sup> Y. K. Fetisov and G. Srinivasan, *Appl. Phys. Lett.* **88**, 143503 (2006).
- <sup>78</sup> S. X. Dong, J. F. Li, and D. Viehland, *Appl. Phys. Lett.* **85**, 2307 (2004).
- <sup>79</sup> U. Laletsin, N. Padubnaya, G. Srinivasan, and C. P. DeVreugd, *Appl. Phys. A: Mater. Sci. Process.* **78**, 33 (2004).
- <sup>80</sup> J. G. Wan, Z. Y. Li, Y. Wang, M. Zeng, G. H. Wang, and J. M. Liu, *Appl. Phys. Lett.* **86**, 202504 (2005).
- <sup>81</sup> P. Murugavel, P. Padhan, and W. Prellier, *Appl. Phys. Lett.* **85**, 4992 (2004).
- <sup>82</sup> S. Srinath, N. A. Frey, R. Heindl, H. Srikanth, K. R. Coffey, and N. J. Dudley, *J. Appl. Phys.* **97**, 10J115 (2005).
- <sup>83</sup> M. Steinhart, J. H. Wendorff, A. Greiner, R. B. Wehrspohn, K. Nielsch, J. Schilling, J. Choi, and U. Gosele, *Science* **296**, 1997 (2002).
- <sup>84</sup> Y. Luo, I. Szafraniak, N. D. Zakharov, V. Nagarajan, M. Steinhart, R. B. Wehrspohn, J. H. Wendorff, R. Ramesh, and M. Alexe, *Appl. Phys. Lett.* **83**, 440 (2003).
- <sup>85</sup> B. A. Hernandez, K. S. Chang, E. R. Fisher, and P. K. Dorhout, *Chem. Mater.* **14**, 480 (2002).
- <sup>86</sup> J. Ryu, S. Priya, K. Uchino, and H. E. Kim, *J. Electroceram.* **8**, 107 (2002).
- <sup>87</sup> J. van den Boomgard, D. R. Terrell, R. A. J. Born, and H. F. J. I. Giller, *J. Mater. Sci.* **9**, 1705 (1974); J. Van den Boomgaard, A. M. J. G. van Run, and J. van Suchtelen, *Ferroelectrics* **14**, 727 (1976).
- <sup>88</sup> B. Wul and I. M. Goldman, *Academie des Sciences de l'URSS - Comptes Rendus* **51**, 21 (1946).
- <sup>89</sup> For a review see N. Izyumskaya, Y. Alivov, S.-J. Cho, H. Morkoç, H. Lee, and Y.-S. Kang, *Critical Reviews in Solid State and Materials Sciences* **32**, 111 (2007).

- <sup>90</sup> E. C. Subbaro, Phys. Rev. **122**, 804 (1961).
- <sup>91</sup> P. H. Fang, C. Robbins, and F. Forrat, Academie des Sciences - Comptes Rendus **252**, 683 (1962).
- <sup>92</sup> Q. M., Zhang, V. Bharti, G., Kavarnos, and M. Schwartz, (Ed.), "Poly (Vinylidene Fluoride) (PVDF) and its Copolymers", Encyclopedia of Smart Materials, John Wiley & Sons, Volumes 1-2, pp. 807-825 (2002).
- <sup>93</sup> O. Kenji, O. Hiroji, and K. Keiko, J. Appl. Phys. **81**, 2760 (1996).
- <sup>94</sup> S.-E. Park and T. E. Shrout, J. Appl. Phys. **82**, 1804 (1997).
- <sup>95</sup> G. Srinivasan, E. T. Rasmussen, A. A. Bush, K. E. Kamentsev, V. F. Meshcheryakov, and Y. K. Fetisov, Appl. Phys. A **78**, 721 (2004).
- <sup>96</sup> S.-K. Kim, J.-W. Lee, S.-C. Shin, H. W. Song, C. H. Lee, and K. No, J. Magn. Magn. Mater. **267**, 127 (2003).
- <sup>97</sup> A. E. Clark, "Magnetostrictive rare earth-Fe<sub>2</sub> compounds", in *Ferromagnetic materials: A handbook on the properties of magnetically ordered substances*, edited by E. P. Wohlfarth (North-Holland, Amsterdam, 1980) vol.1, p 531-589.
- <sup>98</sup> A. E. Clark, J. R. Cullen, and K. Sato, "Magnetostriction of single crystal and polycrystal rare earth-Fe<sub>2</sub> compounds", AIP Conference Proceedings **24**, 670 (1974).
- <sup>99</sup> For a more recent paper on TbDyFe see E.A. Lindgren, S. Haroush, J.C. Poret, A.D. Mazzatesta, M. Rosen, M. Wun-Fogle, J.B. Restorff, A.E. Clark and J.F. Lindberg, J. Appl. Phys. **83**, 7282 (1998); S.F. Fischer, M. Kelsch, and H. Kronmueller, J. Magn. Magn. Mater. **195**, 545 (1999); D.C. Jiles, and J. B. Thoele, Phys. Stat. Solidi A **147**, 535 (1995).
- <sup>100</sup> G. Srinivasan, E. T. Rasmussen, and R. Hayes, Phys. Rev. B **67**, 014418 (2003).
- <sup>101</sup> M. I. Bichurin, V. M. Petrov, Yu. V. Kiliba, and G. Srinivasan, Phys. Rev. B **66**, 134404 (2002).
- <sup>102</sup> M. I. Bichurin, R. V. Petrov, and Yu. V. Kiliba, Ferroelectrics **204**, 311 (1997).
- <sup>103</sup> C. S. Tsai and J. Su, Appl. Phys. Lett. **74**, 2079 (1999).
- <sup>104</sup> V. E. Demidov, B. A. Kalinikos, S. F. Karmanenko, A. A. Semenov, and P. Edenhofer, IEEE Trans. Microwave Theory Tech. **51**, 2090 (2003).
- <sup>105</sup> G. Srinivasan, R. Hayes, and M. I. Bichurin, Solid State Commun. **128**, 261 (2003).
- <sup>106</sup> G. Srinivasan, I. V. Zavislyak, and A. S. Tatarenko, Appl. Phys. Lett. **89**, 152508 (2006).
- <sup>107</sup> R. K. Zheng, Y. Wang, H. L. W. Chan, C. L. Choy, and H. S. Luo, Appl. Phys. Lett. **90**, 152904 (2007).
- <sup>108</sup> Y. G. Ma, W. N. Cheng, M. Ning, and C. K. Ong, Appl. Phys. Lett. **90**, 152911 (2007).
- <sup>109</sup> M. K. Lee, T. K. Nath, C. B. Eom, M. C. Smoak, and F. Tsui, Appl. Phys. Lett. **77**, 3547 (2000).

- 
- <sup>110</sup> J. Das, B. A. Kalinikos, A. R. Barman, and C. E. Patton, Appl. Phys. Lett. **91**, 172516 (2007).
- <sup>111</sup> D. A. Filippov, M. I. Bichurin, V. M. Petrov, V. M. Laletin, and G. Srinivasan, Phys. Solid State **46**, 1674 (2004).
- <sup>112</sup> D. A. Filippov, Phys. Solid State **47**, 1118 (2005).
- <sup>113</sup> U. Laletin, N. Padubnaya, G. Srinivasan, C. P. Devreugd, M. I. Bichurin, V. M. Petrov, and D. A. Filippov, Appl. Phys. Lett. **87**, 222507 (2005).
- <sup>114</sup> M. I. Bichurin, V. M. Petrov, O. V. Ryabkov, S. V. Averkin, and G. Srinivasan, Phys. Rev. B **72**, 060408 (2005).
- <sup>115</sup> G. Srinivasan, C. P. De Vreugd, V. M. Laletin, M. Paddubnaya, M. I. Bichurin, V. M. Petrov, and D. A. Filippov, Phys. Rev. B **71**, 1844423 (2005).
- <sup>116</sup> K. Koombua, R. M. Pidaparti, Ü. Özgür, and H. Morkoç, unpublished.
- <sup>117</sup> H. Zheng, J. Wang, S. E. Lofland, Z. Ma, L. Mohaddes-Ardabili, T. Zhao, L. Salamanca-Riba, S. R. Shinde, S. B. Ogale, F. Bai, D. Viehland, Y. Jia, D. G. Schlom, M. Wuttig, A. Roytburd, and R. Ramesh, Science **303**, 661 (2004).
- <sup>118</sup> F. Zavaliche, H. Zheng, L. Mohaddes-Ardabili, S. Y. Yang, Q. Zhan, P. Shafer, E. Reilly, R. Chopdekar, Y. Jia, P. Wright, D. G. Schlom, Y. Suzuki, and R. Ramesh, Nano Lett. **5**, 1793 (2005).
- <sup>119</sup> C.-W. Nan, G. Liu, Y. H. Lin, and H. D. Chen, Phys. Rev. Lett. **94**, 197203 (2005).
- <sup>120</sup> M. Liu, X. Li, H. Imrane, Y. Chen, T. Goodrich, Z. Cai, K. S. Ziemer, J. Y. Huang, and N. X. Sun, Appl. Phys. Lett. **90**, 152501 (2007).
- <sup>121</sup> J. D. Adam, L. E. Davis, G. F. Dionne, E. F. Schloemann, and S. N. Stitzer, IEEE Trans. Microwave Theory Tech. **50**, 721 (2002).
- <sup>122</sup> B. M. Lebed and V. D. Voronkov, Proc. 26th European Microwave Conference, Prague, 1996, pp 816-822.
- <sup>123</sup> R. Glockler, Int. J. Infrared Millimeter Waves **11**, 101 (1990).
- <sup>124</sup> L. R. Adkins, H. I. Glass, R. L. Carter, C. K. Wai, and J. M. Owens, J. Appl. Phys. **55**, 2518 (1984).
- <sup>125</sup> Y. K. Fetisov and G. Srinivasan, Appl. Phys. Lett. **87**, 103502 (2005).
- <sup>126</sup> F. Reggia and E. G. Spencer, Proc. IRE **45**, 1510 (1957).
- <sup>127</sup> Ronald F. Soohoo, IEEE Trans. Magn. **4**, 118 (1968).
- <sup>128</sup> B. Lax and K. J. Button, "Microwave Ferrites and Ferrimagnetics", McGraw-Hill, New York, 1962.
- <sup>129</sup> E. K.-N. Yung, R. S. Chen, K. Wu, and D. X. Wang, IEEE Trans. Microwave Theory and Techniques **46**, 1721 (1998).
- <sup>130</sup> E. N. Skomal, IEEE Trans. Microwave Theory and Techniques **11**, 117 (1963).

- <sup>131</sup> D. M. Pozar, “Microwave Engineering”, 3<sup>rd</sup> edition, 2005, John Wiley and Sons, Inc.
- <sup>132</sup> P. Shi, H. How, X. Zuo, S. D. Yoon, S. A. Oliver, and C. Vittoria, IEEE Trans. Magn. **37**, 2389 (2001).
- <sup>133</sup> C. E Fay and R.L. Comstock, IEEE Trans. Microwave Theory and Techniques **13**, 15 (1965).
- <sup>134</sup> K. Okubo and M. Tsutsumi, IEEE MTT-S Int. Microwave Symp. Dig., 2006, pp. 548 – 551.
- <sup>135</sup> H. How, T.-M. Fang, and C. Vittoria, IEEE Trans. Magn. **31**, 997 (1995).
- <sup>136</sup> R. A. Stem and R. W. Babbitt, U.S. Patent No 4,749,966, June 7, 1988; U.S. Patent No 4,754,237, June 28, 1988.
- <sup>137</sup> P. S. Carter, Jr., IEEE Trans. Microwave Theory Tech. **9**, 252 (1961).
- <sup>138</sup> H. Tanbakuchi, D. Nicholson, B. Kunz, and W. Ishak, IEEE Trans. Magn. **25**, 3248 (1989).
- <sup>139</sup> D. Nicholson, IEEE MTT-S Int. Microwave Symp. Dig., 1988, pp. 867–870.
- <sup>140</sup> J. Helszajn, “YIG Resonators and Filters”, John Wiley & Sons Inc., New York, 1985.
- <sup>141</sup> M. Lemke, W. Hoppe, W. Tolksdorf, and F. Weltz, IEE J. Microwaves, Optics, and Acoustics **3**, 253 (1979).
- <sup>142</sup> M. Lemke, Proc. of 9th Euro. Microwave Conf., 1979, pp. 617-620.
- <sup>143</sup> B. N. Enander, Proc. IRE **44**, 1421 (1956).
- <sup>144</sup> D. M. Pozar, Proc. IEEE **80**, 79 (1992).
- <sup>145</sup> G. A. Deschamps, “Microstrip microwave antennas,” presented at the Third USAF Symp. on Antennas, 1953.
- <sup>146</sup> K. R. Carver and J. W. Mink, IEEE Trans. Antennas Propag. **29**, 2 (1981).
- <sup>147</sup> D. M. Pozar, IEEE Trans. Antennas Propagation **40**, 1084 (1992).
- <sup>148</sup> A. D. Brown, J. L. Volakis, L.C. Kempel, and Y. Y. Botros, IEEE Trans. Antennas Propagation **47**, 26 (1999).
- <sup>149</sup> J. C. Batchelor, G. Classen and R. J. Langley, 10<sup>th</sup> International Conference on Antennas and Propagation, 14-17 April 1997, Conference Publication No. 436, Vol. 1, pages:30 – 33.
- <sup>150</sup> K. K. Tsang, and R. J. Langley, Electron. Lett. **30**, 1257 (1994).
- <sup>151</sup> E. F. Zaitsev, Y. P. Yavon, Y. A. Komarov, A. B. Guskov, and A. Y. Kanivets, IEEE Trans. Antennas Propagat. **42**, 304 (1994).
- <sup>152</sup> H. Y. D. Yang, IEEE Trans. Antennas Propagation **44**, 1127 (1996).
- <sup>153</sup> H. Maheri, M. Tsutsumi, and N. Kumagai, IEEE Trans. Antennas Propag. **36**, 911 (1988).

- <sup>154</sup> B. A. Kramer, S. Koulouridis, C.-C. Chen, and J. L. Volakis, *Antennas and Wireless Propagation Lett.* **5**, 32 (2006).
- <sup>155</sup> G. Tyras and G. Held, *IEEE Trans. Microwave Theory Tech.* **6**, 268 (1958).
- <sup>156</sup> A. T. Adams, *IEEE Trans. Antennas Propag.* **15**, 342 (1967).
- <sup>157</sup> D. J. Aggelakos and M. M. Korman, *Proc. IRE* **44**, 1463 (1956).
- <sup>158</sup> N. Das and S. K. Chowdhury, *Electron. Lett.* **16**, 817 (1980).
- <sup>159</sup> N. Das, S. K. Chowdhury, and J. S. Chatterjee, *IEEE Trans. Antennas Propag.* **31**, 188 (1983).
- <sup>160</sup> S. N. Das, S. K. Chowdhury, *IEEE Trans. Antennas Propag.* **30**, 499 (1982).
- <sup>161</sup> H. How, P. Rainville, F. Harackiewicz and C. Vittoria, *Electron. Lett.* **28**, 1405 (1992).
- <sup>162</sup> D. S. Dunn, M. S. Telep, and E. P. Augustin, *Southcon/94, Conference Records, Page(s) 230 – 235, March 1994.*
- <sup>163</sup> H. Chang, I. Takenchi, and X.-D. Xiang, *Appl. Phys. Lett.* **74**, 1165, (1999).
- <sup>164</sup> M. I. Bichurin, I. A. Kornev, V. M. Petrov, A. S. Tatarenko, Yu. V. Kiliba, and G. Srinivasan, *Phys. Rev. B* **64**, 094409 (2001).
- <sup>165</sup> A. B. Ustinov, G. Srinivasan, and B. A. Kalinikos, *Appl. Phys. Lett.* **90**, 031913 (2007).
- <sup>166</sup> A. A. Semenov, S. F. Karmanenko, V. E. Demidov, B. A. Kalinikos, G. Srinivasan, A. N. Slavin, and J. V. Mantese, *Appl. Phys. Lett.* **88**, 033503 (2006).
- <sup>167</sup> A. V. Silhanek, W. Gillijns, V. V. Moshchalkov, B. Y. Zhu, J. Moonens, and L. H. A. Leunissen, *Appl. Phys. Lett.* **89**, 152507 (2006).
- <sup>168</sup> A. S. Tatarenko, G. Srinivasan, and M. I. Bichurin, *Appl. Phys. Lett.* **88**, 183507 (2006).
- <sup>169</sup> S. Mathews, R. Ramesh, T. Venkatesan, and J. Benedetto, *Science* **276**, 238 (1997).
- <sup>170</sup> T. Wu, S. B. Ogale, J. E. Garrison, B. Nagaraj, Amlan Biswas, Z. Chen, R. L. Greene, R. Ramesh, T. Venkatesan, and A. J. Millis, *Phys. Rev. Lett.* **86**, 5998 (2001).
- <sup>171</sup> S. Hontsu, H. Nishikawa, H. Nakai, J. Ishii, M. Nakamori, A. Fujimaki, Y. Noguchik, H. Tabata, and T. Kawai, *Supercond. Sci. Technol.* **12**, 836 (1999).
- <sup>172</sup> S. S. Gevorgian, D. I. Kaparkov, and O. G. Vendik, *IEE Proc. Microw. Antennas Propag.* **141**, 501 (1994).
- <sup>173</sup> R. A. Chakalov, Z. G. Ivanov, Yu. A. Boikov, P. Larsson, E. Carlsson, S. Gevorgian, and T. Claeson, *Physica C* **308**, 279 (1998).
- <sup>174</sup> G. F. Dionne, D. E. Oates, D. H. Temme, and J. A. Weiss, *IEEE Trans. Microwave Theory Tech.* **44**, 1361 (1996).
- <sup>175</sup> D. E. Oates, A. Piqué, K. S. Harshavardhan, J. Moses, F. Yang, and G. F. Dionne, *IEEE Trans. Appl. Supercond.* **7**, 2338 (1997).
- <sup>176</sup> S. Dong, J. F. Li, and D. Viehland, *Appl. Phys. Lett.* **83**, 2265 (2003).



- <sup>177</sup> S. Dong, J. F. Li, D. Viehland, J. Cheng, and L. E. Cross, Appl. Phys. Lett. **85**, 3534 (2004).
- <sup>178</sup> A. B. Ustinov, G. Srinivasan, and Y. K. Fetisov, J. Appl. Phys. **103**, 063901 (2008).
- <sup>179</sup> A. K. Tagantsev, V. O. Sherman, K. F. Astafiev, J. Venkatesh, and N. Setter, J. Electroceramics **11**, 5 (2003).
- <sup>180</sup> N. Setter, D. Damjanovic, L. Eng, G. Fox, S. Gevorgian, S. hong, A. Kingon, H. Kohlstedt, N. Y. Park, G. B. Stephenson, I. Stolitchnov, A. K. Tagantsev, D. V. Taylor, T. Yamda, and S. Streiffer, J. Appl. Phys. **100**, 051606 (2006).
- <sup>181</sup> S.-S. Kim, Y.-C. Yoon, and K.-H. Kim, J. Electroceramics **10**, 95 (2003).
- <sup>182</sup> A. S. Tatarenko, V. Gheevarghese and G. Srinivasan, Electronics Letters **42**, 540 (2006).
- <sup>183</sup> D. E. Oates and G. F. Dionne, IEEE MTT-S Int. Microwave Symp. Dig., 1997, pp. 303–306.
- <sup>184</sup> A. A. Semenov, S. F. Karmanenko, B. A. Kalinikos, G. Srinivasan, A. N. Slavin, and J. V. Mantese, Electron. Lett. **42**, 641 (2006).
- <sup>185</sup> S. W. Kirchoefer, J. M. Pond, H. S. Newman, W.-J. Kim, and J. S. Horwitz, IEEE MTT-S International Microwave Symposium Digest **3**, 1359 (2000).
- <sup>186</sup> V. E. Demidov, B. A. Kalinikos, and P. Edenhofer, J. Appl. Phys. **91**, 10007 (2002).
- <sup>187</sup> B. A. Kalinikos and A. N. Slavin, J. Phys. C **19**, 7013 (1986).
- <sup>188</sup> A. Asamitsu, Y. Moritomo, Y. Tomioka, T. Arima, and Y. Tokura, Nature **373**, 407 (1995).